Network Integration of a Quantum Dot Entangled Photon-pair Source

Ziheng Xiang

Department of Physics

University of Cambridge

This thesis is submitted for the degree of

Doctor of Philosophy

Selwyn College

September 2020

Declaration

This thesis is the result of my own work and includes nothing which is the outcome of work done in collaboration except as declared in the Preface and specified in the text. It is not substantially the same as any that I have submitted, or, is being concurrently submitted for a degree or diploma or other qualification at the University of Cambridge or any other University or similar institution except as declared in the Preface and specified in the text. I further state that no substantial part of my thesis has already been submitted, or, is being concurrently submitted for any such degree, diploma or other qualification at the University of Cambridge or any other University or similar institution except as declared in the Preface and specified in the text. It does not exceed the prescribed word limit for the relevant Degree Committee.

Ziheng Xiang
September 2020

Network Integration of a Quantum Dot Entangled Photon-pair Source

Ziheng Xiang

Sub-Poissonian entangled photon-pair sources based on semiconductor quantum dots are promising devices for the construction of a secure quantum network, thanks to their natural lack of multi photon-pair generation. In the previous decades, we have witnessed the achievements on a large variety of quantum dot light sources. However, they are still far from being used in an established standard fibre network. On the one hand, most of the sources are still operated in an environment that requires the installation of bulky laser setups, preventing their integration in a network. On the other hand, most of the experiments on entangled qubits generated from quantum dot sources are performed in the laboratory, resulting in a lack of work on the system supporting the remote operation of the device and high-fidelity transmission of entangled qubits over a long-distance in a large geographic scale.

In this work, we demonstrate the integration of a quantum dot device in an optical network. To achieve this, both the source and the systems have been developed that favour the remote operation in a non-laboratory environment.

For the source, a fully electrically operated telecom entangled on-chip pumping quantum dot device is designed and fabricated. It supports the operation at a low current of 1.6 mA and simultaneously achieves high wavelength tuneability of more than 25 nm by changing the applied bias voltage from 0 to -3.8 V. A in-laboratory entanglement fidelity of $97.3 \pm 0.2\%$ is achieved with this on-chip pumping quantum dot light source.

Several systems are developed in this work, supporting the integration of this developed source. We have proposed an innovative method for the precise alignment of the detection system to the quantum dot eigenbasis based on analysing time-resolved photon-pair correlations in a set of randomly oriented detection bases. It eliminates the restriction on the placement of the free-space polariser before the light is coupled from the quantum dot emitter into the first single-mode fibre.

To support the classical traffic for sending the control signal to required components for source and system operation, we have developed a multiplexing system that allows the transmission of qubits at the telecom O-band with classical traffic at the telecom C-band over the same optical fibre without generating severe background at the quantum channel.

To overcome changes of birefringence introduced by the deployed optical fibres, which causes the variation of the polarisation states during qubit transmission, we have developed a polarisation stabilisation system making use of the commercial polarisation controlling components. The system has an extremely low loss and a high duty cycle.

The above development has enabled us to achieve a successful deployment and integration of the quantum dot device in the Cambridge Fibre Network. We demonstrate multiplexing of true single entangled photons tuned to 1310 nm from the on-chip pumping device with classical data traffic and achieve entanglement fidelity above 94% for over 40 hours.

Acknowledgements

I would like to show my gratitude to the Cambridge Trust, China Scholarship Council and Toshiba Europe Limited for the financial support of the Ph.D. programme, as well as the life and study in Cambridge.

I am grateful to my supervisors Andrew Shields and David Ritchie, for their continuous support during my Ph.D. I have been very lucky to have my supervisors who care so much about my work, and who responded to my questions and queries so promptly.

I would like to express my deep appreciation to Jan Huwer for all the discussion and support he offers during this entire work. I do miss the inspiring ideas with enthusiasm in our discussion, and every fun minute in our experiment. The drive together with Mark to deploy the quantum dot with tons of boxes is one of the moments that will not disappear from my memory.

The completion of this work would have been more difficult were it not for the support from my colleagues. I would thank Mark Stevenson for kindly sharing me with his profound knowledge of the quantum dot, Joanna Skiba-Szymanska for her instruction in the cleanroom and Tina Müller for giving me necessary help during the experiment.

And my Ph.D. life would not have been as enjoyable and delightful as it is without the company and support from my friends at Toshiba. Especially I would like to thank Matthew Anderson for the discussion in the lab as well as in the pub, and the memorial moments during CEWQO 2018 in Mallorca. I would like to thank Innocenzo de Marco, Ginny Shooter and Mariella Minder and all friends in Toshiba for the chat and discussion.

The love that I received from my family has made it all possible to accomplish my work. My mother Lin-Fang Ou-Yang and father Yu-Hong Xiang have always been kind and caring. You have 'teleported' all that I need for studying abroad. And I must thank my partner Shi-Yi Wang for encouraging me to move forward, making me always being positive toward everything around me. And I would extend my appreciation for my cousins Bo-Chen Jiang and Yu-Xin Jiang, for all the fun time even when we do not meet that often anymore.

Publications

Article

Zi-Heng Xiang, Jan Huwer, Joanna Skiba-Szymanska, R. Mark Stevenson, David J. P. Ellis, Ian Farrer, Martin B. Ward, David A. Ritchie & Andrew J. Shields. "A tuneable telecom wavelength entangled light emitting diode deployed in an installed fibre network." *Commun Phys 3, 121 (2020).* https://doi.org/10.1038/s42005-020-0390-7

Zi-Heng Xiang, Jan Huwer, R. Mark Stevenson, Joanna Skiba-Szymanska, Martin B. Ward, Ian Farrer, David A. Ritchie & Andrew J. Shields. "Long-term transmission of entangled photons from a single quantum dot over deployed fiber." *Sci Rep 9, 4111 (2019).* https://doi.org/10.1038/s41598-019-40912-z

Ginny Shooter, Zi-Heng Xiang, Jonathan R.A. Müller, Joanna Skiba-Szymanska, Jan Huwer, Jonathan Griffiths, Thomas Mitchell, Matthew Anderson, Tina Müllerller, Andrzej Krysa, R. Mark Stevenson, Jon Heffernan, David A. Ritchie, and Andrew J. Shields. "1GHz clocked distribution of electrically generated entangled photon pairs." *Opt. Express 28, 36838-36848 (2020)* https://doi.org/10.1364/OE.405466

Conference Contribution

Zi-Heng Xiang, Jan Huwer, R. Mark Stevenson, Joanna Skiba-Szymanska, Martin B. Ward, Ian Farrer, David A. Ritchie & Andrew J. Shields. "Entangled photon transmission from a quantum dot over loop-back fiber in Cambridge network." *CLEO: QELS Fundamental Science. Optical Society of America, 2019.* (Talk)

Zi-Heng Xiang, Jan Huwer, Joanna Skiba-Szymanska, R. Mark Stevenson, David J. P. Ellis, Ian Farrer, Martin B. Ward, David A. Ritchie & Andrew J. Shields. "A 1310nm Tuneable ELED Operated in Cambridge Fibre Network." *Single Photon Workshop, Milano, Italy, 2020* (Talk)

Zi-Heng Xiang, Jan Huwer, R. Mark Stevenson, Joanna Skiba-Szymanska, Martin B. Ward, Ian Farrer, David A. Ritchie & Andrew J. Shields. "Field trial of transmitting polarisation entangled photons from a quantum dot." *QCrypt, Shanghai, China, 2018.* (Poster)

Zi-Heng Xiang, Jan Huwer, Joanna Skiba-Szymanska, R. Mark Stevenson, David J. P. Ellis, Ian Farrer, Martin B. Ward, David A. Ritchie & Andrew J. Shields. "Network Integration of Quantum Dot Device and Entanglement in Cambridge Fiber Network." *Asian Quantum Information Science Conference, Seoul, Korea. 2019* (Poster)

Jan Huwer, Zi-Heng Xiang, Joanna Skiba-Szymanska, R. Mark Stevenson, David J. P. Ellis, Ian Farrer, Martin B. Ward, David A. Ritchie & Andrew J. Shields. "Operation of semiconductor telecom entangled photon sources over installed fiber networks." *CLEO: QELS Fundamental Science. Optical Society of America, 2020.*

Jan Huwer, Zi-Heng Xiang, Joanna Skiba-Szymanska, R. Mark Stevenson, David J. P. Ellis, Ian Farrer, Martin B. Ward, David A. Ritchie & Andrew J. Shields. "Network integration and coherent operation of telecom entangled light sources based on semiconductor quantum dots." *European Quantum Electronics Conference. Optical Society of America, 2019.*

Table of contents

List of figures

List of tables

Acronyms

APD Avalanche photodiode

BS Beam splitter

BSM Bell-state measurement

CBG Circular Bragg grating

CFN the Cambridge Fibre Network

CRL Toshiba Cambridge Research Laboratory

CWDM Coarse wavelength division multiplexer

DBR Distributed Bragg reflectors

DGD Differential group delay

DOP Degree of polarisation

DWDM Dense wavelength division multiplexer

EL Electroluminescence

ELED Entangled light-emitting-diode

EPC Electrical polarisation controller

FSS Fine structure splitting

FWM Four-wave mixing

FWP fibre-wave plate

HWP Half-wave plate

LED Light emitting diode

LP Linear polariser

MBE Molecular beam epitaxy

OCP On-chip pumping

PBS Polarising beam splitter

PL Photoluminescence

PM Power meter

PMD Polarisation mode dispersion

PMF Polarisation-maintaining fibre

QD Quantum dot

QKD Quantum key distribution

QW Quantum well

QWP Quarter-wave plate

RF Radio frequency

SK Stranski-Krastanov

SMF Single-mode fibre

SNSPD Superconducting nanowire single-photon detector

SPDC Spontaneous parametric down conversion

TCSPC Time-correlated single photon counting

TDM Time-division multiplexing

UV Ultra-violet

WDM Wavelength-division multiplexing

WGM Whispering-gallary-mode

WL Wetting layer

X Exciton

XX Biexciton

Chapter 1

Introduction

1.1 Quantum network

Arising from theories explaining the experimental observation which could not be solved by classical physics, quantum physics research has gradually pushed people to understand the nature of fundamental particles, such as atoms, electrons and photons profoundly. Therefore, the application of quantum effects evolves from mainly laser technology and semiconductors that touches the surface of quantum mechanics, to a deeper level where the manipulation of quantum states is explored and utilised.

The end of the last century encounters a fast development of several contemporary quantum technologies. Quantum cryptography, initially invented by Charles Bennett and Giles Brassard in 1984 [1] has illustrated a potential method for sharing information between 2 parties without being unknowingly stolen, which generated a significant impact. Quantum cryptography since then has become a theory-supported subject [2] and received resources on research of protocols [3–6] and implementations [7–9]. The best-known quantum cryptography task, which is the quantum key distribution (QKD), now has become the most mature quantum technology in real-world applications [10–13]. Starting roughly at the same time as quantum cryptography, a quantum mechanics-based Turing machine setup has been proposed [14], which was one of the earliest ideas of building a quantum computer. It then attracted attention as it is supposed to massively accelerate the speed of some algorithms and achieve tasks that could not be realised by a classical computer [15, 16]. Quantum computing is being developed for decades, and the state-of-art products and prototypes have indicated its potential of being practically used [17]. More recent progress on quantum metrology [18] contributed to an on-going trend of fast progress on quantum technology. It exploits the quantum theory to achieve measurements with resolution and sensitivity beyond the classical limits.

Although individual applications of quantum physics, if practically realised, could already enable advantages over classical technology in multiple fields, a 'so-called' quantum network [19, 20] would enable scalable application over long distances, capable of transferring quantum

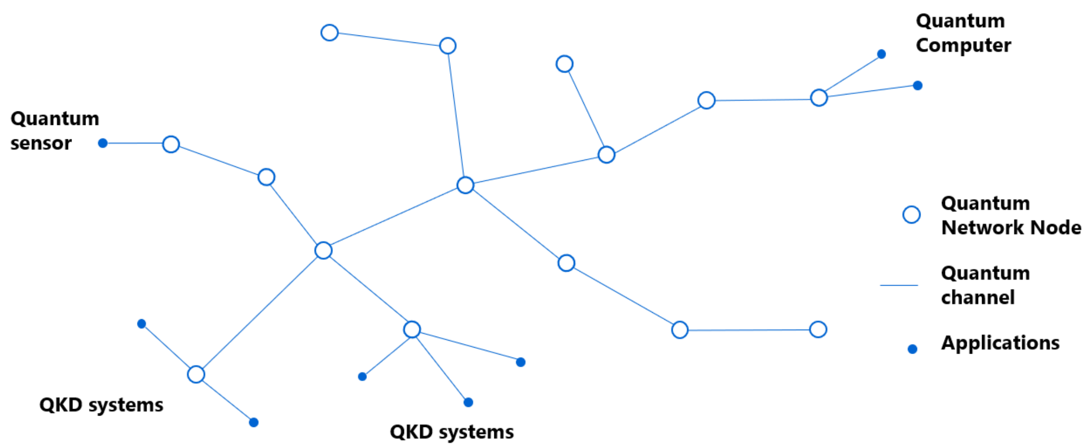

Fig. 1.1 A scheme for a quantum network in practise. Quantum nodes and quantum channels forms the 'backbone' of the quantum network. Applications are linked via the backbone.

states between different locations. In such a network, quantum information is generated and processed locally in various locations referred to as 'quantum nodes', and then transmitted via 'quantum channels' to the other nodes. Quantum channels connect various applications at different nodes, as is introduced in Figure 1.1. In this PhD project, we work on various essential technologies for building a quantum network.

Thanks to the capability of photons being the carriers of quantum information, transmitting quantum states could be achieved over long-distance. The underlying importance is at the security and efficiency of the transmission, influenced by the photon statistics. For a classical light source such as a pulsed laser diode with mean photon number μ, the probability of having n photons in each pulse follows a Poissonian distribution:

$$P(n) = \frac{\mu^n e^{-\mu}}{n!} \tag{1.1}$$

Although in ideal cases, each quantum bit (qubit) should be carried by one photon for unconditional security [21], development of decoy-state protocol [7, 22] and entanglement-based protocols [23, 24] has made the sources with Poissonian distributed photon statistics useful as well for quantum cryptography communication. In many works on QKD, Poissonian sources such as weak coherent laser pulses are used as photon sources. However, these sources come with drawbacks. Decoy states would occupy certain time slots originally used for sending keys. Additionally, larger photon numbers result in higher quantum bit-error-rate [25]. From equation (1.1), we notice a trade-off between the probability of emitting a vacuum states ($n = 0$) or multi-photon states($n > 1$). Therefore to reduce multi-photon emission, the light sources need to be operated at low power, resulting in a high probability of vacuum states and hence, low efficiency. This is a limiting factor for a practical quantum network.

Given the above reason, the development of sub-Poissonian photon sources is of great importance. It is defined as sources with photon-number variance less than the mean photon

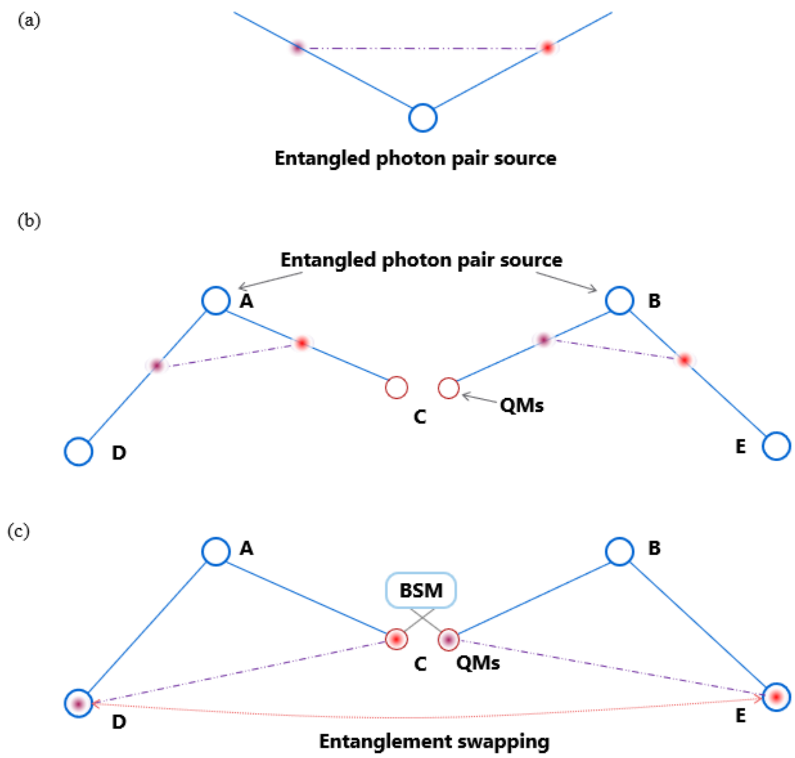

Fig. 1.2 (a) An entangled light source generates two entangled particles that are correlated without distance limitation. (b) Quantum repeater setup. Two sources are installed at location A and B, both emitting entangled photon pairs. A central node is at C between the two locations with deployed quantum memories (QMs). D and E are two remote locations between which the information is supposed to be shared. (c) Entanglement swapping. The entangled photon pairs emitted at location A is sent to C and D; and pairs emitted at location B is sent to C and E. QMs are used to store the qubits and maintain its coherence. When a Bell-State Measurement (BSM) is performed at C with the two received photons, the end-to-end entanglement is created between the photons at D and E.

number ($\Delta n^2 < n$). We in this work focus on quantum dots as the quantum information carrier, with their capabilities of generating sub-Poissonian entangled photon-pairs.

Quantum channels supporting photon transmission in the network are another matter to be considered. Both free-space optical channels and optical fibres could be the medium for quantum channels. For transmission in free-space, the performance is limited by strong background noise caused by sunlight during daytime. Environmental changes such as air turbulence and mist also negatively influence the transmission in free-space. Therefore, it is less practical compared with optical fibre.

A quantum network requires quantum channels to transmit quantum states with high precision of their physical parameters in which the quantum states are encoded. Direct transfer with a feedback system for stabilisation is feasible for a quantum channel with a short distance. However, for a distance scale of inter-city or -state, high optical loss directly results in a reduction of qubit rate, which would significantly decrease the performance of the quantum network. Moreover, given that the detectors always have background noise at the current stage, the fibre optical loss limits the maximum transmission distance of a quantum state. However, it could be mitigated by introducing quantum repeaters [26–28], which uses a remarkable feature of quantum mechanics - entanglement.

As is indicated in Figure 1.2 (a), two entangled particles maintain the correlation of quantum states regardless of their distance, meaning that a measurement on one of the particles in the pair would collapse the qubit state on the partner particle (The details of entanglement will be introduced in the next section). In a quantum repeater, entanglement is "swapped" [29]. As is illustrated in Figure 1.2 (b), entangled photon pairs are created by sources installed at Location A (sent to C and D) and B (sent to C and E). It is possible to create entanglement between location D and E by a Bell-State Measurement (BSM) at location C, shown in Figure 1.2 (c). Quantum information sent over quantum repeaters is therefore not transmitted directly via a physical channel. Instead, it is 'teleported' once the entanglement at a distant location (refers to C here) is established. One could, as well, add more entangled pairs at different locations to further extend the entanglement, which is the reason why it is called a "quantum repeater".

A quantum repeater would require quantum memories [30, 31] in each location to store the qubits until the next pair arrives. Whereas at the current stage when a quantum memory is not available, one could still use a simpler link, a so-called quantum relay [32–35], to teleport a photon from one location to another. We notice here that for a quantum repeater or a quantum relay, effective distribution of entangled states between 2 locations is necessary.

Quantum communication, including the above-mentioned QKD, quantum repeater or relay, requires a classical communication channel established in parallel. Essential information such as prepared measurement bases of the qubits needs to be exchanged between the end nodes. Installing or allocating dark-fibres for transmitting quantum information separately from the classical link seems to be a widely-adopted approach [36, 37]. This, however, would lead to the construction of new fibre network infrastructure, coming at a high cost. We hence focus on the integration of the quantum sources within a real fibre-network.

In this chapter, we would like to provide background information to support the following work on the realisation of entangled photon pairs transmission in an urban optical network environment. Therefore, contents for the following sections are the introductions of entanglement (1.2), entangled photon-pair sources (1.3) and the network integration (1.4).

1.2 Entanglement

Entanglement is a critical resource of a quantum network, serving as the core of quantum repeaters and relays. To introduce quantum entanglement, we would like to start with a comparison between a system of a single quantum (for example, a photon) and that of multiple quanta, from the perspective of quantum physics.

For a (quantum) system with one single photon, one could represent its quantum states as:

$$|\Phi_1\rangle = \sum_n p_{i_n} |i_n\rangle \tag{1.2}$$

Here, it has various eigenstates $|i_n\rangle$, each with a probability p_{i_n}.

For a system with several subsystems, there exists more than one scenario. We consider the first scenario being two individual photons in one system without correlations, meaning that the quantum states of one photon are not affected by the other. The quantum state of this system could thus be denoted as:

$$|\Phi_2\rangle = \sum_n p_{i_n} |i_n\rangle \cdot \sum_m p_{j_m} |j_m\rangle \tag{1.3}$$

This system with two photons is in a product state and therefore, separable. It is commonly applied to scenarios such as the position of two individual photons.

There also exist systems in which each subsystem is correlated with one or multiple other subsystems. Considering a case where:

$$|\Phi\rangle = p_1|i_1\rangle|j_1\rangle + p_2|i_2\rangle|j_2\rangle + ... + p_n|i_n\rangle|j_n\rangle \tag{1.4}$$

Here $|i_n\rangle$ and $|j_n\rangle$ are the quantum states for the first subsystem and second subsystem respectively. It could be noticed that once the quantum state for the first subsystem is measured, the state of the second system is determined. It could occur in a system with a pair or group of particles, which is referred to as an entangled quantum state and therefore, being not separable.

The history of entanglement research could be dated back to 1935 with a joint discovery by Albert Einstein, Boris Podolsky and Nathan Rosen, that is the so-called 'EPR Paradox'. It points out that when two particles with a state Φ as is in equation (1.4), the measurement result of one particle state would give us the knowledge of another particle's exact state instantly [38]. It violates the special relativity that no information could be transmitted faster than the speed of light. The state those two particles are referred to as an 'entangled state' in later research. The discussion and explanation, aiming to explain the 'spooky action' on a distant particle in an entangled pair, has started since then, including initially Einstein's famous local-hidden-variable theory [39], later replaced by Bell's theorem [40] to be accepted by the majority.

Compared with a normal point-to-point communication where the optical source is located at one end and the detection modules are at the other, entanglement-based quantum communication

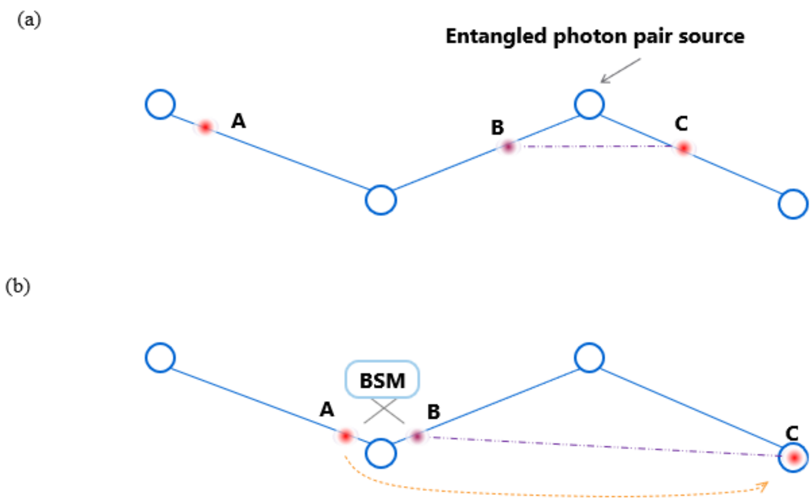

Fig. 1.3 (a) An illustration of quantum teleportation. Qubit A carries the quantum states to be transmitted. The entangled photon-pair source generates qubit pair B and C. Qubit A and B is sent over an optical fibre to the same location in between. Qubit C is sent to the target location. (b) We perform a Bell-state measurement on qubit A and B. It will project the partner qubit C of B onto a unitary transformed state of A.

enables a possibility of generating photon pairs from a location without trust. It could then be sent to locations between which we want to establish communication. Quantum teleportation has been proposed for this purpose [41, 42]. Its architecture is illustrated in Figure 1.3. In this scheme, the target is to transmit qubit A with state

$$|\varphi_A\rangle = \alpha|0\rangle + \beta|1\rangle \tag{1.5}$$

to the target location. Here, $|0\rangle$ and $|1\rangle$ could be any orthogonal states. In principle, α and β could be chosen arbitrarily if the normalisation condition: $|\alpha|^2 + |\beta|^2 = 1$ is met.

Considering four Bell-states:

$$|\Phi^\pm\rangle = \frac{1}{\sqrt{2}}|00\rangle \pm \frac{1}{\sqrt{2}}|11\rangle$$
$$|\Psi^\pm\rangle = \frac{1}{\sqrt{2}}|01\rangle \pm \frac{1}{\sqrt{2}}|10\rangle$$

With an entangled photon pair source installed at the node, we prepare an entangled photon pair namely B and C, with the entangled states $|\Phi^+_{BC}\rangle = (|0_B 0_C\rangle + |1_B 1_C\rangle)/\sqrt{2}$

Such that the overall system has a state:

$$|\Phi_s\rangle = (\alpha|0_A\rangle + \beta|1_A\rangle) \otimes (\frac{\sqrt{2}}{2}|0_B 0_C\rangle + \frac{\sqrt{2}}{2}|1_B 1_C\rangle) \tag{1.6}$$

At this stage, we send B to the same location as input qubit A, while C to the target location, as is shown in Figure 1.3. If the prepared qubit A is indistinguishable from qubit B and C, then the three-photon states is expressed as an overall system in state $|\varphi_A\rangle \otimes |\Phi^+_{BC}\rangle$, which could be rewritten into a form of

$$\begin{aligned} |\varphi_A\rangle \otimes |\Phi^+_{BC}\rangle = \frac{1}{2}(&|\Phi^+_{AB}\rangle \otimes |\varphi_C\rangle + |\Phi^-_{AB}\rangle \otimes \sigma_z|\varphi_C\rangle + \\ &|\Psi^+_{AB}\rangle \otimes \sigma_x|\varphi_C\rangle - i|\Psi^-_{AB}\rangle \otimes \sigma_y|\varphi_C\rangle) \end{aligned}$$

where σ_i are the Pauli matrices

$$\sigma_x = \begin{bmatrix} 0 & 1 \\ 1 & 0 \end{bmatrix}, \sigma_y = \begin{bmatrix} 0 & -i \\ i & 0 \end{bmatrix}, \sigma_z = \begin{bmatrix} 1 & 0 \\ 0 & -1 \end{bmatrix}$$

Hence, a BSM performed on qubit A and B would tell us which of the four states shown in equation 1.2 the system is projected onto. It simultaneously collapses the photon C to a unitary transformed state of the original input qubit A, which could be recovered by a unitary transformation. The BSM result of the qubit pair A and B needs to be sent to the location of photon C via a classical communication channel. However, such information does not include any information regarding qubit A.

Quantum teleportation serves as the basis of a quantum relay. It teleports quantum states from one location to the other. Replacing the original photon A with another entangled photon pair A and D, one could realise a so-called entanglement swapping by the same BSM on A and B, which projects photon C and D onto an entangled state[43]. With a quantum memory to store and synchronise the entangled qubits C and D, a quantum repeater is established.

While quantum repeaters, being scalable, could be the ideal quantum nodes, quantum relays would be able to transmit qubits to distant location without the requirement of trust and the need of quantum memory without being scalable. And entanglement is the core resources for both quantum relay and quantum repeater.

1.3 Entangled photon-pair sources

The previous section illustrates the importance of entanglement in a quantum network. The generation of entangled quantum states at a quantum node is thus critical. Over the last few years, we have witnessed the development of both Poissonian photon sources, including Spontaneous Parametric Down Conversion (SPDC) [44–46] or Four-Wave Mixing (FWM) [47–49], and sub-Poissonian sources such as Quantum Dots (QDs) [50–52] for entanglement generation.

SPDC or FWM sources generate entangled photons from laser pulses by non-linear optical effects, occurring in non-linear optical media such as crystals and optical fibres. They are relatively easy to operate compared to sub-Poinssonian sources with the capability of high-fidelity entanglement generation. However, their underlying low efficiency, as is discussed in Section 1.1, would be a limiting factor for a future quantum network. Given the Poissonian distribution of the photon statistics making the entangled photon pair generation a probabilistic process, alternative sources are therefore required for a quantum network.

A previous study has illustrated the possibility of generating polarisation-entangled photon pairs using a semiconductor QD via the Biexciton-exciton (XX-X) cascade [50]. These three-dimensionally confined crystals contain only a few discrete energy levels, therefore referred to as ’artificial atoms’. Over the last decades, lots of resources and efforts have been put into research on QDs as sub-Poissonian entangled photon-pair sources. It is also the focus of this work.

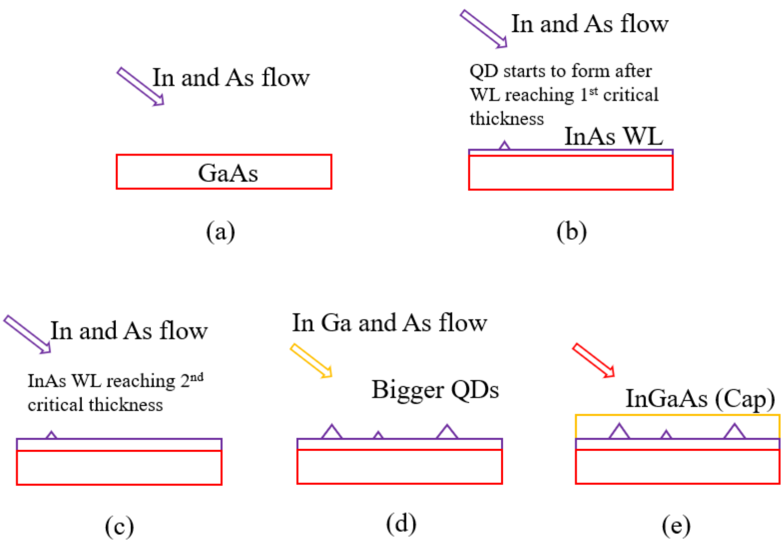

Fig. 1.4 Wafer growth and QD formation. InAs is deposited on GaAs (a). After the initial formation of WL, InAs starts to cluster into small islands, forming QDs (b). We continue applying InAs flow and push the WL, reaching its second critical thickness (c), after which the bigger QDs are formed (d). It is then capped by a layer InGaAs by applying In, Ga and As flow (e).

QD emission is influenced by their material composition and dimensions, as well as the surrounding semiconductor matrix. QD formation is based on epitaxy, in which ordered deposition of one atom lattice layer atop another. In the strain-driven Stranski-Krastanov (SK) growth mode [53], when a material with larger lattice parameter than the current layer is being deposited, it leads to the deposition of a strained film. The formation of islands is energetically favourable on this film, as it reduces the strain energy. This is how QDs are formed.

An example is given here corresponding to the growth of QDs used in this work, shown in Figure 1.4. Here the growth is performed using Molecular Beam Epitaxy (MBE). A flow of In and As is injected by the MBE to the GaAs substrate. The strained film, a so-called 'wetting layer (WL)', is formed initially, with a thickness of around several atoms. When the first critical thickness is reached, InAs starts to cluster, and QD islanding commences. These are the InAs/GaAs QDs emitting at around 950 nm, although dependent strongly on various parameters during growth. When the bi-modal growth method [54] is applied by means of keeping on applying a flow of InAs after initial QD formation, the WL is pushed to reach its second critical thickness. It would then result in QDs with larger sizes. An InGaAs strain-relaxation layer is capped above. This cap layer also pushes the emission to a longer wavelength reaching telecom O-band, owing to its lower bandgap energy compared with GaAs.

While Figure 1.4 illustrates a part of the essential procedures required for QD generation, more growth is required to form, for example, an AlGaAs – GaAs quantum well (QW) and stacked Distributed Bragg Reflectors (DBR) made from GaAs/AlGaAs, in order to provide an environment favouring the QD emission. Details of the procedures will be illustrated in Chapter 2.

The QD emission wavelength is influenced by the energy gap between its conduction and valence energy bands. Different from classical semiconductor devices, its dimensions with a scale of a few nanometres provide it with a particle-in-a-box effect. This model gives us the overall QD energy bandgap of [55]:

$$\Delta E(r) = E_{gap} + \left(\frac{h^2}{8r^2}\right)\left(\frac{1}{m_e} + \frac{1}{m_h}\right) \tag{1.7}$$

where h represents the Planck constant, E_{gap} represents the energy bandgap of the bulk material, m_e and m_h are the effective masses of the electron and hole, and r is the radius of the QD. The above model describes the zero-point energy of the 'box' based on an ideal case of infinitely high energy sidewalls. However, it illustrates that QDs with larger size would have a smaller energy band gap value, therefore emitting photons with longer wavelengths.

The small energy bandgap between the material of QD and the surrounding semiconductor matrix results in only a few discrete energy levels contained in a QD. Given by the Pauli exclusion principle, the s-shell level could contain up to 2 electron-hole pairs with opposite spins, forming the so-called biexciton energy level (XX). The two pairs recombine subsequently in the XX decay through a cascade via an intermediate X level. The emitted two photons in one cascade, due to the conservation of the QD angular momentum, have opposite spins and thus exhibits a maximally entangled state:

$$|\Phi^+\rangle = \frac{1}{\sqrt{2}}\left(|\sigma^+\sigma^-\rangle + |\sigma^-\sigma^+\rangle\right) \tag{1.8}$$

However, QDs formed under Stranski-Krastanov (SK) growth scheme often suffer from the asymmetric geometry by strain. It results in the so-called fine-structure-splitting (FSS) that negatively influences the fidelity of the generated entangled photon pairs. More information about this will be introduced in chapter 2.

The development has been done over decades on QD devices facilitating integration from multiple aspects. Traditionally, QDs are optically excited, resulting in the so-called photoluminescence (PL) process of QDs. In PL, a laser is injected to the QD, generating carriers and exciting the QD to its biexciton state. In a later development, doping techniques are used during QD growth, forming a positive-intrinsic-negative (p-i-n) diode structure on the wafer with the QDs lying in the intrinsic region. Cleanroom-based semiconductor processing techniques including etching and metal deposition have enabled p-i-n diodes devices fabricated from a wafer where QDs are grown on [56, 57], making electroluminescence (EL) possible. Many designs have been made using this technique, focusing on the improvement of driving conditions and photon extraction efficiency. Radio frequency (RF) signals are applied on the devices confining emitted photons from QDs into packets of pulses with allocated time-slot, having its potential to be used for photon generation compatible with synchronisation [58, 59]. The frequency of the

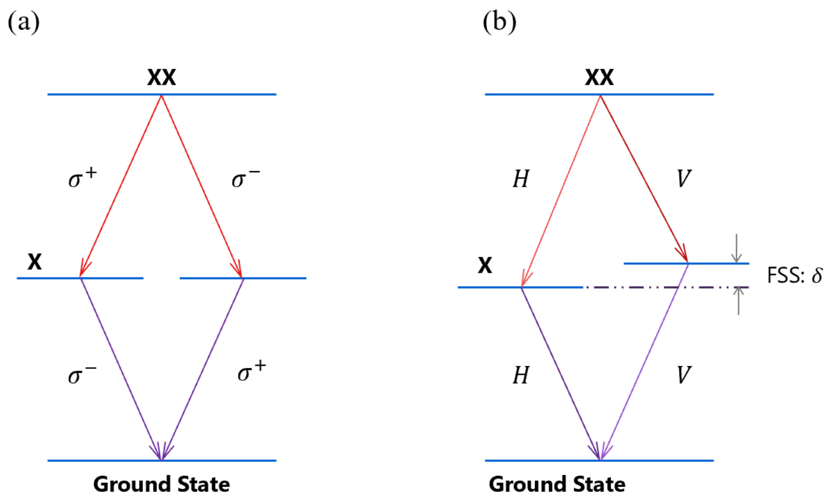

Fig. 1.5 Decay paths of a QD that generates entanglement. An unpolarised photon is generated when the QD decays from the XX neutral state. It leads to an intermediate superposition state for the neutral X. The decay from the X state to the ground state generates another unpolarised photon. (a) shows such a procedure from an ideal symmetric QD. There are two decay paths that are considered to have an intermediate energy level. (b) shows the case in an asymmetric dot. The degeneracy of the X levels is lifted for emitted polarisations corresponding to the crystal axes of the QD. The energy difference of the level δ between the two paths is the so-called FSS.

electrical driving signal has increased from hundreds of MHz [60] to 1 GHz [61, 62], and finally reaching 3 GHz in recent year [63]. Photon extraction efficiency benefits from designs such as micro-pillars [61, 64] and bulls-eyes with circular-Bragg-grating (CBG) [65, 66], enabling high-rate QD single-photon sources. Thus, in general, QDs has the potential to be practically applied as a single photon device with network integration.

The development of quantum dots has also driven forward the development of sub-Poissonian quantum applications. QDs emitting at around 950 nm are firstly developed [51, 67]. Applications were explored such as the entangled-light-emitting-diode (ELED) [56], the quantum relay [34] and the quantum memory [68]. Recent progress has also illustrated their application value in quantum computing [69]. Despite their success for on-chip applications [70], QDs emitting at 950 nm is not compatible with the fibre-based quantum communication network. QDs emitting at the telecom O-band (centred at 1310 nm) and C-band (centred at 1550 nm) have been successfully made [35, 71–73], finally opening up their capability to be practically used in an optical fibre transmission network.

1.4 Network integration of the quantum dot devices

In an ideal scenario, quantum nodes in a network serve critical functions as quantum repeaters and relays, facilitating information transmission among various distantly located users. Sub-Poissonian entangled photon-pair sources are suitable devices to be used in quantum nodes given their capability of providing unconditional security. As entangled single-photon pair generation was enabled by QDs, more effort has been made towards the network integration of QD photon-pair sources, enabling their practical application.

We would structure the development of a QD device compatible with practical network integration into three categories of research topics. The first research topic focuses on photon properties such as small FSS. It will enable higher quantum teleportation or swapping rate, which would become a step toward building a real quantum network. The second focuses on the hardware of the sources, aiming to provide a suitable device design and driving mechanism that favours deployment and photon generation. The third focuses on photon transmission to ensure that the qubit state is maintained over long-distance. In this work, we aim at pushing the development of QD from the aspects corresponding to the second and third research topics.

When considering the network, attempts have been made toward deploying entangled photon sources in the real world. The transmission of the entangled qubits is both in free-space and over deployed optical fibres. Projects at enormous scale have been achieved including a satellite launched with entangled light sources integrated at its payload, which enables entanglement to be achieved at a maximum distance of 1200 km [74]. From the same satellite platform, quantum teleportation, QKD with weak coherent laser pulses [75] and QKD with entanglement [12] have been achieved. However, these approaches also have drawbacks for practical applications. Photons could only travel over one direction - from space to ground. The earth atmosphere introduces the fast variation of diffraction that alters the propagation direction of photons, which makes them impossible to be stably received by a moving satellite. Even for receiving photons on the ground from space, a large receiver with the diameter of one metre has to be installed. Moreover, the system could only perform well at night, due to significant background introduced by sunlight during day time. Entanglement sources deployed onto a satellite need to withstand extreme conditions, which is difficult for entangled single photons sources. Thus, all the work involving entangled photon pairs on this satellite is based on SPDC - a Poissonian light-source. These drawbacks make the satellite-based quantum nodes to be less likely used in a domestic terrestrial network.

An optical fibre-based network is more appropriate to be the network infrastructure of urban-scale quantum communication. The classical optical-fibre network has been well established over the world. They consist of essential elements including users, links and nodes. Information in such a network is sent and received by users that are connected by communication links built upon optical fibre. Nodes are deployed as a combination of relay stations and switches, transmitting specific information to target users. Figure 1.6 shows a map of a fibre network, the

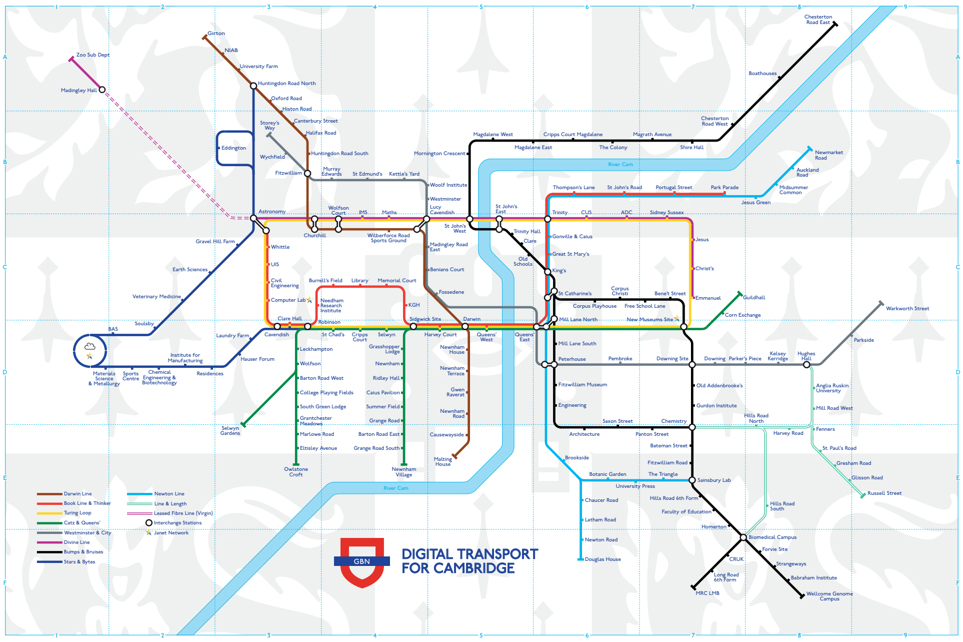

Fig. 1.6 The Cambridge Fibre Network. Network users are located at each location in the city connected via the optical links denoted by different lines on the map. The links go under the road, rivers and reach specific locations inside buildings, during which various noise like vibration and temperature drift is introduced. Under such an environment, the quantum network will also be built and operated. Optical nodes are established at various locations to help route and multiplex communication signal.

Cambridge Fibre Network (CFN), where this project is performed. Part of this work, including correlation measurements, is performed at the Toshiba Cambridge Research Laboratory, linked via deployed fibre shown in black and yellow connected at a node to an office location near the Cavendish Laboratory of the University of Cambridge, where the developed QD entangled photon pair source is installed.

A similar infrastructure could be applied to a quantum network. Quantum bits, or qubits, in short, are generated by quantum light sources such as single-photon emitters or weak coherent laser pulses and detected by avalanche photodiodes (APDs) or superconducting nanowire single-photon detectors (SNSPDs) at user ends. During transmission, they are relayed and routed by quantum nodes which are supposed to include entangled photon sources and detectors to form a quantum repeater or quantum relay. Another critical component in a fibre-based quantum network is the quantum communication channel. They could potentially share the same fibre platform as the classical optical communication network. Optical fibres are deployed in an urban environment typically with disturbance such as temperature variation and vibration. The state that a qubit is encoded in needs to be maintained over the entire transmission distance. Therefore, one important requirement for the optical fibre-based quantum communication and quantum network is to synchronise the photon generation and detection module [76, 77], and stabilise polarisation states [78] or phase of the input light [79]. And therefore a qubit stabilisation system is always required for successful transmission.

Currently, there are a few fibre network infrastructures dedicated for quantum communication in the world such as the UK quantum communication network (currently in operation in Cambridge) [80] and the Tokyo QKD network [81]. Various long-distance urban QKD projects [13, 82–84] with the integration of such a stabilisation system or module have confirmed its success. In comparison, large-scale entanglement transmission is slower in its development. From 2016 on-wards researchers have illustrated successful trials of quantum teleportation [36, 37] over installed optical fibre. Stabilisation systems have been successfully implemented to enable the transmission of time-bin qubits. These trials for the first time illustrated the possibility of distributing entanglement between two distant locations on the earth via an established optical fibre that was previously used in classical communication. However, urban-scale entangled qubits from sub-Poissonian entangled photon-pair sources in the polarisation encoding scheme have not yet been demonstrated. And one of the objectives of this work is to achieve entangled qubit transmission from a QD over an installed fibre in an optical network.

It is worthwhile to consider the QD device for network integration. In realistic cases, an optical fibre network does not always provide a dedicated environment for quantum communication experiments such as a laboratory, and therefore it is preferable to deploy a system containing as little bulky and free-space optics as possible. Hence, optical excitation techniques are not optimal for the device network integration.

Grown QDs vary in sizes and shapes, resulting in different emission wavelengths as well as FSS. Tuneability is thus important if a specific wavelength is required for network-based applications that require the two-photon interference, such as a quantum repeater. Commonly there are three methods for tuning the emission wavelength of a QD. The first method is by strain [60, 71, 85, 86]. In this method, a piezoelectricity material is attached to the QD wafer, which introduces a strain when operated. It, however, requires up to hundreds of volts applied to the material, and such a high voltage is a potential hazard for the QD devices with p-i-n junctions. The second method is via the Zeeman effect by applying a magnetic field [87] to the devices. It, however, requires a magnetic field up to several Tesla, being impractical for real-world application. Hence, we here consider the third method via the quantum-confined Stark effect [88], in which an electric field is applied to the QD [54, 89–91]. The operation requires typically a voltage applied via the deposited metal contacts on the p-type and n-type layer, creating a field in its intrinsic region where the QD is located. This tuning method is, however, not compatible with the electrical excitation, given the voltage or current for exciting the QD also determines the electric field in the intrinsic region.

Attempts have been made on exploring the on-chip optical excitation. As is illustrated in work [92], a whispering-gallery-mode (WGM) laser is fabricated alongside several QD devices. When injecting a current to switch on the WGM laser, the surrounding QDs will be excited. In [93], researchers also discovered the possibility of incoherent excitation, which is done by using the WL emission from one QD device to excite the nearby device. The separation between the pumping source and the QD of interest provides an environment where one can introduce additional electrical fields for the tuneability separated from the excitation. Both devices work on short-wavelength QDs, showing great potential for the on-chip excitation technique in practice, therefore applied in this work. We have optimised the on-chip excitation scheme for 1310 nm QD, both in terms of device design and the wafer structure. This has enabled an electrically driven and tuneable device that is easy to be deployed and operated in an optical fibre network.

1.5 Thesis objectives

This thesis describes details of a network integration of QD entangled photon-pair sources that take place in Cambridge. We divide the thesis into eight chapters including introduction, with their content introduced as follows,

Chapter 2 focuses on the background regarding InAs QDs emitting at the telecom O-band. Various methods for QD characterisation including the measurement of FSS, single-photon purity and entanglement fidelity of the emitted photon pairs are introduced.

Chapter 3 concentrates on the device design that supports network integration. A tuneable QD device with electrical operation by using the on-chip pumping technique is designed and fabricated. The QD characterisation is also carried out to investigate the performance of the device.

Chapter 4 deals with the entangled photon pair transmission in a field environment. We developed a polarisation stabilisation system to compensate for the polarisation states variation introduced by the fibre birefringence variance as it occurs in installed networks.

Chapter 5 focuses on the remote correlation measurement. We discuss the drawbacks and limitations for the current system for aligning the polarisation correlation measurement bases in a remote environment and propose a new method for bases alignment.

Chapter 6 deals with a classical communication required for devices and components operation during the network integration. A multiplexed system is designed to support the transmission of quantum and classical signals over the same fibre.

Chapter 7 describes the device and system deployment.

Chapter 8 is the summary of this thesis, with the future works proposed for the following development.

Chapter 2

Telecom O-band Quantum Dot

2.1 Emission from the InAs quantum dot

The sub-Poissonian photon source in this work is an InAs QD, emitting entangled photon pairs at the telecom O-band. Therefore, prior to introducing various technologies for its network integration, we would, in this chapter, discuss the source itself and its emitted entangled photon pairs. A measurement of entanglement has been carried out using a QD developed in previous works for the preparation of the network integration of sub-Poissonian entangled photon-pair sources.

Emission from QDs is mainly determined by its wafer structure. An overall schematic of the wafer cross-section in this work is illustrated in Figure 2.1, in which the QDs are formed under SK process, as is illustrated in Section 1.3. Surrounded by GaAs and AlGaAs, a dual-QW structure is formed with increasing bandgap energy from InGaAs, GaAs to AlGaAs. The high energy barriers of the QWs prevent the carriers from tunnelling out, therefore introducing strong confinement which favours the recombination of electron-hole pairs at QDs.

Doped stacked DBR mirrors made from GaAs/AlGaAs surround the QW. They consist of 17 repeats underneath the QD layer, and one repeat on the top. The DBR forms a weak vertical $\lambda/2$ cavity to enhance the emission from the QD around the centre of the telecom O-band toward the vertical direction, which helps to suppress the background at the wavelengths outside of the O-band when detecting entangled photon pairs.

Generation of entangled photon pairs would require excitation process that brings a QD from its ground state to the XX state. Here we apply the optical excitation to the QD to realise its photoluminescence (PL). Highly coherent photons could be generated by a so-called resonance fluorescence excitation when the exciting laser is at the same wavelength as QD photons. It, however, requires polarisation filtering to separate the excitation light from the emitted photons, given spectral filtering is impossible. When the QD is used as entangled photon pair sources, polarisation filtering collapses the entanglement prior to the correlation measurement, incompatible with this work. A scheme called resonant two-photon excitation is

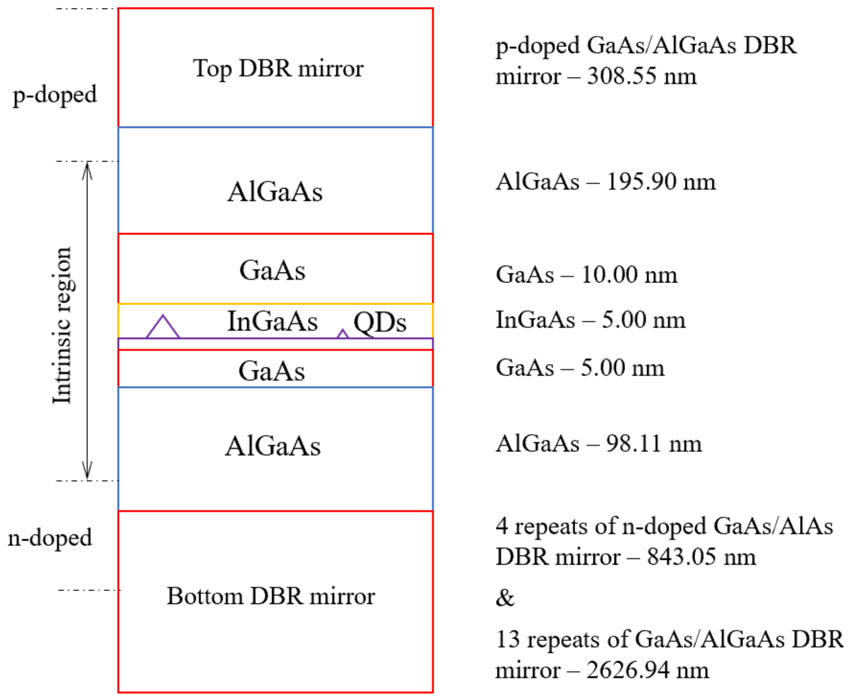

Fig. 2.1 Details of the wafer used in this work based on its layered structure.

applied [94, 95] with laser pulses tuned to half of the energy difference between XX and ground state. In terms of the wavelength, it is located at the centre of the XX and X photons, hence could be applied with spectral filtering. We, in this work, consider an alternative method which is non-resonant excitation in this work.

Non-resonant excitation schemes use a laser that emits light at higher energy than the entangled photon pairs from QDs. The coherence time of the generated photons in this scheme is shorter compared with resonance excitation due to stronger homogenous and inhomogeneous spectral broadening [96, 97]. It is compatible with spectral filtering; therefore entangled photon pairs could be obtained with the little background generated from the excitation laser. Non-resonant excitation could be classified to be above or below-band excitation. When the excitation laser energy is above the bandgap of the material surrounding QDs (GaAs in this case), electron-hole pairs are generated at GaAs and fall into the potential well of the QD subsequently. It, therefore, does not require the laser to focus on the exact QD directly. Such a feature facilitates the excitation of QD, useful for QD characterisation. In below-band excitation scheme, the excitation power is smaller than the surrounding semiconductor bandgap but higher than the QD bandgap. The electron-hole pair is directly generated at the QD, therefore requires the direct focus. Given that its laser energy is closer to the QD bandgap compared with above-band excitation, it is expected that the entangled photon pairs are generated with less trapped charges, resulting in longer coherence time in below-band excitation.

Here we introduce a micro-photoluminescence setup for applying non-resonant excitation and collecting the QD emission, as is shown in Figure 2.2. A sample of QDs is held at cryogenic

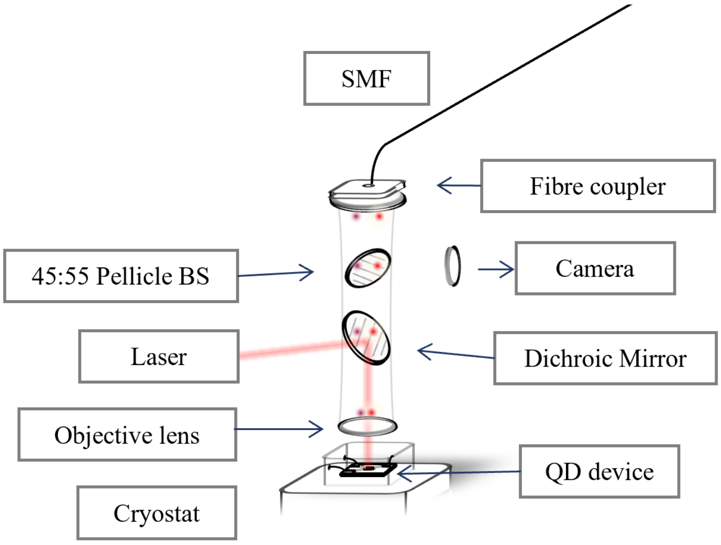

Fig. 2.2 A micro-photoluminescence (PL) setup installed above the QD for its excitation and emission collection. The QD is installed in the cryostat cooled to cryogenic temperature. The microscopic setup contains a set of confocal lenses to collect the emission light from the QD. A dichroic mirror is installed above the objective lens for the excitation laser to be injected. A camera is installed for observation, connected to the setup via a 45:55 Pellicle Beam Splitter (BS). The micro-PL setup is integrated with a Picomotor translation stage controlled by a PC. It is to move the collection spot over the entire devices to inspect different QDs.

temperatures in a cryostat, cooled by liquid helium. Above it is a confocal microscope setup to collect the emitted light from the QD into a single-mode fibre (SMF). A 45:55 pellicle beam splitter (BS) is installed before the collection, splitting a part of the light to an InGaAs camera sensitive at the telecom O-band. The exciting laser is injected into the collection path with an inserted dichroic mirror and focused down to the surface of the semiconductor sample by an objective lens.

Another process that could be used for QD excitation is to electrically excite QDs, realising a so-called Electroluminescence (EL). During the wafer growth, the top- and bottom-cavities are respectively p- and n-doped, forming a p-i-n diode structure on the wafer with the QDs lying in the intrinsic region. In EL, carriers are injected via a voltage or current applied to the QD p-i-n junction. It normally requires device processing to deposit metal contacts to the positive and negative region of the wafer, which is then packaged as a chip-like semiconductor device connected to the power supply. We have witnessed works on compact QD device design which all apply electrical injection [56, 61]. EL devices have a great advantage in network integration as they require no excitation laser to be installed. However, EL excitation severely broadens the QD emission at the telecom O-band in this work, potentially due to the second QW with lower energy barriers introduced by the strain-relaxation layer. When a high positive voltage is applied on the QD p-i-n junction, the energy shift is beyond the extent that could be treated as a perturbation, and the carriers partly recombine outside of the QD. This undermines the entanglement from the QD emission. Therefore in this work, PL is applied for QD characterisation.

2.2 Characteristics of the quantum dot emission light

A large number of QDs could be formed on a wafer in a single growth with varying optical properties. Choosing an appropriate candidate QD is often required before the rest of the experiments. Characterisation of QDs is therefore essential.

2.2.1 Fine structure splitting and its measurement

The QD formation procedure in the SK mode is yet non-ideal. The strain forms InAs QDs on GaAs, simultaneously introducing a preferred elongation along the crystal lattice [110] direction. Therefore the QD emission has linear eigenstates $|H\rangle$ and $|V\rangle$ corresponding to its elongated shape. Structural properties of the dot such as elongation and strain cause in-plane asymmetry of the exciton wavefunction introduce the QD FSS [98, 99], generating a slight energy difference between two decay paths corresponding to its emission eigenstates. An illustration of the FSS is shown in Figure 2.3 (a).

After decay from XX to X, the states remained on X for a certain time τ. During this period, a phase difference between the two intermediate states develops due to the FSS, as is shown in Figure 2.3 (b). The entangled photon pairs emitted from the QD therefore has a phase difference in its polarisation correlation depending on time τ on the superposition states. The final two-photon state is:

$$|\Phi^+\rangle = \frac{1}{\sqrt{2}}(|\mathrm{H_X H_{XX}}\rangle + e^{i\frac{\delta}{\hbar}\tau}|\mathrm{V_X V_{XX}}\rangle) \tag{2.1}$$

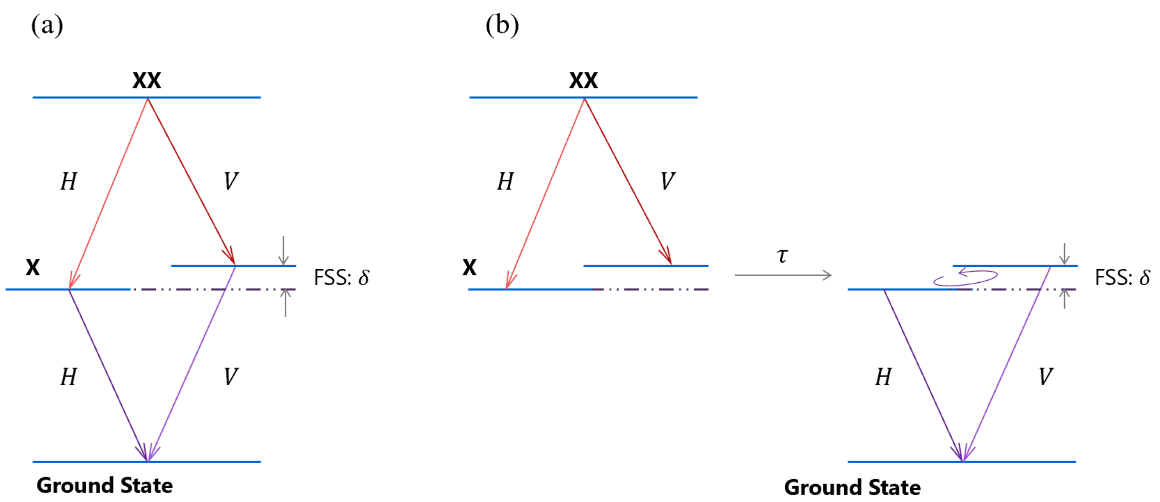

Fig. 2.3 (a) The degeneracy of the X levels is lifted for emitted polarisations corresponding to the crystal axes of the QD. The energy difference of the X level δ between the two paths corresponding to QD emission eigenbasis is the so-called FSS. (b) The FSS introduces a time-dependent phase oscillation in superposition states between XX photons and X photons.

in which δ represents the FSS energy. This FSS would result in a time-dependent oscillation on the polarisation correlation between XX and X photons. Given that any detectors have a certain time resolution, the measured entanglement fidelity corresponds to an average fidelity in the time period of the detector's resolution. Given by equation 2.1, a larger FSS would result in a shorter oscillation period, leading to a more significant fidelity drop given the limited detector resolution. Moreover, only photons contained in the first oscillation period of one emission would be used, resulting in a reduced rate for QDs with larger FSS. Therefore, among all the grown QDs, we selected ones that have small FSS for correlation measurements.

We here introduce a typical setup for inspecting the FSS of QDs. Its schematic is shown in Figure 2.4. The emitted photons from the micro-PL setup directly reach a FSS analyser consisting of a quarter-wave plate (QWP) and a linear polariser (LP). While rotating the QWP, different polarisation component of the photons is sent to the connected spectrometer after the analyser. We hence would notice a wavelength shift of XX and X photons.

The value of the QD FSS could be obtained via operations on the spectral analysing setup. As is introduced previously, the FSS results in an energy level difference of the X state for two different decay paths, represented by their density matrix [100]:

$$\hat{H}s_1 = E_H|H\rangle\langle H| + E_V|V\rangle\langle V| \tag{2.2}$$

in which s_1 is the eigenstate of the Hamiltonian $\hat{H}$ given:

$$s_1 = |H\rangle\langle H| + |V\rangle\langle V| \tag{2.3}$$

E_H and E_V in equation 2.2 are the X energy of the two decay paths with a FSS $\delta = (E_H - E_V)$.

The introduced transformation from the optical fibre between QD and the setup generates a rotation θ and a phase ϕ to the original state. We use states $|H'\rangle = \cos(\frac{\theta}{2})|H\rangle + \sin(\frac{\theta}{2})e^{i\phi}|V\rangle$ and $|V'\rangle = \sin(\frac{\theta}{2})|H\rangle - \cos(\frac{\theta}{2})e^{i\phi}|V\rangle$. The eigenstate of the function is then changed to s_2:

$$s_2 = \frac{1+p}{2}|H'\rangle\langle H'| + \frac{1-p}{2}|V'\rangle\langle V'| \tag{2.4}$$

where p is the degree of polarisation of the entangled photons from the QD.

By rotating the QWP, we are selecting different polarisation components passing the LP, which could be observed as a shift of the spectrum. This operation could be written in the following measurement basis:

$$|M\rangle = QWP(\chi)|H\rangle = \frac{\sqrt{2}}{2}(i+\cos(2\chi))|H\rangle + \frac{\sqrt{2}}{2}\sin(2\chi)|V\rangle \tag{2.5}$$

in which χ represents the rotation angle of the QWP. The energy measurement result on the spectrometer could then be written given input eigenstate s_2 as:

$$E(\chi) = \frac{\langle M|\hat{H}s_2|M\rangle}{\langle M|s_2|M\rangle} = \frac{E_1+E_2}{2} + \frac{\delta}{2}\left(\frac{(a_1(\chi)-a_2(\chi))+p}{1+p(a_1(\chi)-a_2(\chi))}\right) \tag{2.6}$$

Here, $a_n(\chi) = |\langle M(\chi)|B_j\rangle|^2$, based on which we obtain

$$a_1(\chi) - a_2(\chi) = \frac{1}{2}(\cos\theta\,(1+4\cos 4\chi) + \sin\theta\sin 4\chi\cos\phi - 2\sin\theta\sin 2\chi\sin\phi) \tag{2.7}$$

Given the average energy of XX and X photons $\frac{E_1+E_2}{2}$ are constant, we here investigate the energy variation caused by FSS:

$$\Delta E(\chi) = -\frac{\delta}{2}\left(\frac{2p+\cos\theta\,(1+4\cos 4\chi)+\sin\theta\sin 4\chi\cos\phi - 2\sin\theta\sin 2\chi sin\phi}{2+p(\cos\theta\,(1+4\cos 4\chi)+\sin\theta\sin 4\chi cos\phi - 2\sin\theta\sin 2\chi\sin\phi)}\right) \tag{2.8}$$

Here we review the above analysis once again. Despite the slight energy difference of $|H\rangle\langle H|$ and $|V\rangle\langle V|$ decay paths, the QD light is overall non-polarised as the FSS δ is negligible compared with the overall photon energy. Therefore, the DOP p of QD emission is near zero. Hence, the energy deviation ΔE are:

$$\Delta E(\chi) = -\frac{\delta}{4}(\cos\theta\,(1+4\cos 4\chi) + \sin\theta\sin 4\chi\cos\phi - 2\sin\theta\sin 2\chi sin\phi) \tag{2.9}$$

The above function does include not only QD FSS information, but also the rotation θ and ϕ by the transformation of the optical fibre. While rotating the QWP, the spectrometer would record a spectral shift. Hence, one could obtain the central wavelength λ of the emitted photons by performing a Gaussian fitting on the XX/X spectral line using the following equation:

$$I(\lambda) = Ae^{(-\frac{\lambda-\lambda_0}{2\sigma^2})} + bg \tag{2.10}$$

in which A is the scaling factor of the intensity of the measured photons, λ_0 is the central wavelength and bg is the background count rate. The photon energy E is therefore:

$$E = hc/\lambda \tag{2.11}$$

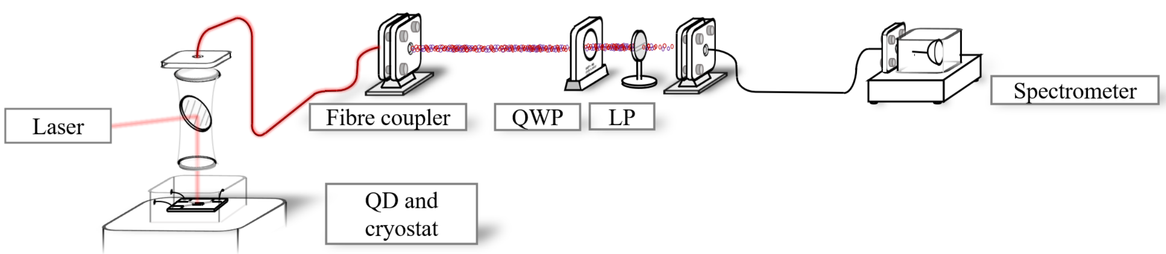

Fig. 2.4 Experimental setup for measuring the photon count rate and FSS. The QD is placed in a cryostat, and a micro-PL setup is installed above for QD excitation and photon collection. The emitted photons are connected to a FSS measurement setup, consisting of a quarter-wave plate (QWP) and a linear polariser (LP) as an analyser, and a spectrometer for measuring the photon energy.

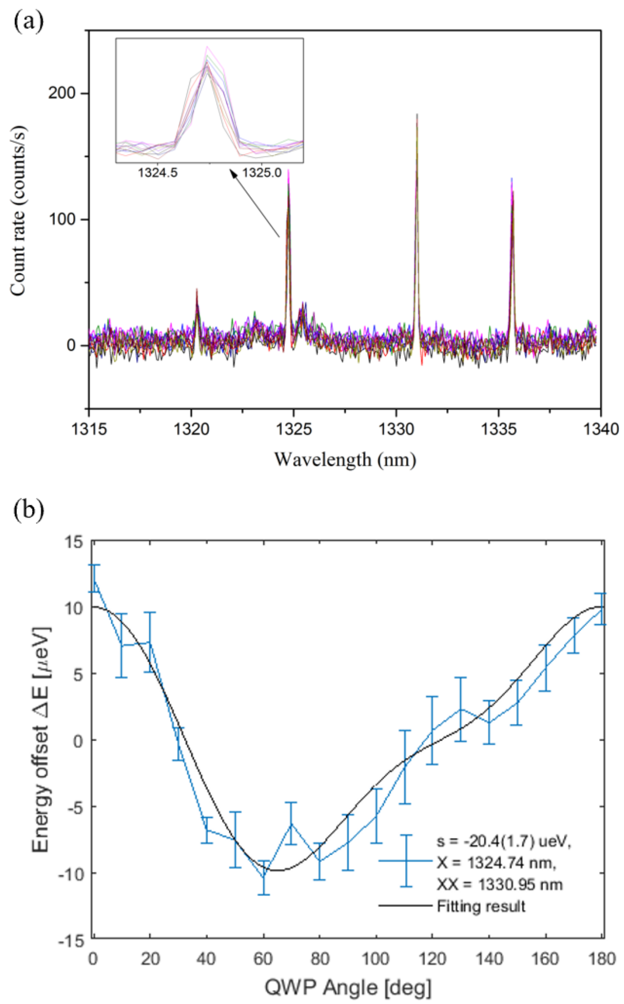

Fig. 2.5 (a) A set of InAs QD emission spectra measured by the spectrometer in the FSS measurement setup with QWP rotating by a 10°step size. The X photon energy shift with respect to the QWP rotation could be observed. (b)The change of XX/X energy offset with the QWP rotation angle is shown in blue. And a curve fitting the energy offset is shown in black. From such fitting, we obtain the FSS value of $20.4 \pm 1.7\,\mu$eV

where h is the Planck constant. We therefore obtain the energy difference with the QWP rotation angle χ: $\Delta E(\chi)$.

We here show a measurement on the emission spectra of an InAs QD with the rotation of QWP by a step size of 10° in Figure 2.5 (a). One could notice the wavelength shift of X photons with respect to QWP rotation. We fit the XX and X photon with a Gaussian curve and plot the energy offset with the rotation angle in Figure 2.5 (b). By fitting a curve using equation 2.9, one could obtain the FSS value of the measured QD.

The varying geometry from growth results in QDs grown on the same wafer has significantly different FSS from around $5\,\mu$eV up to more than $150\,\mu$eV. Setting up a threshold for an acceptable FSS value is important for searching a workable QD. We select those with FSS value less than $10\,\mu$eV, considering the detector being a conventional APD for QKD systems with 170 ps jitter. This value is obtained via a calculation based on an analysis of QD FSS corresponding to its entanglement fidelity deterioration. See Subsection 2.3.3 for more detail.

2.2.2 Emission intensity and single-photon property

Spectral analysis in the FSS measurement would allow us to identify emitted XX and X photons by their wavelengths. Therefore entangled photon pairs could be separated from the background by passing through a spectral filter. We in this work uses superconducting nanowire single-photon detectors (SNSPDs) to detect photons. The observed count rate of XX and X varies from tens of up to several hundred kHz, each directly measured by the SNSPDs with efficiency around 65%.

QDs with a good single-photon property requires a low probability of multi-photon contained in a pulse. It is estimated by measurement of the second-order autocorrelation function ($g^{(2)}$). The experimental setup is shown in Figure 2.6. The emitted XX and X photons are separated from the background by a spectral filter and split by BSs before reaching SNSPDs. During the measurement, two SNSPDs corresponding to a single output are connected to a time-correlated single photon counting (TCSPC) system, with the signal from one SNSPD used as the synchronisation signal. It allows a measurement of the $g^{(2)}$ of both XX and X photons to be obtained by performing a time-correlation on their corresponding SNSPDs signal (SNSPD 1 and 2 for XX photons; SNSPD 3 and 4 for X photons) with the following relation:

$$g^{(2)}(\tau) = \frac{\langle n_1(t)n_2(t+\tau)\rangle}{\langle n_1(t)\rangle\langle n_2(t+\tau)\rangle} \tag{2.12}$$

where $n_1(t)$ and $n_2(t)$ represents the count rates at time t on the two SNSPDs respectively. τ is the time delay between two SNSPDs. When detecting sources with higher single-photon purity, there is a smaller possibility that both detectors would detect a photon simultaneously (the so-called anti-bunching), resulting in a $g^{(2)}(0)$ value more toward 0. The $g^{(2)}(t)$ value gradually rises with the time delay, following a curve determined by the photon lifetime and excitation rate. Ideally, the measurement result could be described by a fitting function taking a single excited state into account:

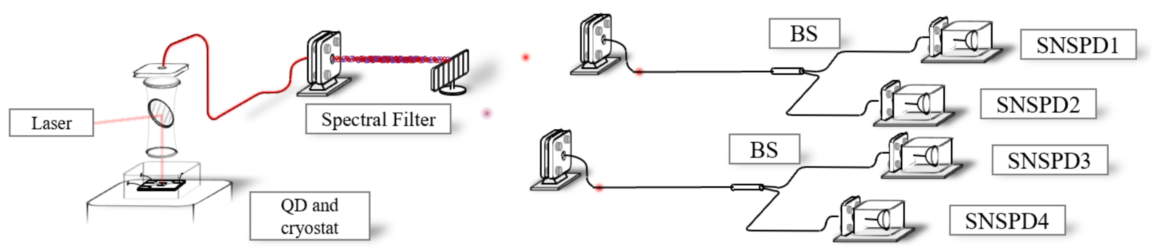

Fig. 2.6 Second-order autocorrelation measurement setup. Emitted light from QD passes through a spectral filter where the XX and X photons are separated. Each output is then connected to a BS and two SNSPDs. Correlations are acquired using a time-correlated single-photon counting (TCSPC) system that is not shown in the figure.

$$g^{(2)}(t) = 1 - e^{-\frac{|t-t_0|}{\tau_1}} \tag{2.13}$$

where τ_1 is the photon lifetime. Due to a long-lived shelving state such as a dark state accessible by a spin flip, a stronger bunching, meaning that a greater possibility to detect photons at two output ports simultaneously, at a short delay could often be noticed. It could be captured by adding a third level to the simple two-level system often used to model X emission:

$$g^{(2)}(t)_{3L} = 1 - (1+A)e^{-\frac{|t-t_0|}{\tau_1}} - Ae^{-\frac{|t-t_0|}{\tau_2}} \tag{2.14}$$

where τ_2 is the timescale of the additional decay processes with A being its coupling strength. For fitting the X photon emission without considering the background, this three-level function is applied. However, for $g^{(2)}(t)$ on XX photons, an additional level is necessary, potentially due to more existing long-lived shelving states [101]. Hence we use:

$$g^{(2)}(t)_{4L} = 1 - (1+A+B)e^{-\frac{|t-t_0|}{\tau_1}} - Ae^{-\frac{|t-t_0|}{\tau_2}} - Be^{-\frac{|t-t_0|}{\tau_3}} \tag{2.15}$$

as the function for XX and X photons. Similarly, τ_3 and B represents the timescale and coupling strength for the new level.

It is important to take the background into consideration for fitting. We define the function

$$g^{(2)}(t)_{bg} = \frac{|g^{(2)}(t)^2_{xL} + bg|^2}{(|g^{(2)}(t)_{xL}| + bg)^2} = \frac{g^{(2)}(t)^2_{xL} + 2bg + bg^2}{(1+bg)^2} \tag{2.16}$$

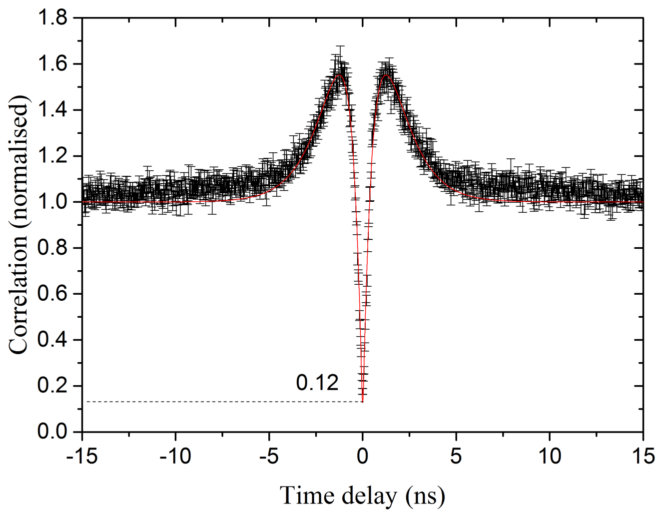

Fig. 2.7 Second-order correlation measurement on emitted XX photons from an InAs QD (dot 4), which was also used in the previous work [35, 102].

which is used to describe the cases with correlations of signal and background counts taken into account. Figure 2.7 shows one result of a second-order correlation measurement on XX photons emitted from an InAs QD (dot 4), which was as well used in previous works [35, 102]. We notice its $g^{(2)}(0)$ reaches 0.12, well below a threshold $g_{th}^{(2)}(0) < 0.5$ for a source that shows a good single photon property [103]. The background calculated from equation 2.16 is 6.6%.

2.3 Entanglement fidelity evaluation

In an entanglement-based quantum communication system, the quantum bit error rate (QBER) in the four dimensional case is calculated as (supplementary of [104]):

$$QBER = \frac{2}{3}(1-F) \tag{2.17}$$

where F is the entanglement fidelity. Therefore, high fidelity entanglement is required for a low QBER, leading to better security in a quantum network. Ideally XX and X photon pairs are fully entangled due to the angular momentum conservation. The entanglement fidelity, however, could drop due to the imperfection of the measurement and the imperfection of the source including high QD FSS. In this section, we introduce a method for evaluating entanglement fidelity based on the polarisation correlation measurement and provide the relevant analysis on how it is influenced by detection basis misalignment and FSS.

2.3.1 Evaluation of entanglement fidelity by the polarisation correlation measurement

The polarisation-encoded entanglement could be evaluated by the measurement of correlation coefficients in three orthogonal polarisation bases on the Poincaré sphere. Let us assume that the detection system is aligned for projection to a randomly oriented polarisation state $|H'\rangle$ described by its corresponding rotation angle θ and phase difference ϕ in spherical coordinates on the Poincaré sphere:

$$|H'\rangle = \cos\frac{\theta}{2}\,|H\rangle + \sin\frac{\theta}{2}e^{i\phi}\,|V\rangle \tag{2.18}$$

Revisiting the entangled Bell-state with FSS represented in equation 2.1, we project XX photons to the $|H'\rangle$ basis, collapsing the exciton photon into state:

$$|P'_X\rangle = \langle\, H'_{XX}|\;\;\phi\,\rangle = \cos\frac{\theta}{2}\,|H_X\rangle + \sin\frac{\theta}{2}e^{i(\frac{\delta}{\hbar}t\,-\,\phi)}\,|V_X\rangle \tag{2.19}$$

The probability for the detection of a co-polarised coincidence between X and XX photons is then described by:

$$p_{co} \;=\; |\langle\, P'_X \mid H'\,\rangle|^2 = (1\;-\;2\;\sin^2\frac{\theta}{2}\;\cos^2\frac{\theta}{2}\;(1\;-\;\cos(\;\frac{\delta}{\hbar}t\;-\;2\phi))) \tag{2.20}$$

The correlation coefficients is defined as the contrast of co- and cross-polarised polarisation correlation value, calculated by:

$$C_{PQ} = (2p_{co}-1)e^{-\frac{t}{\tau}} \tag{2.21}$$

where τ is a constant accounting for exponential decay of the photon correlation due to the natural lifetime of the X state and other spin dephasing processes including repumping.

When considering the rotation and phase of $|H\rangle$, $|D\rangle$ and $|R\rangle$ polarisation states as follows:

$$\begin{aligned}\theta_H &= 0, \phi_H = 0\\ \theta_D &= 90^\circ, \phi_D = 0\\ \theta_R &= 90^\circ, \phi_R = 90^\circ\end{aligned} \tag{2.22}$$

Thus in an ideal case, the correlation coefficients for $|H\rangle|V\rangle$, $|D\rangle|A\rangle$ and $|R\rangle|L\rangle$ are calculated as:

$$\begin{aligned}C_{HV} &= e^{-\frac{t}{\tau}}\\ C_{DA} &= \cos(\frac{\delta}{\hbar}t)e^{-\frac{t}{\tau}}\\ C_{RL} &= -\cos(\frac{\delta}{\hbar}t)e^{-\frac{t}{\tau}}\end{aligned} \tag{2.23}$$

based on the above relationship and equation 2.21. The fidelity is evaluated using the following equation as is derived in a previous work [54]:

$$\mathscr{F} = \frac{1 + C_{HV} + C_{DA} - C_{RL}}{4} \tag{2.24}$$

Its form in an ideal case is therefore:

$$\mathscr{F} = \frac{1 + (1 + 2\cos(\frac{\delta}{\hbar}t))e^{-\frac{t}{\tau}}}{4} \tag{2.25}$$

Here, we have noticed that fidelity at zero-delay has a value 1.

2.3.2 Correlation measurement and bases alignment setup

To perform correlation measurements, we here introduce a typical setup [105] illustrated in Figure 2.8. Here, the QD is installed in a vapour cryostat. The objective lens is placed in the cryostat. Therefore it could support lenses with a higher numerical aperture (NA) of 0.7 compared with 0.5 in the micro-PL setup. It gives a great advantage in that more emitted photon pairs could be collected. It as well provides more robust mechanical stability for the collection setup, therefore usually used for QD characterisation.

We directly inject a polarisation reference on top of the cryostat. It is generated using a light-emitting-diode (LED) at the telecom O-band and modulated by a setup consisting of a LP, a HWP and a QWP. A flip mirror is installed in the collection optical path after the dichroic mirror, operated to send either QD emission light or the polarisation reference to the correlation

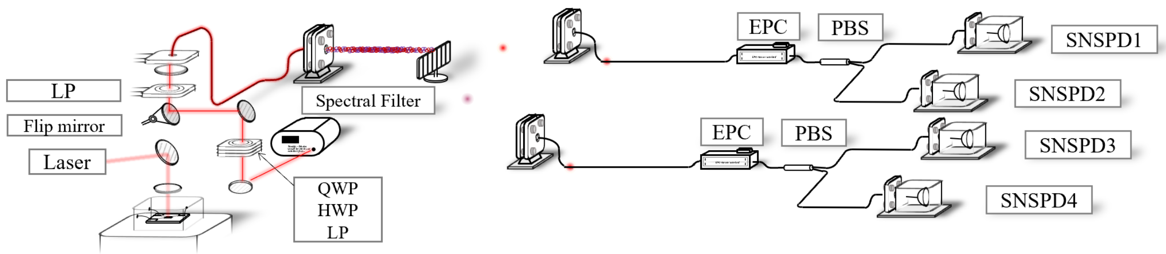

Fig. 2.8 A traditional method for aligning the measurement bases to the QD emission eigenbasis. The QD is installed in a vapour cryostat. A polarisation reference is installed above the cryostat, generated by a LED. Its polarisation is controlled by a polarisation modulation unit consisting of a LP, a HWP and a QWP. A flip mirror is installed to select whether QD light or the references are injected to the detection systems. The light passes a spectral filter and reaches a correlation detection module. The module consists of an electronic polarisation controller (EPC) and a polarising beam splitter (PBS) with two output ports connected to two SNSPDs each.

detection module. Before the fibre coupler, we introduce a LP to analyse the polarisation state of the light.

In the detection module, instead of a BS before each pair of SNSPDs as is in the second-order correlation measurement, we connect an electronic polarisation controller (EPC) and a polarising beam splitter (PBS). By controlling EPCs, we can select to which polarisation state the entangled photon pairs are collapsed.

We initiate the alignment by finding the QD emission eigenbasis. While keeping the LP before the fibre coupler in the light path, we flip the mirror out of the optical path to inject the QD emission light. The XX/X photons are thus collapsed to a linear state. Due to the FSS, the corresponding XX (or X) photon energy for decay path of $|H\rangle|H\rangle$ and $|V\rangle|V\rangle$ are at different level (Figure 2.3). Hence the measured X photon energy E_X corresponding to the LP rotation angle β with its eigenbasis could be represented by the following equation:

$$E_X = \frac{E_{XH} + E_{XV}}{2} + \frac{\delta}{2}\cos(\beta - \beta_0) \tag{2.26}$$

where E_{XH} and E_{XV} are the maximal and minimal emission energy of X photon corresponding to QD eigenbasis. β_0 is the offset angle between the initial position of the LP and the QD eigenbasis. We hence rotate the LP by 5° steps and acquire the spectra to find the rotation angle that corresponds to the highest X photon energy. The photon emission profile can be estimated by the same Gaussian curve in equation 2.10 around its central wavelength. The fitting would provide us with a relation of an emission energy shift with respect to the LP rotation angle. It is then by another fitting to equation 2.26 that we can find the rotation angle with the shortest wavelength of XX photon, corresponding to the QD eigenbasis.

We rotate the LP to the angle corresponding to the QD eigenbasis and connect the polarisation reference to the system by flipping the mirror in the microPL setup. By rotating the HWP and the QWP in the polarisation modulation unit after the LED, the polarisation states of the injected references to the microPL setup will be changed and reflected on the varying count rate shown on the SNSPD. The state could be analysed by minimising the photon count rate on one of the SNSPDs connecting to the target XX or X photons. And the rotation angle of the HWP and QWP are recorded as their zero-angle.

Then we rotate HWP and QWP to align the references to the superposition states. To acquire the rotation angles, we use Jones calculus for its analysis. In Jones calculus, one polarisation state could be written as a vector containing two complex amplitudes of field E_x and E_y respectively on their horizontal (x-axis) and vertical (y-axis) directions. In this case, a state is written in a Jones vector as:

$$E = \begin{bmatrix} E_x \\ E_y \end{bmatrix} = \begin{bmatrix} A_x e^{i\phi_x} \\ A_y e^{i\phi_y} \end{bmatrix} \tag{2.27}$$

in which A_x and A_y represent the amplitudes of the light electric field in the horizontal and vertical direction. ϕ_x and ϕ_y represent the corresponding phases. To simplify the analysis, we set the default amplitude and phase of a Jones vector corresponding to its x-component; hence the Jones vector is transformed into

$$E = \begin{bmatrix} \cos\theta \\ \sin\theta e^{i\phi} \end{bmatrix} \tag{2.28}$$

where θ is the rotation angle of the light with respect to horizontal direction, and ϕ is the phase difference between electric fields at horizontal and vertical directions. Therefore, the electric fields of polarisation states $|H\rangle$, $|D\rangle$ and $|R\rangle$ are written as:

$$E_H = \begin{bmatrix} 1 \\ 0 \end{bmatrix} \quad E_D = \begin{bmatrix} \frac{\sqrt{2}}{2} \\ \frac{\sqrt{2}}{2} \end{bmatrix} \quad E_R = \begin{bmatrix} \frac{\sqrt{2}}{2} \\ \frac{\sqrt{2}}{2} i \end{bmatrix} \tag{2.29}$$

Linear transformation of polarisation states, including waveplates, polarisers and fibre birefringence-induced polarisation shift could be represented by matrices A

$$A = \begin{bmatrix} a_{11} & a_{12} \\ a_{21} & a_{22} \end{bmatrix} \tag{2.30}$$

to transform the input polarisation, E_0, to the output polarisation, E_1 by

$$E_1 = AE_0 \tag{2.31}$$

In this polarisation analyser, HWP, QWP and LP have the following Jones Matrices A_H, A_Q, A_L when aligned with 0 degree with respect to the reference direction (horizontal normally) [106]:

$$A_H = \begin{bmatrix} 1 & 0 \\ 0 & -1 \end{bmatrix} \quad A_Q = \begin{bmatrix} 1 & 0 \\ 0 & i \end{bmatrix} \quad A_R = \begin{bmatrix} 1 & 0 \\ 0 & 0 \end{bmatrix} \tag{2.32}$$

Waveplates and LPs are normally rotated as components to generate polarisation variations. In Jones Calculus, a rotation with angle α on the component with a transformation matrix A could be represented by equation $A' = R(\alpha)AR^{-1}(\alpha)$, in which $R(\alpha)$ is:

$$R(\alpha) = \begin{bmatrix} \cos(\alpha) & -\sin(\alpha) \\ \sin(\alpha) & \cos(\alpha) \end{bmatrix} \tag{2.33}$$

Thus, a rotated HWP by α and a rotated QWP by β could be denoted by:

$$\begin{aligned} A'_H(\alpha) &= \begin{bmatrix} \cos(2\alpha) & -\sin(2\alpha) \\ \sin(2\alpha) & -cos(2\alpha) \end{bmatrix} \\ A'_Q(\beta) &= \begin{bmatrix} \cos^2(\beta) + i\sin^2(\beta) & \frac{1-i}{2}\sin(2\beta) \\ \frac{1-i}{2}\sin(2\beta) & i\cos^2(\beta) + \sin^2(\beta) \end{bmatrix} \end{aligned} \tag{2.34}$$

Hence, the overall transformation equation from light with an input state E_0 is

$$E_o = A'_Q(\beta)A'_H(\alpha) \begin{bmatrix} 1 & 0 \\ 0 & 0 \end{bmatrix} \begin{bmatrix} E_x \\ E_y \end{bmatrix} = \begin{bmatrix} e_1 E_x \\ e_2 E_x \end{bmatrix} \tag{2.35}$$

in which

$$e_1 = \cos(2\alpha)(\cos^2\beta + i\sin^2\beta) + \frac{1-i}{2}\sin(2\alpha)\sin(2\beta) \tag{2.36}$$

$$e_2 = \frac{1-i}{2}\cos(2\alpha)\sin(2\beta) + \sin(2\alpha)(i\cos^2\beta + \sin^2\beta) \tag{2.37}$$

For example, when $\alpha = 22.5°$ and $\beta = 45°$,

$$E_1 = \begin{bmatrix} \frac{\sqrt{2}}{2}E_x \\ \frac{\sqrt{2}}{2}E_x \end{bmatrix} \tag{2.38}$$

From the above equation, we work out the following relations:

HWP	QWP	Jones Vector	Polarisation state
0°	0°	$[1 \quad 0]^T$	H
0°	45°	$[1 \quad i]^T$	R
22.4°	45°	$[1 \quad 1]^T$	D

Table 2.1 Waveplates rotation angle and output polarisation states.

It is noticeable that Jones vectors span the space of full-polarised light. For partially polarised light, it is worthwhile to introduce the concept of the Stokes vector, which is closely related with the Poincaré sphere expression of the polarisation states of the light. Stokes vectors have the following form:

$$S = \begin{bmatrix} s_0 \\ s_1 \\ s_2 \\ s_3 \end{bmatrix} \tag{2.39}$$

where s_0, s_1, s_2, s_3 are Stokes parameters that represents the intensity and polarisation ellipse parameters. It has the following relationship with the corresponding Jones vectors of the state $|S\rangle$ [107]:

$$\begin{aligned} s_0 &= A_x^2 + A_y^2 \\ s_1 &= A_x^2 - A_y^2 \\ s_2 &= 2A_xA_y\cos\phi \\ s_3 &= 2A_xA_y\sin\phi \end{aligned} \tag{2.40}$$

The so-called Stokes vector. It corresponds to the coordinate value of the state on the Poincaré sphere. Here we consider the state $|S\rangle$ on the Poincaré sphere in Figure 2.9 with two rotations θ_p and ϕ_p. The Stokes vector of the state $|S\rangle$ is:

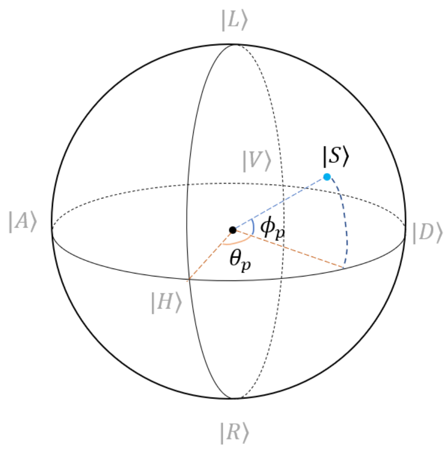

Fig. 2.9 A polarisation state on the Poincaré sphere $|S\rangle$. We introduce θ_p and ϕ_p to represent two rotations of the polarisation state on the sphere with respect to the horizontal polarised state $|H\rangle$

$$\begin{aligned} s_0 &= I \\ s_1 &= Ip\cos\theta_p\cos\phi_p \\ s_2 &= Ip\sin\theta_p\cos\phi_p \\ s_3 &= Ip\sin\phi_p \end{aligned} \tag{2.41}$$

Where I is the intensity of the light and p is the degree of polarisation (DOP). It can be figured out that the two angles θ_p and ϕ_p have the following relationship with the rotation and phase parameter in Jones vectors representation (Equation 2.28):

$$\theta_p = 2\theta \quad \phi_p = \phi \tag{2.42}$$

Both Jones vectors and Stokes vectors are useful tools for studying polarisation optics.

Alignment of the polarisation detection units to the reference states is realised by operations on EPCs to minimise the photon count rate registered on SNSPD 1 and 3. EPCs are controlled by four channels, each driven by -5 V to 5 V voltage. Changing the voltage would cause a change of polarisation on the input of the PBS and influence the SNSPD count rates. Therefore, keeping the SNSPD signals as the feedback, one would be able to control the EPCs accordingly. Co-polarised correlations are therefore registered by SNSPD 1 and 3. On the contrary, SNSPDs 1 and 4 indicates the measurement of cross-polarised cases. When the bases are aligned, the voltages for each channel of the two EPCs are stored respectively in a local PC.

The QD is operated continuously in this work. Therefore, the generation time of entangled photon pairs is randomly distributed. Hence we apply a so-called post-selection method, in which we select events only with matching timing condition for each detector. We manually apply a post-selection time-bin window, 32 ps in this work, larger than the time resolution of detectors to obtain more events within each time-bin window.

The correlation coefficients C_{PQ} in the $|PQ\rangle$ polarisation basis are calculated from the measurement result as:

$$C_{PQ} = \frac{c_{PP} - c_{PQ}}{c_{PP} + c_{PQ}} \tag{2.43}$$

for each time-bin window. In the above equation, c_{PP} and c_{PQ} refer to the measured coincidences for the co-polarised and cross-polarised case.

2.3.3 Influence on entanglement fidelity by bases misalignment and fine structure splitting

In practise, it is difficult to achieve perfect alignment of measurement bases to $|H\rangle|V\rangle$, $|D\rangle|A\rangle$ and $|R\rangle|L\rangle$. We hence add an additional rotation angle θ' and a phase ϕ' as the misalignment to equation 2.22, resulting in:

$$\begin{aligned} \theta'_H &= \theta', \phi'_H = \phi' \\ \theta'_D &= 90^\circ + \theta', \phi'_D = \phi' \\ \theta'_R &= 90^\circ + \phi', \phi'_R = 90^\circ + \phi' \end{aligned} \tag{2.44}$$

Combine the above relation with equation 2.21, we can get the maximum achievable correlation coefficients at zero-delay:

$$\begin{aligned} C_{HV} &= 1 - \sin^2\theta'(1 - \cos(2\phi')) \\ C_{DA} &= 1 - \cos^2\theta'(1 - \cos(2\phi')) \\ C_{RL} &= 1 - \cos^2\theta'(1 + \cos(2\phi')) \end{aligned} \tag{2.45}$$

From the above equation, we could estimate the introduced fidelity drop by a misalignment of detection bases.

For the FSS influences on the entanglement fidelity, we analyse the measured correlation coincidences given by equation 2.21, in which a sinusoidal oscillation with the period given by the FSS and an exponential decay due to the photon lifetime and dephasing is introduced to the correlation coincidences. While the influence of the decay is negligible considering a short detector resolution of 100 ps, for an ideal emitter the oscillation will cause the fidelity to drop to 50% (the classical limit) after a quarter of the rotation period (h/δ).

Hence, we select those QDs with the FSS value that corresponds to the oscillation period equivalent to or greater than four times the detection resolution of SNSPDs. It leads to a maximum affordable splitting parameter of $\delta_{max} = 10\,\mu$eV in this work.

Chapter 3

On-Chip Pumping Device for Network Integration

3.1 On-chip pumping device for InAs quantum dot at the telecom O-band

While Chapter 2 introduces the QD selection based on FSS, an ideal sub-Poissonian entangled photon-pair emitter for an optical quantum network should meet a more strict requirement of suitable operating condition, telecom emission wavelength, high emission rate and coherence time, good single-photon purity as well as small (near-zero) FSS. For telecom wavelength devices, the requirements are yet far from being met. The devices in this work target a device compatible with electrical operation and tuneability within the telecom O-band wavelength range while maintaining good entanglement fidelity.

3.1.1 On-chip pumping device design

A potential solution for achieving electrically driven and tuneable QD devices is to apply an on-chip design for both excitation and tuning. EL QD devices tuned by strain meet this condition. However, their high operational voltage generates a high risk for operating the device, therefore not suitable for deployment in a realistic network. In this work, we explore the alternative method that is the integration of the pumping source with the QD device.

The device structures designed in works [92, 93] allow the electrical operation of the device without bringing negative effects introduced by EL, as is discussed in Chapter 2. Despite this progress, the application of the on-chip pumping (OCP) technology has not yet been demonstrated on a sub-Poissonian entangled photon-pair source. Moreover, the wafer used in this work has a different structure compared to the above works: an additional InGaAs strain-relaxing layer is deposited on top of the QDs which influences the pumping and absorption property in the OCP process.

(a) (b)

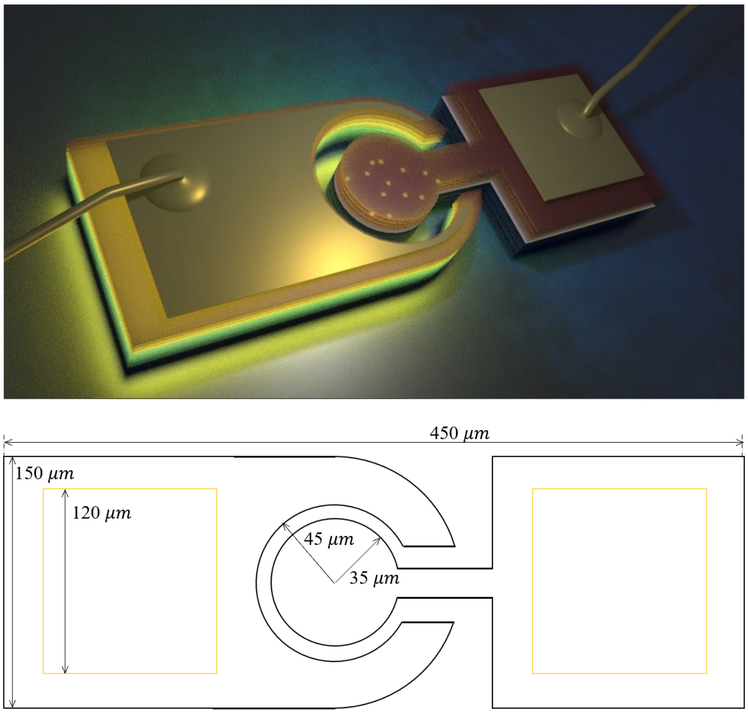

Fig. 3.1 (a) Concept of tuneable electrical entangled QD light source. A current is injected via the top contact on the pumping diode for optical excitation of single quantum dots in the embraced circular tuning diode. Both diodes share the same bottom contact not shown in the figure. (b) Dimensions of the on-chip pumping (OCP) device. The black line indicates the edge of the diode and the yellow line indicates the edge of the ohmic contact.

We have developed a new device inspired by optical excitation using a near-by device as is introduced in [93]. Figure 3.1 shows an artistic image of the design. It consists of two parts: a pumping diode and a tuning diode. The pumping diode is electrically excited by a current injected from the ohmic contact on the left. The emitted light from it in the in-plane direction optically excites the QDs located at the tuning diode. And a bias voltage could be applied from the right ohmic contact for tuning the emission wavelength and QD FSS. Both Ohmic contacts in the figure are attached to the p-type layer of the two devices. Another Ohmic contact is at the n-type layer, not shown in the figure. In comparison with the side-by-side on-chip excitation design in [93], the ring-shaped device allows relatively more light injected into the central region, providing more excitation power to QDs at lower driving currents.

Appropriate device design is of great importance for the performance of any QD devices. Firstly, a short separation between two p-types is preferred to enable sufficient light from the pumping diode to reach the tuning diode. Meanwhile, we would like to have more dots contained in one device for better yielding, meaning a larger area of the tuning diode is preferred. Figure 3.1 (b) shows the dimensions of the OCP devices. The circular region of the tuning diode has a radius of 35 μm, which normally contains from tens of to a few hundred QDs depending on the density. The outside ring of the pumping diode has an inner radius of 45 μm, leaving a 10 μm gap between the pumping and tuning diode. The overall device, including the pumping diode, the tuning diode and bond pads has a width of 150 μm and a length of 450 μm.

3.1.2 Device fabrication

For device fabrication, a standard photolithography method is applied to achieve the required geometry. The area of two devices is defined by etching the surrounding semiconductor material. The photomask is designed based on the device dimension shown in Figure 3.1 (b).

The detailed procedure for device fabrication is shown in Figure 3.2. Steps (1-5) indicate the etching procedures to form the device area. A layer of photoresist is applied on the wafer surface by a spinner for photolithography (1). The photomask is then placed above the wafer. With an ultra-violet (UV) light applied to the wafer followed by development in a dipping bath (2), a window will be formed at the uncovered region of the photomask. It is then followed by a so-called 'wet etching' procedure, during which the wafer is immersed in diluted sulphuric acid (3). It is etched down to the n-type region (4), leaving the unetched diode area as a p-i-n junction with empty space at both p- and n-type region for depositing the ohmic contacts (5). A relatively large window for wet etching is required for the acid fluid to fill in. Wet etching also forms sloped sidewalls instead of vertical, since the acid etches the material to all directions, making the part in contact with sulphide acid for longer time having a larger opening area. When the above factors are considered, the 10 μm gap between the pumping and tuning diode is big enough for etching to be performed successfully. Then we use Acetone to clean the etched device for next steps.

Procedures (6-9) show the process for depositing the ohmic contacts for electric connection. This procedure needs to be separated into the top (p-type) contacts and the bottom (n-type) contacts since they use different materials [108, 109]. Given the uneven surface of the n-type layer after deposition, annealing is required for the bottom contact; therefore, it is deposited first.

The bottom contact made of a NiGeAu alloy is deposited with a thickness of 100 nm. We first use photolithography to open windows on regions for the planned n-type contacts (6-7). Then it is placed under a metal evaporator with different materials loaded and deposited (8). The annealing is performed after this step.

For the top contact, we follow the same procedure. Instead of NiGeAu as material, around 10 nm of Cr and 60 nm of Au is deposited after the photoresist window is opened by photolithography. And it is finished without annealing. The fabrication is finished by removing the remaining photoresist with Acetone (9).

The fabricated chip is packaged after finishing the above fabrication procedure. The deposited ohmic contacts are bonded to a metal pad for external electrical connection using gold wires for electric connection during operation. An image of two fabricated OCP devices is shown in Figure 3.3 (a).

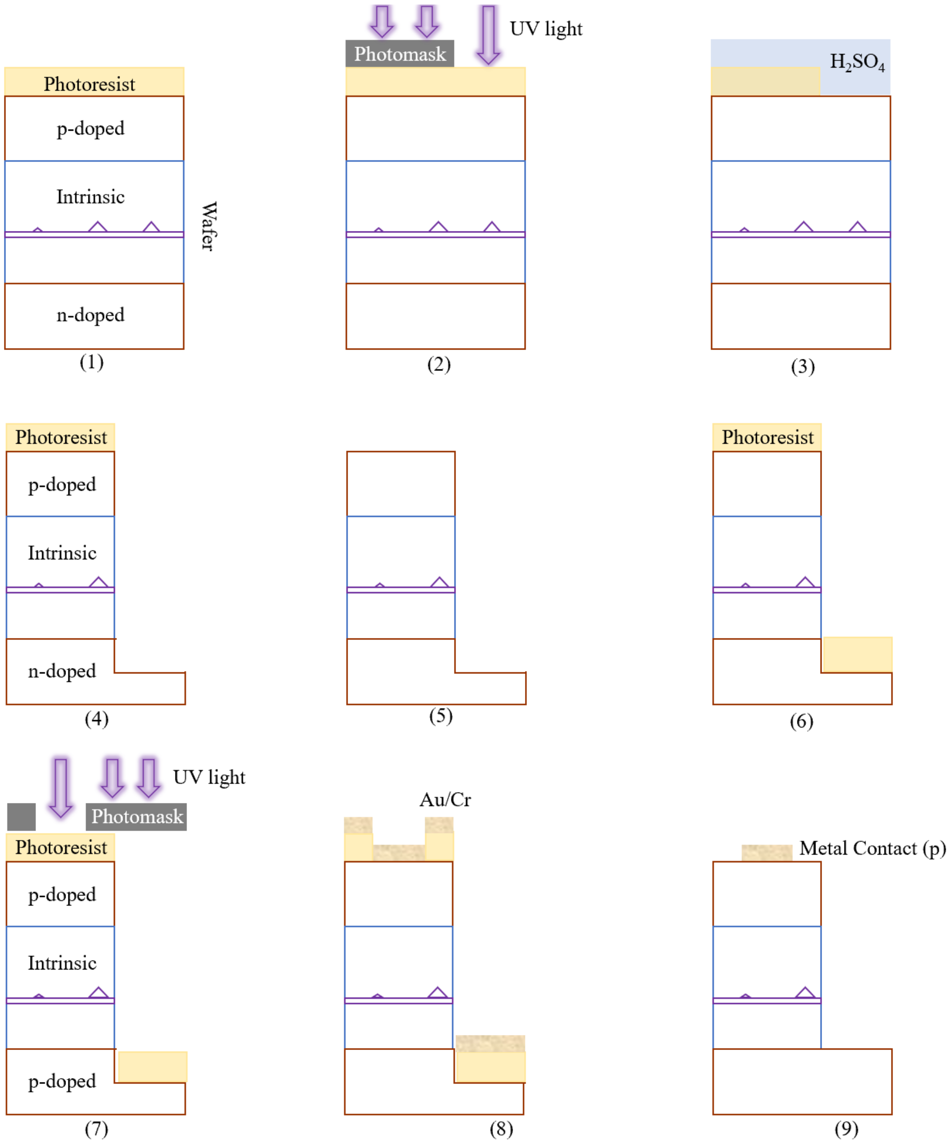

Fig. 3.2 Fabrication of the pumping and tuning diodes and the deposition of the ohmic contacts. The steps of the processing include (1) we use a spinner to deposit a 5 nm flat layer of photoresist on top of the target chip cut from the wafer. (2) The chip is placed on the photolithography machine covered by the photomask, which is designed with its dark field covering the area of pumping and tuning diodes. The lithography light is then applied with the time condition of 9 seconds. (3) The chip is then developed for 45 seconds, leaving an open window. We then use diluted sulphide acid to etch the device until it reaches the N-doped layer. (4) Reaching the n-type layer requires sufficient etching of more than 550 nm. Therefore we etch it for about 50 seconds to realise such an etching depth. (5) We remove the photoresist by Acetone. (6)-(9) is to deposit the ohmic contact for the diodes. In (6) we spin a layer of photoresist again. (7) We put it underneath the designed photomask which has the ohmic contact part as the bright field. And then it is exposed under the lithography beam for 9 seconds. (8) We deposit a layer of metal. (9) The photoresist is removed by Acetone, leaving the ohmic contact on the device as the top contact. The bottom contact is annealed after deposition.

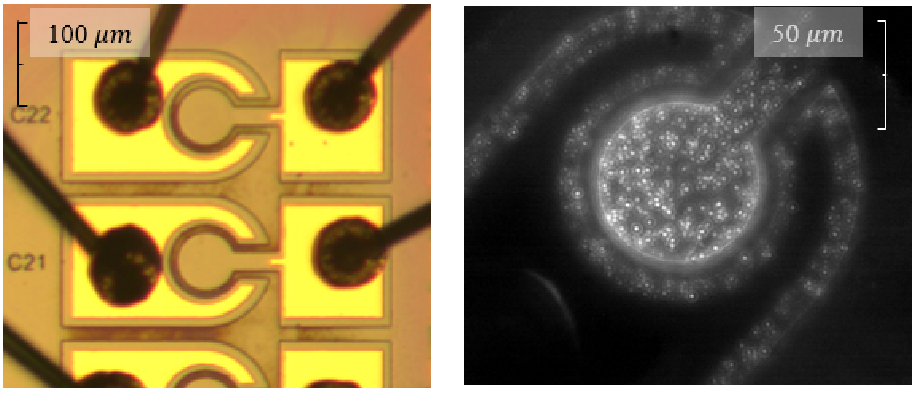

Fig. 3.3 (a) Microscope image of fabricated devices with attached bond wires. (b) Microscope image of QDs in the structure emitting at telecom wavelength when applying a forward bias to the pumping diode. A long-pass filter at 1100 nm is placed before the camera to suppress short-wavelength pumping light for better visibility of QD emission.

The packaged chip is then installed in the cryostat, attached to a cold finger with wires connected to both the pumping diode and tuning diode. A current source is connected to the pumping diode and a voltage source is connected to the tuning diode. Here, a microscope image of it illuminated under the driving condition of 3 mA for the pumping diode and -3 V bias for the tuning diode is taken, recorded using an InGaAs camera which is sensitive at telecom wavelengths. One could notice the glowing individual QDs at the telecom O-band.

3.2 On-chip pumping properties

3.2.1 On-chip pumping efficiency

To explore the influence of the wafer structure on the on-chip pumping excitation, we have investigated the pumping light property. In an ideal case, it is directly measured in the in-plane direction. This is, however, not achievable with a typical micro-PL setup. Thus, we fabricated another chip containing OCP devices with the same design on the wafer used in work [93], and performed a set of pumping diode-QD emission measurements. We here use the name W1310 for the current wafer with 1310 nm QDs, and W950 for the previous wafer with 950 nm QDs for simplicity. The major difference between the wafer of W950 and W1310 is the existence of the InGaAs strain relaxation layer and bigger QDs on W1310. We select one device on each fabricated chip for the comparison; both operated in a pumping condition that is near-saturated, with identifiable X photon spectral line. The applied bias on the tuning diode is -1.5 V for the device on W950, and -2.6 V for the device on W1310. These two voltage values are optimised for X photon emission for both devices.

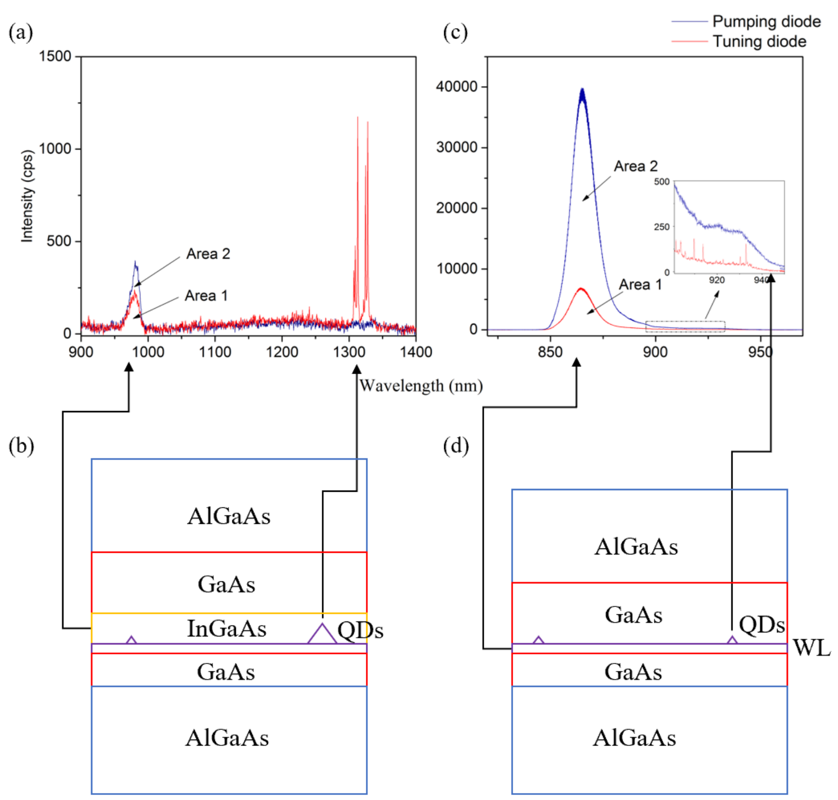

Fig. 3.4 The wafer structure of W950 and W1310 and the corresponding emission spectra of 2 OCP devices. (a) shows the emission spectra of the pumping and tuning diode measured on the OCP device based on W1310. The blue line is the emission from the pumping diode, and the red line is that from the tuning diode. (b) is the corresponding wafer structure of W1310. (c) and (d) are the OCP device emission spectra and wafer structure of W950.

We record the emission spectra from a QD on each device. And they are plotted with the corresponding wafer structure in Figure 3.4, where (a) and (b) are the measured spectra and wafer structure of W1310, and (c) and (d) of W950. The red curves in both figures represent the spectra of the measurement on the pumping diode, and the navy curves represent those measured on QDs in the tuning diode. The pumping light for the measured two wafers is peaked at around 830 nm for W950 and 980 nm for W1310 respectively.

A good evaluation of the pumping efficiency could be made via the ratio between the collected pumping light intensity of the pumping diode and the tuning diode represented by a pseudo efficiency factor η:

$$\eta = I_1/I_2 \tag{3.1}$$

where I_1 is the emission intensity from the tuning diode of the pumping light band, and I_2 is the emission intensity from the pumping diode of the same band. It corresponds to the integrated intensity of area 1 and area 2 in Figure 3.4 (a) and (c). Given that the tuning diode is only excited by the light emitted from the pumping diode and the two diodes share the exact wafer structure, such an efficiency factor indicates the ratio of pumping light reaching the tuning diode.

The two measurements observe significant differences in pumping efficiency and background. We obtain $\eta_1 = 1/2$ for W1310, and $\eta_2 = 1/6$ for W950. The current applied on the pumping diode of W950 to achieve saturation was 15 mA in comparison with 1.6 mA on W1310 via a comparison between the on-chip excitation and PL spectra. The separation of the pumping light from the QD emission is more than 300 nm on W1310 compared with around 100 nm on W950. The large separation further guarantees small leakage from the pumping light to the telecom O-band. In comparison, a strong background was observed on the emission of the QD on W950.

A pumping-favoured environment could explain the improvement mentioned above in the on-chip excitation efficiency of W1310. Firstly the DBR cavity mode, which aims to enhance the vertical emission from QDs at the telecom O-band, suppresses the vertical emission of the light at the wavelength outside of the cavity resonance window. Therefore, the in-plane transmission is preferred. Another contribution is from the InGaAs cap layer. In W1310 spectra, photons from the pumping light at around 980 nm have the energy just above the InGaAs bandgap (corresponding to 1030 nm emission wavelength at 4 K) and below GaAs (820 nm). It means that the pumping light is emitted from the QW consisting of the InGaAs and InAs WL. As is illustrated in Figure 1.4, the pumping and absorption area on W1310 has a thickness greater than 5 nm. In comparison with the WL on W950 of only 0.5 nm, it significantly increases the absorption area given that the effective pumping light emits in the in-plane direction.

3.2.2 Location influence on the on-chip pumping emission spectra

During the device fabrication, we have experienced the non-uniform characteristics of the wafer structure and the QD distribution. The QD density increases from the centre to the edge of the wafer. This variation may come from the growth with a temperature gradient over the wafer. This may as well influence the OCP process. We therefore fabricated several devices over different locations on the same wafer and recorded their spectra for investigation.

Although on-chip excitation under appropriate driving condition (<5 mA) and QD emission are achieved on all the devices, a spectral difference is noticed. Figure 3.5 shows a spectra comparison for fabricated OCP devices at different locations. Among the three devices (a) is closest to the wafer centre, with lowest dot density; while (c) is closest to the edge with the highest density. A clear difference in the OCP efficiency could be noticed by comparing their η factors. The efficiency decreases from the device in (a) to (c). The stronger GaAs emission at around 820 nm from devices (b) and (c) also indicates the largely over-saturated EL on the pumping diode. It means that a higher power is required for the devices toward the edge of the wafer to excite the QDs located in the tuning diode based on the same design.

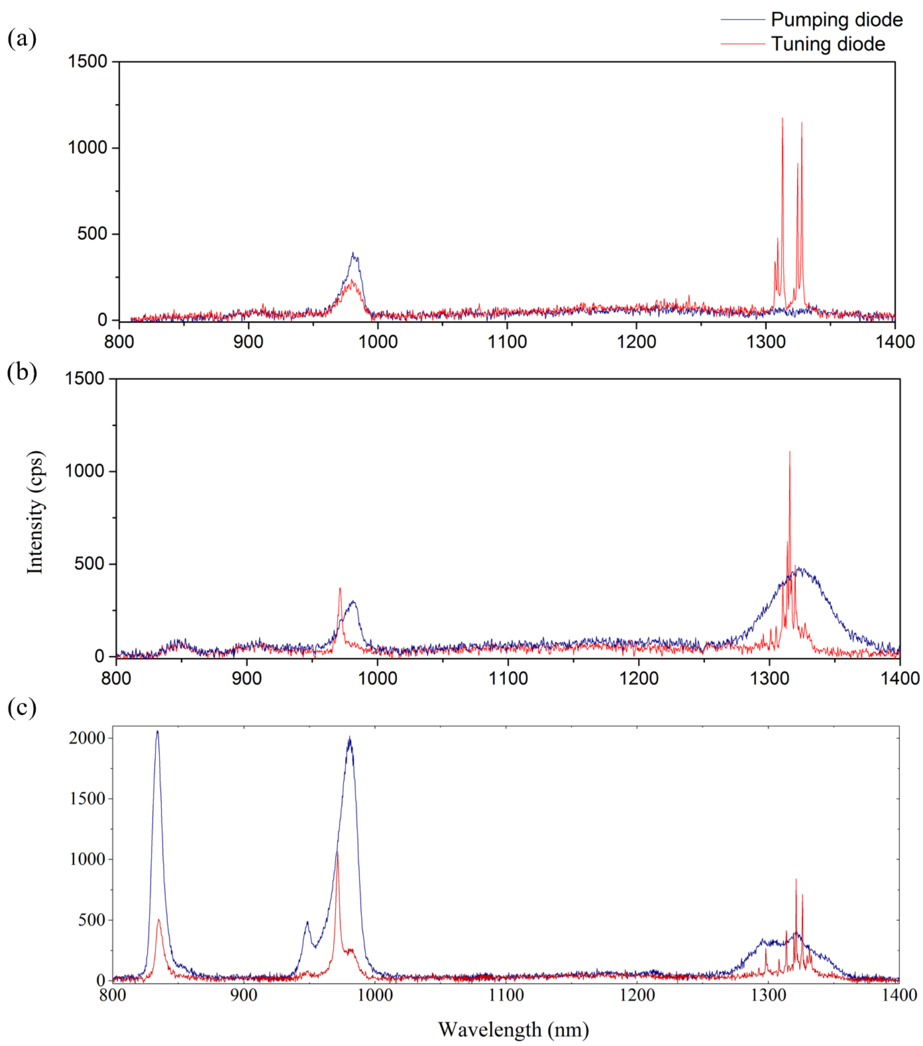

Fig. 3.5 Emission spectra of 3 OCP devices. The lines in blue represents the emission spectra collected from pumping diodes, the lines in red represents the light collected from QDs. From (a) to (c), the region gets closer to the edge of the wafer with higer density of QDs.

The efficiency variation may come from the difference of the wafer structure; however, we have not yet carried out a detailed study on it. Moreover, one could notice that the emission spectra of the pumping (InGaAs) layer are different in these three devices. In (b), InGaAs emission shows a different feature for pumping and tuning diodes. It might be due to the higher dot density towards the edge that results in more recombination of carriers. Therefore more pump light is required to get the individual dots bright.

3.3 Characteristics of the quantum dot emission

In this section, we discuss the photon statistics and entanglement properties of the OCP device. Typically one OCP device contains 100-200 QDs in its tuning diode. We have inspected one of the devices with roughly 120 QDs primarily based on their FSS. Owing to the random nature of the self-assembled QDs used here, photons emitted at telecom wavelength generally exhibit a broad variation of parameters, requiring the selection of an emitter with suitable properties. For the device displayed, there is one QD (dot17) meeting the requirements for brightness and entanglement fidelity. The following characterisations have been carried out on this QD.

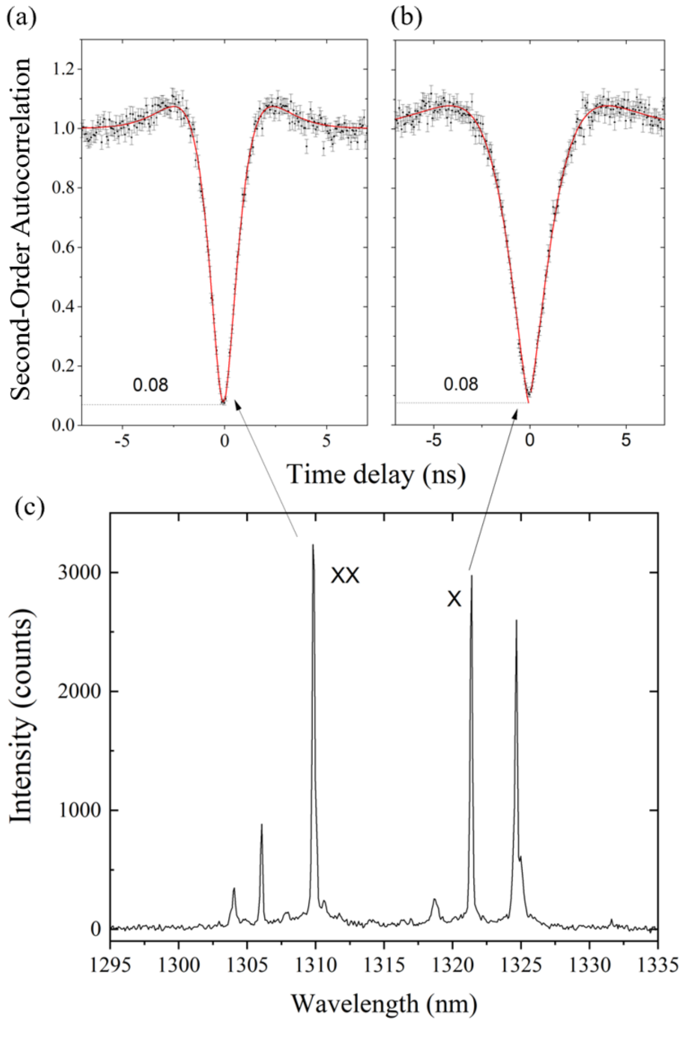

Fig. 3.6 Dot 17 emission spectrum and second-order correlation function. (a) Spectrum of quantum dot for -2.6 V bias voltage applied to the tuning diode. The exposure time was 2 s. Measurement of second-order correlation function for (b) XX and (c) X photons including numerical fit. Displayed error bars are propagated from Poissonian counting statistics.

3.3.1 Emission spectrum and single-photon purity

Dot17 is driven by a fixed pumping current of 1.6 mA and a bias voltage of -2.6 V for tuning the XX photon to the centre of the telecom O-band (1310 nm). The count rate of XX and X are respectively 500 kHz and 400 kHz, each directly measured by a detector (SNSPD, with a jitter of 70 ps and detection efficiency of around 65%).

Figure 3.6 (a) and (b) shows the second-order auto correlation measurement on the XX and X photons, and (c) is the corresponding emission spectrum of the dot 17. By fitting a four level $g^{(2)}$ curve on the measured result, we obtained $g^{(2)}_{XX}(0) = 0.08$ and $g^{(2)}_{XX}(0) = 0.08$. The background calculated from those two measurements using equation 2.16 are respectively 4.2% and 4.4%.

Compared with the optically excited QDs in Chapter 2, the XX/X photon count rate stays at a similar level. And the background level has dropped by around 2.2% for X photons. Such a difference might be from the difference of the QD or from the in-plane excitation. But overall, it illustrates that the OCP process results in a similar level of single-photon purity of the emitted photons from a QD as when excited using a laser.

The second-order autocorrelation measurement is only shown when the pumping diode and tuning diode is driven in continuous-wave (CW) mode. We have applied 100 MHz pulsed operation on the device (pumping diode). However, the obtained photon rate is too low to show any clear second-order autocorrelation properties.

3.3.2 Wavelength tuneability

The wavelength tuneability is studied by recording the QD emission spectra at the telecom O-band while changing the tuning applied bias of the OCP device. We keep the current at 1.6 mA and tuned the voltage from 0 to -3.8 V with a step size of 0.1 V. Figure 3.7 shows the wavelength tuning range of dot 17. More than 30 nm and 25 nm are achieved respectively on XX and X photons. The electric field E in the plot is calculated by the relation $E = (V - V_0)/d$. The internal electric field V_0 is estimated as the built-in potential of the AlGaAs barrier taken to be 2.2 V, and the width of the intrinsic region d is 203 nm.

The wavelength tuneability in several relevant works is summarised on QD in table 3.1. Here, the comparison of the wavelength (or energy) tuning range to the maximum introduced electric field could be used for estimating the tuneability. The QDs in [89, 90, 110] emit photons at short wavelengths (around 900 nm), self-assembled InAs/InGaAs QDs grown surrounded by GaAs, forming one QW. In particular, the InGaAs QD in [110] has additional layers for strain tuning underneath the QW. [111] shows an InAs QD embedded in InP substrate, emitting at around the telecom O-band. Unfortunately, only the voltage is provided in works [90, 111] without information regarding the electric field. In comparison with the above works that have one QW surrounding the QD, the wafer in this work (also in work [54]) with a dual-QW shows a higher tuning range when applying a similar range of electric fields.

Various factors contribute to the tuneability of QDs, including the III-V semiconductor material and wafer structure. QDs have highly confined excited quantum states, and thus their emission wavelengths are limited within a narrow range. Hence loosening the confinement would help the QDs gain wavelength tuneability within a certain range. Reviewing the structure of this wafer, the QDs are located in a dual-QW structure. The first QW is formed by GaAs surrounded by AlGaAs barriers, and the second QW is formed by InGaAs surrounded by GaAs barriers. Compared with QDs in a wafer without a cap layer (InGaAs in this case) where the GaAs-AlGaAs QW is mainly used for preventing the carriers from tunnelling out, the second QW further loosens the confinement of the excited states of QDs. As a result, a change of the electric field across the electron-hole pair in a QD results in a greater energy shift of the wave function.

3.3.3 Fine structure splitting tuneability

In comparison, the strain-tuned devices are operated under a much smaller electric field. However, due to significantly larger distances between the metal contacts, the applied voltages are often around several hundreds of volts. For magnetic field-tuned devices, a 9 T field is even less practical for network integration of a proper emitter.

As introduced previously, FSS in self-assembled QDs is caused by the geometric imperfection during the growth. The time-dependent oscillation originated from the FSS reduces the entanglement fidelity. Similarly, the FSS could be tuned by applying an electric field, magnetic field or strain. Thus, it is therefore important for the QD to stay entangled, while the change of the applied bias tunes the emission wavelength. As is introduced in Chapter 2, a FSS less than 10 μeV is required.

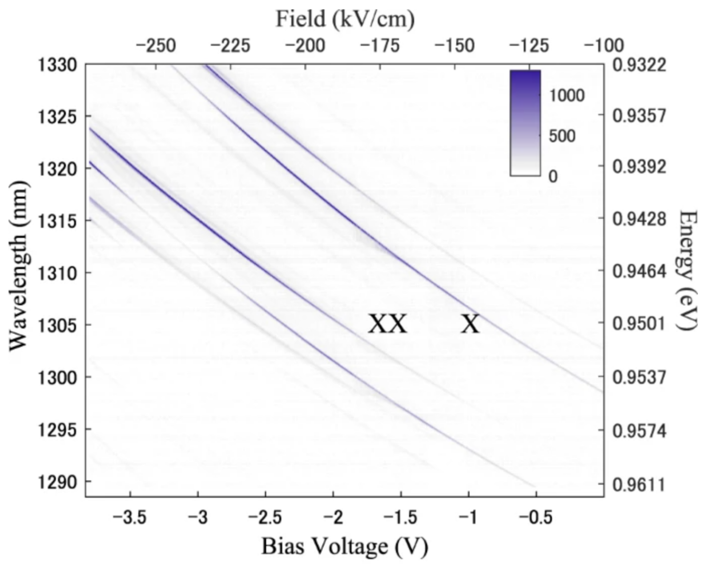

Fig. 3.7 Wavelength tuning of XX and X photons of the dot used in this work. Both can be tuned over 25 nm.

Although the FSS measurement method introduced in Section 2.4 is an effective method for inspecting a large amount of QDs, it requires two numerical fits that potentially reduces the accuracy. We here use an alternative approach for a better precision. FSS is the value of the splitting energy level of QD exciton states, hence directly reflected on the polarisation correlation of the generated entangled photon pairs. Reviewing the co-polarised coincidences:

$$p_{co} \;=\; |\langle\, P'_X \mid H' \,\rangle|^2 = (1 \;-\; 2\,\sin^2\frac{\theta}{2}\;\cos^2\frac{\theta}{2}\;(1 \;-\; \cos(\;\frac{\delta}{\hbar}t \;-\; 2\varphi))) \tag{3.2}$$

The time-dependent oscillating factor $\cos(\;\frac{\delta}{\hbar}t \;-\; 2\varphi)$ is influenced by FSS δ. Thus, by fitting the measurement curve with the above equation, the FSS value can be obtained.

Figure 3.8 (a) shows a measured polarisation correlation on the dot 17 at a random superposition basis and the fitted curve of such a measurement by equation 3.2. In this measurement, the X photon is used as a synchronisation signal; therefore the time-axis is reversed.

A bias-dependent FSS measurement has been carried out using the above method. The result is shown in Figure 3.8. As an electric field is applied all transitions Stark shift with the applied field, following the form [89]:

$$E = E_0 - pF + \beta F^2 \tag{3.3}$$

where p is the permanent dipole moment in the z-direction, and β is the polarizability and F is the applied field. Here we notice that within the wavelength tuning range, the FSS stays below the threshold of 10 μeV.

Reference	Method	Central wavelength	Tuning range	Maximum field
[90]	Electrical field	900 nm	1 nm	(0.6 V)
[110]	Electrical field	893 nm	4 nm	80 kV/cm
[89]	Electrical field	941 nm	18 nm	450 kV/cm
[111]	Electrical field	1355 nm	7 nm	(26 V)
[54] (same wafer)	Electrical field	1280 nm	50 nm	400 kV/cm
This work	Electrical field	1310 nm	30 nm	150 kV/cm
[71]	Strain	1254 nm	2 nm	(400 V)
[85]	Strain	949.8 nm	2 nm	25 kV/cm
[86]	Strain	886.2 nm	3 nm	30 kV/cm
[60]	Strain	888 nm	1.6 nm	25 kV/cm
[110]	Strain	888 nm	0.7 nm	16 kV/cm
[87]	Magnetic field	973.5 nm	0.8 nm	9 T

Table 3.1 Summary of the wavelength tuneability from various works on tuneable QD emitters.

3.3.4 Photoluminescence and electroluminescence spectra comparison

We compared the emission of this dot when excited by the pumping diode with when excited using PL with an external laser, as is shown in Figure 3.9. The laser diode has an emission wavelength of 850 nm. Both spectra were acquired with the spectrometer integration time set to two seconds. In order to acquire the same X photon emission intensity, we need to tune the excitation power to be over-saturated for the PL process, indicated by double the emission rate on XX photons. Given that 850 nm is closer to the GaAs bandgap at 4 K (1.52 eV, corresponding to around 820 nm), the PL spectra shows more features of the above-band excitation such as higher background around the XX and X emission line due to the introduced perturbation.

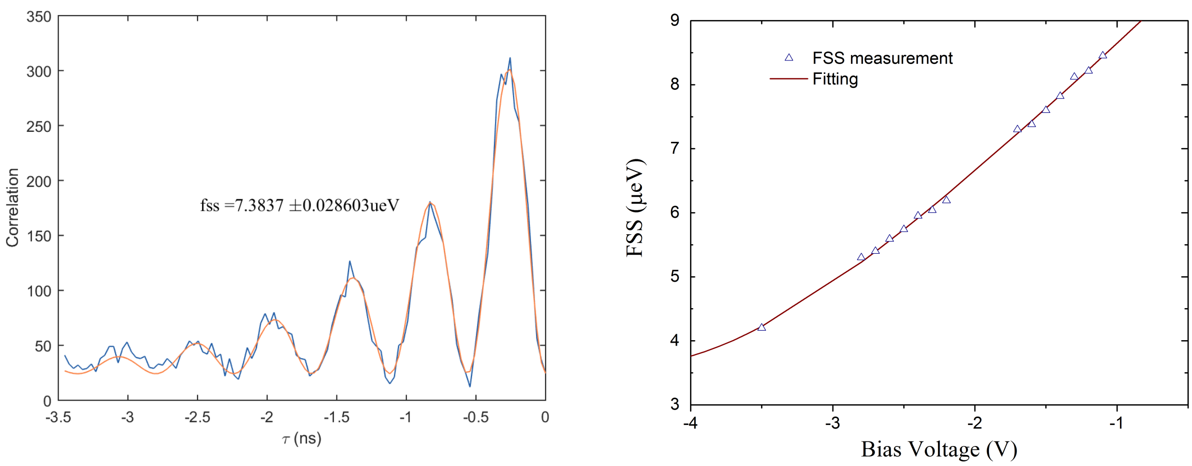

Fig. 3.8 The FSS is obtained by a fitting of the oscillation when recording X-XX correlations in a superposition basis. (a) shows one of the measurement result. (b) shows a change of the FSS for the dot used in this work with respected to the applied voltage bias.

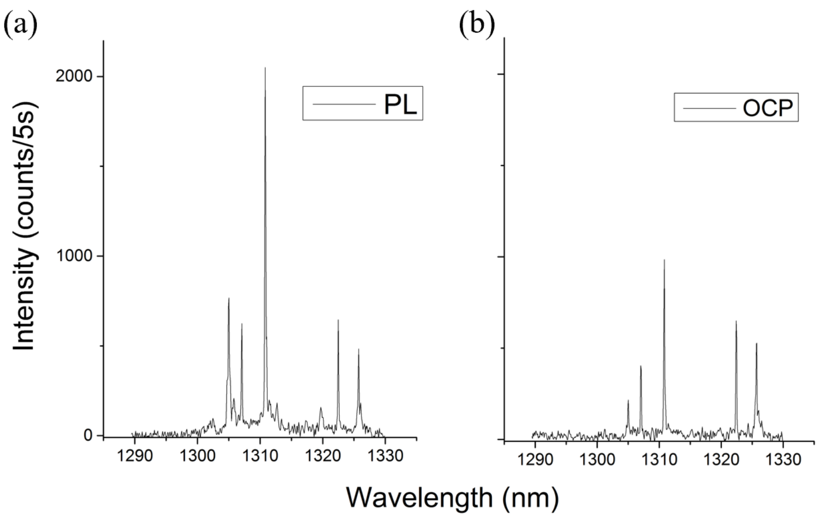

Fig. 3.9 Comparison of PL and OCP spectra on dot 17. PL is performed with a laser at 850 nm. And the QD emission spectrum under this process is shown in (a). The QD emission spectrum from the OCP process is shown in (b).

Two reasons are contributing to this difference. Firstly, the laser wavelength for PL scheme is closer to the GaAs bandgap. Therefore, a relatively larger proportion of the pumping light generates carriers at the GaAs instead of the InGaAs QW. Secondly, the OCP pumping light is resonant with the absorption area of the tuning diode, generating carriers in the QW more easily. Overall speaking, the OCP process generates a cleaner spectrum than PL at shorter wavelengths, making it a favourable excitation scheme for the QDs with this wafer structure.

3.3.5 Entanglement fidelity

An entanglement measurement is carried out using the setup illustrated in Figure 2.8 on the selected QD from the OCP device. Figure 3.10 shows an in-lab measurement result of the correlation contrast of three bases and the calculated entanglement fidelity. The data is recorded for 30 min for each basis and a post-selection window of 32 ps closest to the zero-delay of the XX and X correlation is applied. For this QD, we obtain around $97.32 \pm 1.2\%$ maximum fidelity. This illustrates that OCP devices have the potential to provide high-fidelity entangled qubits comparable to QD entangled photon-pair sources under PL excitation. The electrical operation further guarantees its network integration capability.

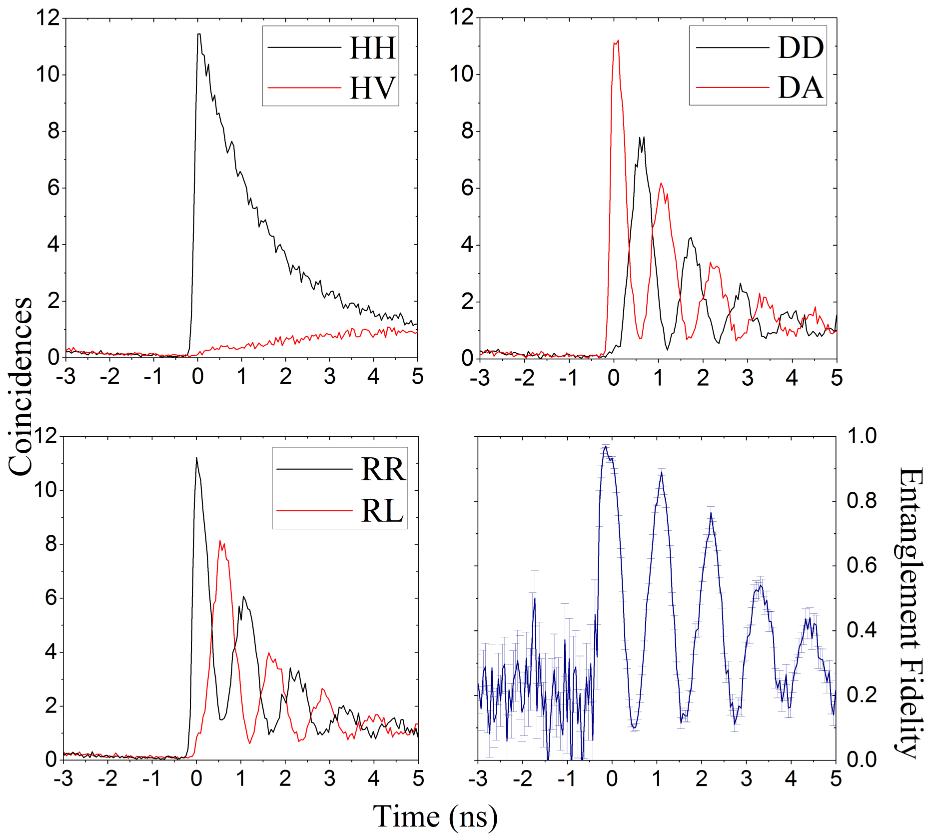

Fig. 3.10 Polarisation correlation measurement result of the entangled photon pairs emitted from dot 17 in the OCP device. (a), (b) and (c) respectively represent the normalised correlation measurement result on $|HV\rangle$, $|DA\rangle$ and $|RL\rangle$ bases. (d) represents the evaluated entanglement fidelity.

Chapter 4

Entangled Photon Transmission over an Installed Loop-back Fibre

4.1 Fibre birefringence

Currently, two main encoding schemes for quantum states have been adopted, both in their polarisation [35, 101] and time-bins [112, 113]. These two encoding methods would likely coexist in a real quantum network. We here focus on the transmission of polarisation-encoded qubits, which are naturally favoured for qubit generation in sources based on sub-Poissonian quantum emitters [50, 67, 114, 115] due to the ability of directly interfacing with electronic states on optical dipole transitions. The stability during qubit transmission, however, is undermined by random birefringence variation in optical fibre generated by varying environmental conditions. In particular, the installed single-mode fibre, which is used in this work, has introduced fibre birefringence by the internal or external stress [116] that generates the polarisation states variation during transmission. Our target is to develop a system that compensates for such variation.

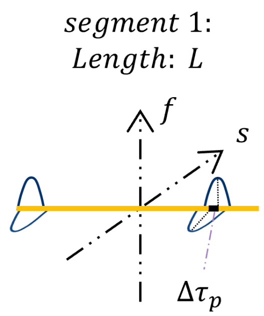

Fig. 4.1 Phase delay introduced by fibre birefringence. When the input light propagates through the first segment of the optical fibre, the birefringence would generate a phase delay $\Delta\tau_p$ between the projected components along the fast (f) and slow (s) axes.

Optical fibre imperfections, as well as the introduced perturbation, create a polarisation-dependent change of the refractive indices. We represent such a change based on two distinct polarisation eigenstates: normally referred to as 'fast' and 'slow'. To understand the polarisation states variation caused by fibre birefringence, we normally resolve the state into components along the fast and slow eigenstates. However, the fibre birefringence is more complicated in real cases, considering the optical fibre is normally bent and exposed to forces in different directions. Hence, we first consider a short optical fibre segment of length L, along which the birefringence is fixed, as is shown in Figure 4.1. The propagation constant along the two eigenstates are different, represented by β_f and β_s. We review the phase velocity:

$$v_p = \frac{\omega}{\beta} \tag{4.1}$$

where ω is the light frequency. The two polarisation components along the eigenstates would have a phase delay $\Delta\tau_p$:

$$\Delta\tau_p = \frac{L}{v_{ps}} - \frac{L}{v_{pf}} = \frac{\beta_s - \beta_f}{\omega} L = \frac{\Delta\beta}{\omega} L \tag{4.2}$$

The current polarisation state with the introduced phase delay would now propagate along another short segment of the optical fibre with the orientation of the eigenstates along a different direction from the first segment. For an installed fibre meandering along various geographically different locations with varying temperature and external stress, the birefringence direction could have a great variation, making the calculation highly complex. Hence, to simplify the analysis, we represent such a transformation based on the Poincaré sphere, as is shown in Figure 4.2. The fibre birefringence could be denoted by an axis, along which the polarisation states rotate for $\frac{\Delta\beta}{\omega}L$ where L is the fibre length.

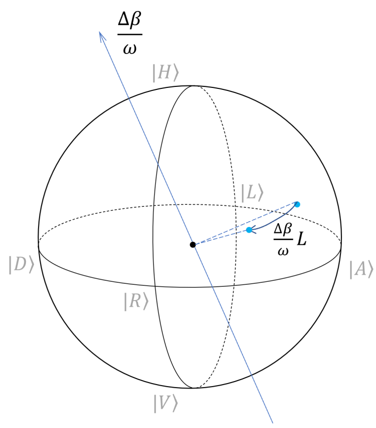

Fig. 4.2 An illustration of a fixed fibre birefringence influencing the polarisation states variation. The fibre birefringence $\frac{\Delta\beta}{\omega}$ is frequency-dependent, with its direction shown with a blue axis on the Poincaré sphere. The polarisation states variation caused by such a fibre birefringence corresponds to a states rotation along the birefringence axis with the value $\frac{\Delta\beta}{\omega}L$ where L is the length of the fibre.

An installed fibre would have segments with different birefringence axis, and this results in the random polarisation states variation over a long installed fibre. Therefore, it could be compensated by unitary transformations applied by polarisation controlling components.

We notice that the polarisation states variation over an installed optical fibre is influenced by the birefringence direction, fibre length and light frequency. In realistic cases, when light with different wavelengths propagates over the same fibre, the polarisation states variations are randomised for each wavelength. Such a phenomenon will be discussed in Section 3.5.

4.2 Polarisation stabilisation method

We design the polarisation stabilisation system based on the analysis in the previous section. Polarisation controlling units need to be introduced and installed. Components such as EPC, HWP, QWP and fibre-wave plate (FWP) are the effective equipment to generate compensation operations against birefringence-introduced polarisation states variation when feedback signals are provided. For polarisation entangled photon pairs, arbitrary polarisation states need to be stabilised for entangled qubit transmission. In this scenario, two references with non-orthogonal polarisation states are required to be able to lock any arbitrary polarisation drift effectively.

We use $|S_a\rangle$ and $|S_b\rangle$ to represent the two non-orthogonal references, and a unitary transformation U_f to represent a random rotation of polarisation states caused by fibre birefringence. Such a transformation acts on both of the two non-orthogonal polarisation states. We apply two compensation operation, represented by R_a and R_b respectively. The transformation has to meet the following conditions [117]:

$$\begin{aligned} R_a U_f \left|S_a\right\rangle &= \left|S_a\right\rangle \\ R_b \left|S_a\right\rangle &= \left|S_a\right\rangle \\ R_b R_a U_f \left|S_b\right\rangle &= \left|S_b\right\rangle \end{aligned} \tag{4.3}$$

in which R_a and R_b compensate respectively for the states variation applied on $|S_a\rangle$ and $|S_b\rangle$. From the above equation, $R_b R_a = {U_f}^{-1}$ leads to the full compensation of arbitrary changes in birefringence. Operational cross-talk is avoided if the transformation by R_b does not change the states of $|S_a\rangle$.

The compensation could be physically represented on a Poincaré sphere as movements and rotations, as is shown in Figure 4.3. Three states are shown on this sphere: $|S\rangle$, which represents an arbitrary random input to be stabilised. $|S_a\rangle$ and $|S_b\rangle$, which are two reference states injected simultaneously with $|S\rangle$. These two references are originally aligned to two known detectable states with orthogonal directions on the sphere, for example $|H\rangle$ and $|A\rangle$. When fibre birefringence variation occurs, all states undergo the operation by U_f and reach their transformed states $|S\rangle'$, $|S_a\rangle'$ and $|S_b\rangle'$.

The stabilisation mechanism here reacts to the polarisation state changes. We operate the first polarisation controlling component to apply a unitary transformation R_a on the first reference, bringing it to its original state $|S_a\rangle$. The proper operation could be realised based on a feedback signal by the detection of the first reference which monitors the projection of the state along the axis of $|D\rangle\,|A\rangle$. Meanwhile, this operation transform $|S_b\rangle'$ to a state $|S_b\rangle''$. It is a state on the equator along $|D\rangle\,|A\rangle$ axis. Therefore, an additional operation R_b on the second reference on the equatorial direction along the axis $|D\rangle\,|A\rangle$ would successfully recover it to the original states $|S_b\rangle$ without generating disturbance to the recovered $|S_a\rangle$. Given that the states along two axes

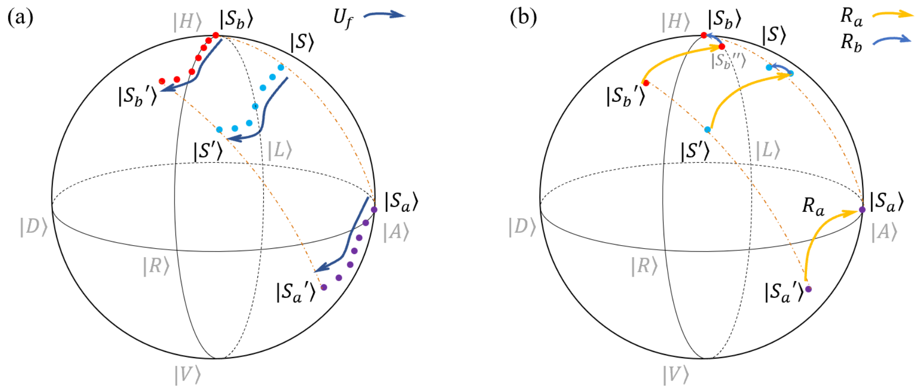

Fig. 4.3 (a) A physical representation of the polarisation states variation caused by fibre birefringence on the Poincaré sphere. $|S\rangle$, $|S_a\rangle$ and $|S_b\rangle$ are the three input states, in which $|S_a\rangle$ and $|S_b\rangle$ have polarisation $|A\rangle$ and $|H\rangle$ respectively. $|S\rangle'$, $|S_a\rangle'$ and $|S_b\rangle'$ are the three transformed states by an unitary operation U_f caused by the fibre birefringence. (b) A physical representation of the polarisation stabilisation mechanism. R_a and R_b are the two operations applied by polarisation controlling components on the three states. The first operation is R_a, which brings the transformed state $|S_a\rangle'$ to $|S_a\rangle$, and $|S_b\rangle'$ to $|S_b\rangle''$. Then the second operation R_b brings $|S_b\rangle''$ to $|S_b\rangle$.

are fixed, the polarisation state variation is compensated over the whole Poincaré sphere and the input light $|S\rangle$ is recovered to its original state.

4.3 Stabilisation system architecture

4.3.1 System design

When designing the system, the following points need to be considered:

1. Reliable feedback signal.
2. Effective implementation of recovery transformation R_a and R_b.
3. Little influence on qubit rate and background.

We designed a stabilisation system that is operated based on feedback given by polarisation references [61, 118]. Figure 4.4 shows its schematic. References are generated using a wavelength-tuneable laser operated at telecom O-band. It is tuned to emit the same wavelength as the transmitted photons.

As is introduced in the previous section, two non-orthogonal references need to be stabilised in order to compensate for arbitrary polarisation changes. We place a LP just after the laser to make the emitted light polarised, and a BS to split the emission light of the laser into two paths. An EPC is installed in one of the two split paths for alignment. By operating the optical switch (OSW1), we connect one of the references to the system.

To detect the polarisation states after propagating along the birefringent fibre, we apply a similar setup as the correlation measurement setup. Two power meters (PMs) instead of SNSPDs are installed after PBS, which detect polarisation projection values of the input light based on the measured power. Two EPCs (EPC 3 and 4) are installed on separated fibres for calibrating the polarisation measurement bases before the PBS. And two OSWs are operated to select one of the EPCs to be connected to the system. We introduce a polarisation projection value, represented by the following equation:

$$pol = \frac{P_1 - P_2}{P_1 + P_2} \tag{4.4}$$

in which P_1 and P_2 stands for the measured power value given by PM1 and PM2. In an ideal case, when the input matches one of the state (denoted by $|H\rangle$) selected by the PBS, the corresponding PM will have a maximum measured power value ($P_{1_{max}}$) and the other PM will measure ($P_2 = 0$). Therefore in this case, the power value has a maximum of $pol_{max} = 1$. When the input state is at the orthogonal state $|V\rangle$, it reaches the minimum $pol_{max} = -1$. Represented on the Poincaré sphere, *pol* is a polarisation projected value of any polarisation states along the $|H\rangle$ $|V\rangle$ axis. We could estimate the angular deviation θ to an arbitrary direction from the $|H\rangle$ state using the following equation:

$$\theta = 2 \times \arccos(pol) \tag{4.5}$$

The detection modules are aligned to the same axes as the generated references. It means that the initial input will be at one end of the detection axis that has a reference value of $pol \approx 1$.

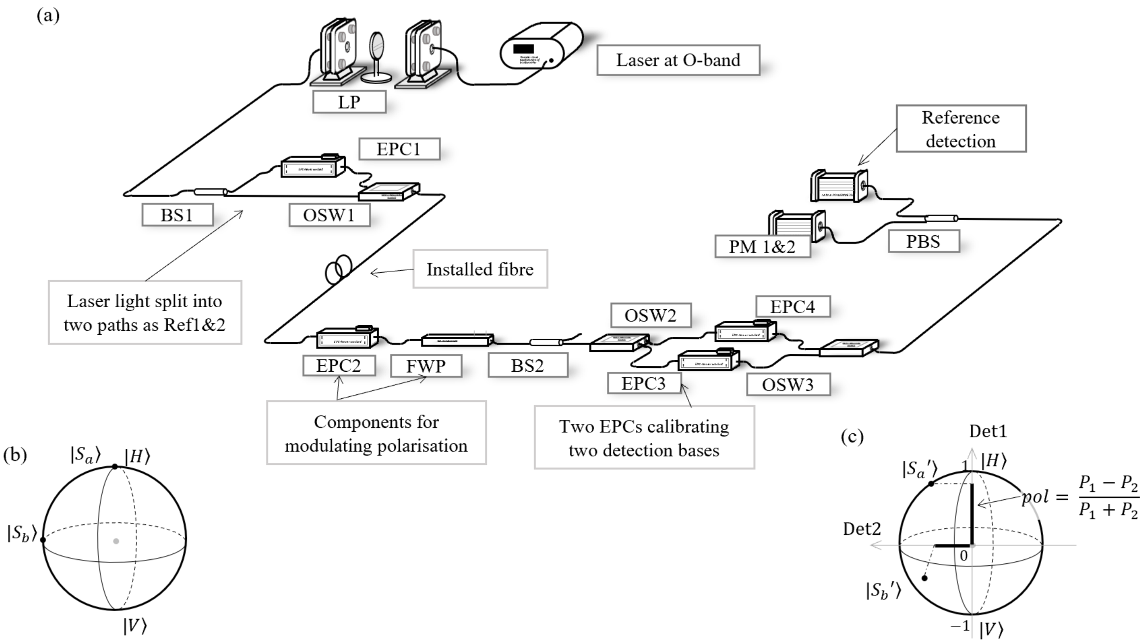

Fig. 4.4 (a) An illustration of the polarisation stabilisation system. The input polarisation references are generated by a tuneable laser emitting at the telecom O-band, passing a LP and split by BS1. EPC1 is for tuning the polarisation state of one of the references. An optical switch (OSW1) selects which reference is injected to the installed fibre. EPC2 and FWP are the components generating the polarisation compensation operation. BS2 is a 90:10 BS to monitor the polarisation state during the alignment. And its 10% output port is connected to a Polarimeter that is not shown here. The two detection bases are monitored by EPC3 and EPC4, switched into the system by OSW2 and 3. The states are detected by a system consisting of the two EPCs, a PBS and two power meters. (b) two references with states $|S_a\rangle$ and $|S_b\rangle$ are tuned to have the states $|H\rangle$ and $|D\rangle$. (c) Detection bases are aligned to $|H\rangle$ and $|D\rangle$. The polarisation projection values *pol* are measured by this setup.

When operating the polarisation stabilisation system, the system would maximise the *pol* value, keeping it at its original location on the Poincaré sphere.

We align the two references to have orthogonal directions on the Poincaré sphere, for example, the states $|H\rangle$ and $|D\rangle$ as is shown in Figure 4.4 (b). This configuration maximises the detection sensitivity for polarisation change in any directions. The detection bases are aligned to $|H\rangle$ and $|D\rangle$, corresponding to the two input states, as is shown in Figure 4.4 (c). Hence, the states variation would be represented by the drop of *pol* at each detection base.

EPC2 and the FWP connected before the detection setup respectively apply stabilisation operations R_a and R_b. Importantly, operations on the FWP need to meet the requirement of R_b, which is the second condition in equation 4.3, to not change the polarisation state of $|S_a\rangle$.

The FWP used in this work is a length-tuneable birefringent fibre. It has introduced static stress similar to a polarisation-maintaining fibre (PMF), resulting in its orthogonal fast and slow optical axes. Reviewing the introduced phase delay during lightwave propagation in an optical medium with birefringence in equation 4.2, we notice that when the FWP length changes, the

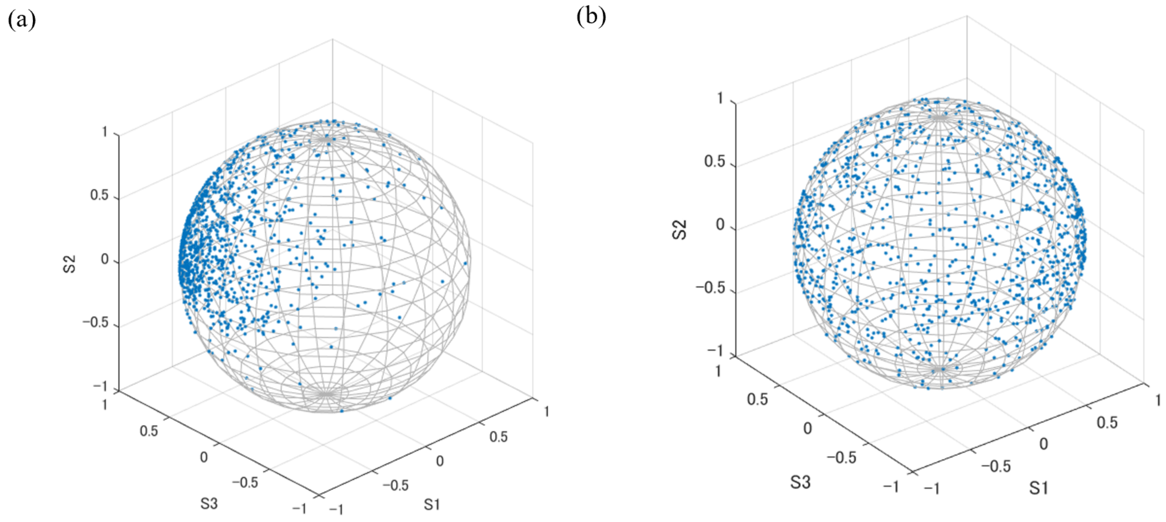

Fig. 4.5 Performance comparison of two EPCs. Both EPCs are injected with a given input polarisation state, and output to a polarimeter which is operated with a 30Hz recording rate. Both EPCs are running in scrambling mode with 3 Hz, 7 Hz, 11 Hz and 19 Hz for four channels. (a) shows the output polarisation states from a malfunctioned EPC. The output polarisation state is highly restricted within one region occupying a quarter-sphere. One could compare it to a normally operated EPC shown in figure (b) where the polarisation is perfectly randomised.

introduced phase difference varies accordingly, resulting in a polarisation states rotation around an optical axis on the Poincaré sphere, with the two endpoints on the axis corresponding to the fast and slow optical axis of the FWP. This is the operational principle of the FWP. In such a case that the input light is aligned to one of the endpoint states on the rotation axis, the state will remain unchanged during the operation of FWP. Hence, we align the rotation axis to the state $|S_a\rangle$. Such a property of the FWP cannot be achieved straightforwardly by a normal EPC which controls polarisation by applying forces to the optical fibre.

During tests, we have discovered a malfunction occurring in most of the EPCs. The EPC has four channels applying forces onto the embedded fibre from four directions to change the output polarisation. Each channel is operated by a voltage in the range from -5 V to 5 V. However, during tests, we have found that most of the EPCs (OZ optics) had performance problems for polarisation control, hence failing to generate the appropriate transformation R_a. For specific input polarisation states, the EPC transforms to output states only within a restricted region on the Poincaré sphere. We have recorded such malfunctioning when running the EPC with four channels having different prime-number modulation frequencies. From the result shown in Figure 4.5, with a fixed input polarisation state, the biased-EPC gives output polarisation states restricted within a quadrant in (a) compared with a whole-sphere coverage in (b) generated from a normally functioning EPC. As a result, when performing the actual experiments, we carefully inspected each EPC to ensure they function normally.

4.3.2 Stabilisation system alignment

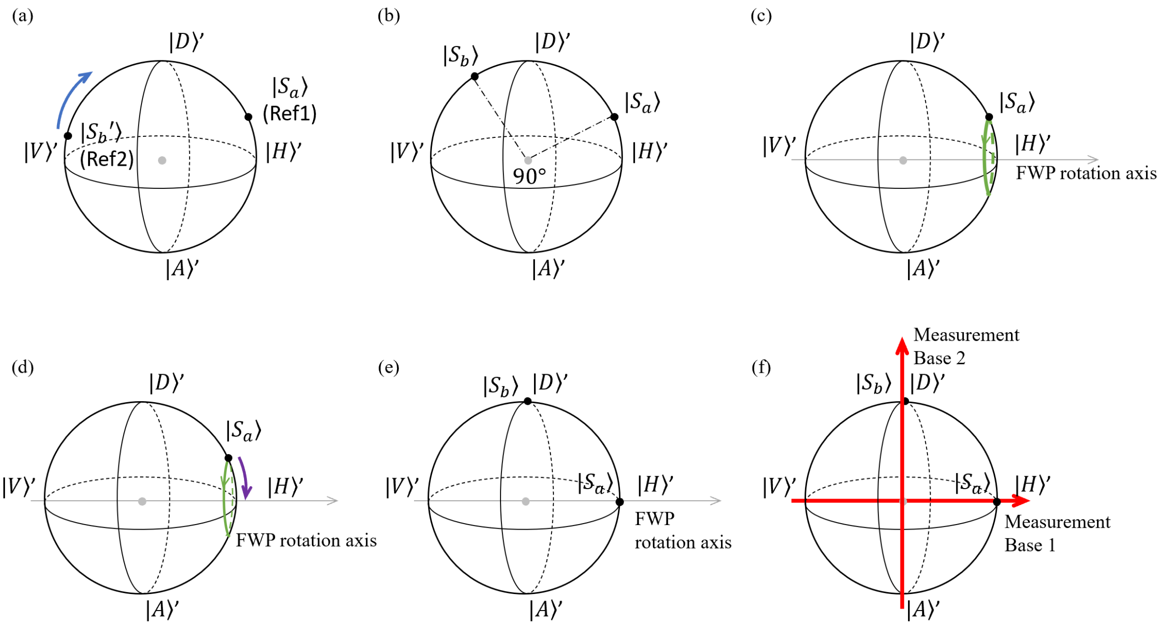

Fig. 4.6 Reference and detection alignment procedure illustrated on the Poincaré sphere. (a) Original states of the two references. The states are detected by a polarimeter based on which the EPC is operated to align the state $|S_b\rangle'$ to have orthogonal direction to $|S_a\rangle$. (b) Aligned two references. (c) Operation of the FWP from the polarisation controlling module would generate rotations on the two references. We connect $|S_a\rangle$ to the detection system to monitor the rotation after the FWP via a polarimeter connected at BS2. (d) Operation of EPC2 to minimise the rotation of $|S_a\rangle$. (e) Aligned $|S_a\rangle$ to the FWP rotation axis (f) Detection systems are aligned with first and second polarisation reference by an operation on EPC3 and EPC4.

The stabilisation system needs to be initially aligned to meet the following two requirements: the first being two detection bases matching the two reference states which have orthogonal directions on the Poincaré sphere; the second being rotation R_a and R_b corresponding to the operation on EPC and FWP respectively. The critical procedure here is to align $|S_a\rangle$ and the corresponding detection system to the FWP rotation axis. By doing so, any operations on the FWP (R_b) will not generate transformation on the $|S_a\rangle$ state. Following the system design in Figure 4.4, we developed alignment procedures explained below. Each of the following steps corresponds to a figure shown in Figure 4.6.

(a) The two initial reference states are represented by $|S_a\rangle$ and $|S_b\rangle'$. While maintaining $|S_a\rangle$, we operate EPC1 in Figure 4.4 (a) to align $|S_b\rangle'$ to reach a required state that has orthogonal direction with $|S_a\rangle$. A polarimeter is connected to the output port of OSW1 for monitoring this operation.

(b) shows the aligned second reference at the state $|S_b\rangle$.

(c) We start the alignment of the state $|S_a\rangle$ to the rotation axis of the FWP. In this system, a 90:10 BS (BS2 shown in Figure 4.4) is installed after EPC2 and the FWP. We connect the 10%

output to a polarimeter for monitoring the polarisation states after the controlling components and operate OSW1 to inject the first reference with the state $|S_a\rangle$. The FWP is then continuously operated, generating a circular movement on this polarisation state on the Poincaré sphere.

(d) Via operations on EPC2, the polarisation state rotation is minimised.

(e) When there is no states variation observed, $|S_a\rangle$ is aligned with the rotation axis of the FWP and $|S_b\rangle$ is at the equator.

(f) Align detection polarisation bases by adjusting EPC 3 and 4. By operating OSW 2 and 3, we connect EPC3 to calibrate the first detection basis. Instead of a polarimeter, the feedback signal is generated by the polarisation contrast value *pol* calculated from the measured optical power P_1 and P_2 by power meters PM1 and PM2 (equation 3.1). We operate EPC3 to maximise *pol*. After it is successfully aligned, we switch the system to the second reference by operating OSW 1, and the second detection basis by operating OSW 2 and 3. EPC4 is then operated to perform the same alignment.

4.3.3 Time-division multiplexing and system operation

We apply a time-division multiplexing (TDM) scheme to integrate the polarisation stabilisation system with the polarisation correlation setup introduced in Chapter 2. The overall system design is illustrated in Figure 4.7. Module A and B are the two parts, respectively for generating the polarisation references and for detecting the states, of the polarisation stabilisation system. The microPL setup and the spectral filter are in module C and the detection setup for correlation measurement are in module D.

The connection of these modules is controlled by OSW 4 and 5 in a TDM architecture. OSW4 is at one end of the installed fibre, and OSW5 is on the other end, connected after the polarisation modulation components. By controlling OSW 4 and 5, we can choose to send either qubits to the correlation measurement system by connecting module C and D; or the polarisation references to the polarisation detection modules by connecting module A and B. In this experiment, we keep X photons from the entangled photon pairs in the lab. The partner photons (XX) are sent over an installed loop-back fibre before measurement. The stabilisation system is only installed on the XX photon transmission path, with references at the wavelength at 1321 nm, same as the XX photon wavelength.

The initialisation of the polarisation stabilisation system requires the alignment that follows the procedure described in the previous section. We need high precision at each step to avoid accumulated deviation. Step (a) - (d) in Figure 4.6 are based on measurement by the polarimeter with a precision of 0.25°, which is also the precision for the two polarisation references. Alignment of detection bases requires several steps. During the FWP rotation operation as is introduced in step 4 in section 4.2, we keep on operating the EPC to align the input polarisation states to the FWP rotation axis. This procedure also has a precision of 0.25°. In the following step, as well as during stabilisation when *pol* is monitored, we introduce the threshold pol_{th} on

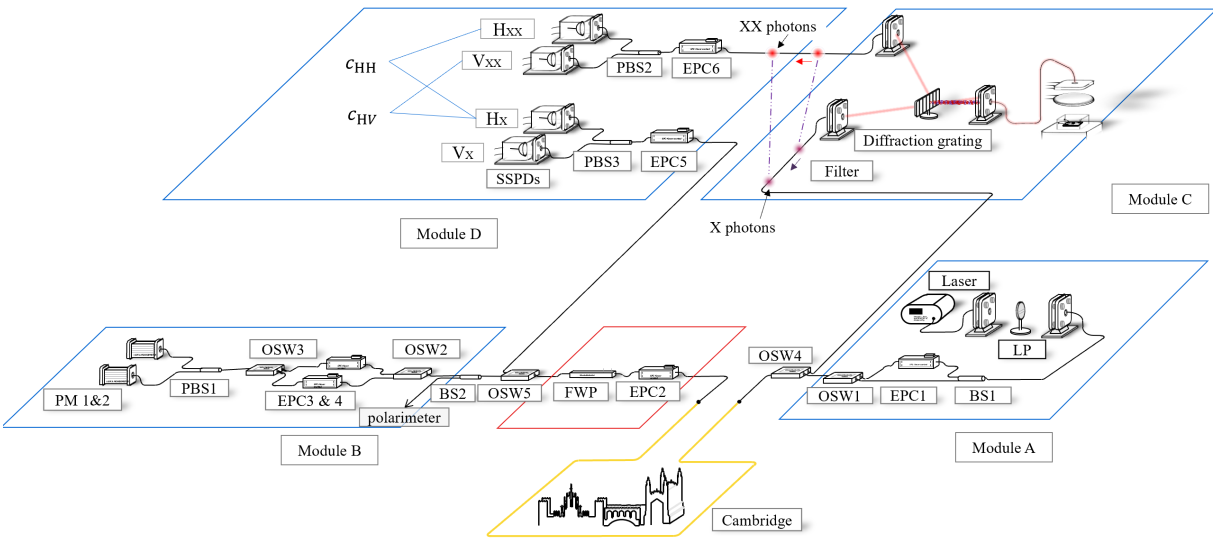

Fig. 4.7 Entanglement measurement setup with a polarisation stabilisation module. Module A and B are for polarisation reference generation and detection system corresponding to Figure 4.4 (a). Module C and D are for entangled photon pair generation and correlation measurement corresponding to Figure 2.8. All the modules are located in the laboratory. We keep XX photons in the laboratory and send the X photons to a loop-back fibre in the city of Cambridge and back. Polarisation references are time-multiplexed to the installed fibre with X photons, controlled by OSW 4 and 5.

the *pol* value. The decision to work with a certain threshold value in this work is empirical, taking into consideration the precision of the stabilisation and its time of operation. During step 6, we set the threshold to $pol_{th} = 0.9999$. It guarantees that the error of the polarisation references is limited within 1.6°, based on equation 4.5. It, in total, generates 2.1°of uncertainty along one measurement axis. Based on the analysis in subsection 2.3.2, this corresponds to a maximum fidelity drop by 0.1%.

We start polarisation stabilisation by operating OSW 4 and 5 to connect generated polarisation references to the detection arms, and OSW 1, 2 and 3 to connect the first polarisation reference to the detection bases calibrated by EPC3. We then operate EPC2 to bring the polarisation states of the first reference to match the detection state maximally. A threshold $pol_{th_1} = 0.9997$ is set, which corresponds to an angular deviation of 2.8 °in the worst case. Under this condition, the first reference states are considered to be aligned to the rotation axis of the FWP.

We then operate the FWP to recover the polarisation state of the second reference such that the detected polarisation projection value pol_2 is greater than a threshold $pol_{th_2} = 0.9993$. The reason for $pol_{th_2} < pol_{th_1}$ is to minimise the operation time. Operations on the FWP would not, in principle, generate polarisation variation on the first reference. However, due to the imperfection of the alignment and system components, as well as the optical fibre relaxation over a large time-scale, we have noticed a long-term polarisation drift of the aligned references during the experiment. Therefore, after stabilisation of the second reference, we switch back to check the first reference. This final step is to verify that the states of the first reference are not influenced by FWP operation by comparing pol_1 again with pol_{th_1}.

We then operate OSW 4 and 5 to send photons to SNSPDs over the deployed loop-back fibre. The entanglement fidelity is evaluated by measurements of correlations in 3 polarisation bases, as introduced in subsection 2.3.1.

When using time-division multiplexing schemes, it is essential to achieve high duty cycles and low optical loss for qubit transmission. Thanks to the installed fibre being buried underground, the birefringence changes slowly. During the correlation measurement, reference polarisation states are checked every 60 s, alternated between the first and second references. Intermittent polarisation checks are realised by OSW 4 and 5 to connect references to detection module and perform a single measurement. Each check takes about 0.5 s, corresponding to a duty cycle of 99%. If measured pol_1 and pol_2 is greater than the corresponding $pol_{th} = 99.5\%$, we switch back to the quantum channel. Otherwise, we then operate EPC2 and the FWP to recover both references to their original states respectively, taking on average 5 s. This would result in a duty cycle of 92%. Apart from the threshold-based check, the recovery system was activated around every 11 minutes to maximise the alignment for both references. Thus, an overall duty cycle of 98% is achieved. The combined loss in this work from OSW 4 and 5, EPC 2 and the FWP is 3.49 dB at the telecom O-band.

Each component is affiliated with control hardware that is operated via a software interface on LabVIEW on a PC. EPC controllers are provided by OZ optics supplying four-channel operation. It is connected to the PC via USB. The OSWs are operated by applying a 2 ms width pulse. Thus we have introduced an Arduino micro-controller to apply the pulses. For operating the FWP, we integrate a motor shield driver hardware onto the Arduino platform as a current source. The Arduino script is interfaced with LabVIEW.

4.4 Correlation measurement with polarisation stabilisation

Obtaining entanglement from qubits transmitted over an optical fibre deployed in the field is an important step toward the network integration of the sub-Poissonian entangled photon-pair sources. With such a target, we have carried out a correlation measurement for obtaining entanglement over an installed loop-back fibre with the polarisation stabilisation system. The installed fibre has a length of 18 km, starting from Toshiba Cambridge Research Laboratory (CRL) to the Cambridge city centre and back.

In this experiment, we use the same QD as the one in Chapter 2 operated in PL. The setup for exciting the InAs QD, collecting the emitted light, aligning the measurement bases and performing correlation measurement is the same as that introduced in Chapter 2. We operate the polarisation stabilisation system to reach the stabilised polarisation states first to ensure the alignment of the correct base for correlation measurement. Figure 4.8 (a) (b) and (c) shows the measured polarisation correlation in 3 bases: $|HV\rangle$, $|DA\rangle$ and $|RL\rangle$ over a 30 minutes time slot. The entanglement fidelity is evaluated by the above measurements by equation 2.24, with the result shown in Figure 4.8 (d). The maximum entanglement fidelity of $90.1 \pm 2.3\%$ is achieved. For comparison, the entanglement fidelity measured without sending the photons over the loop-back link is $(94.7 \pm 1.7)\%$.

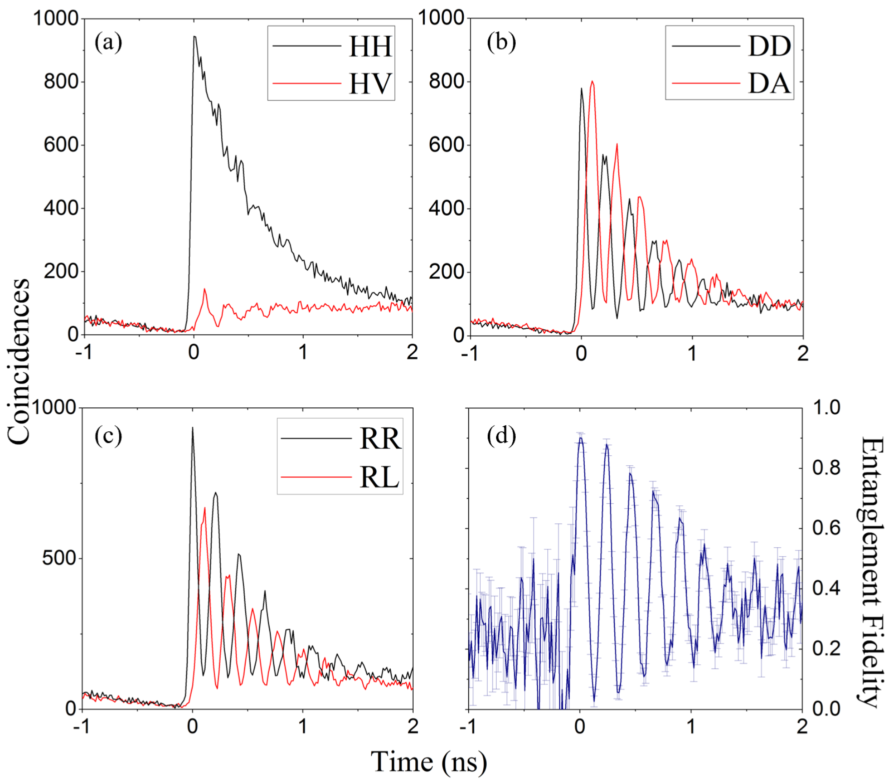

Fig. 4.8 Correlation measurement and entanglement fidelity evaluation over an installed loop-back fibre with the stabilisation system. Correlation is evaluated in (a) $|HV\rangle$, (b) $|DA\rangle$ and (c) $|RL\rangle$ bases and the coincidences are recorded for 30 minutes in each base. (d) shows the entanglement fidelity evaluated from the correlation measurements.

The major reason for such a reduced entanglement fidelity is the misalignment of correlation measurement bases. In the correlation measurement on the $|HV\rangle$ basis in Figure 4.8 (a), one could see an oscillating cross-polarised coefficient curve close to the zero-delay. It is an indication of a slightly misaligned $|HV\rangle$ detection basis given that the aligned bases to the QD eigenbasis should be not subject to the phase oscillation introduced by the FSS. Based on the previous analysis that the fidelity drop introduced by the limited precision of the polarisation stabilisation system is 0.1%, the majority of the drop is from the misalignment of the correlation measurement bases. In Chapter 5, we introduce an improved method for aligning the correlation measurement bases for this purpose.

To test the long-term operation capability of the polarisation stabilisation system, we have continuously recorded the entanglement fidelity for seven days [118]. In addition to the polarisation states variation, changes in the environment such as temperature and stress as well cause a change of the effective optical length of the installed fibre. Given that no active synchronisation system is added as both XX and X photons are measured by different channels on the same time-correlation unit, the zero-delay information needs to be obtained for the evaluation of the entanglement fidelity. Figure 4.9 (a) shows one normalised dataset of measured coincidences of co-polarised correlations between X and XX photons in $|HV\rangle$ for 30 minutes, with a time-bin size of 8 ps. The zero-delay drift is negligible over this time-scale. We obtain the ideal function for co-polarised coincidences in HV from equation 2.20:

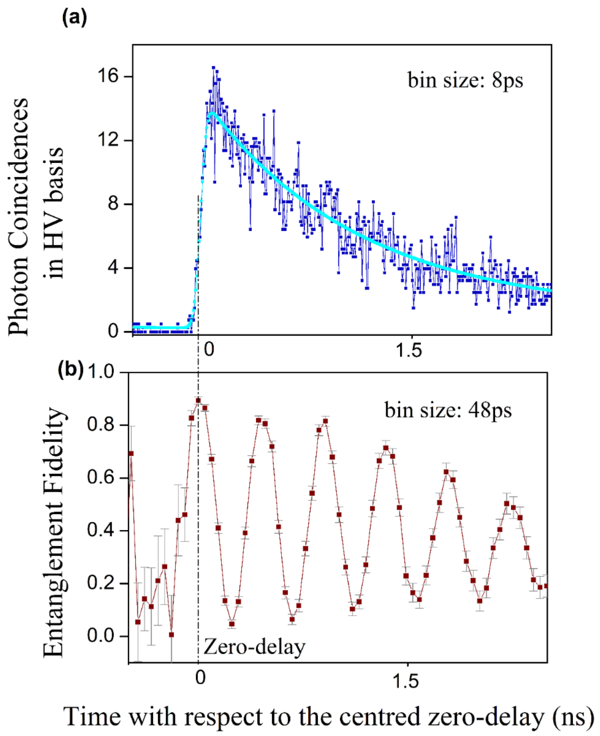

Fig. 4.9 Photon correlations and entanglement fidelity from the QD emitter for a single experimental data set. (a) The normalised co-polarised coincidences from the correlation measurement under $|HV\rangle$ bases with an empirical fitting. (b) Entanglement fidelity as a function of the delay between X and XX photon.

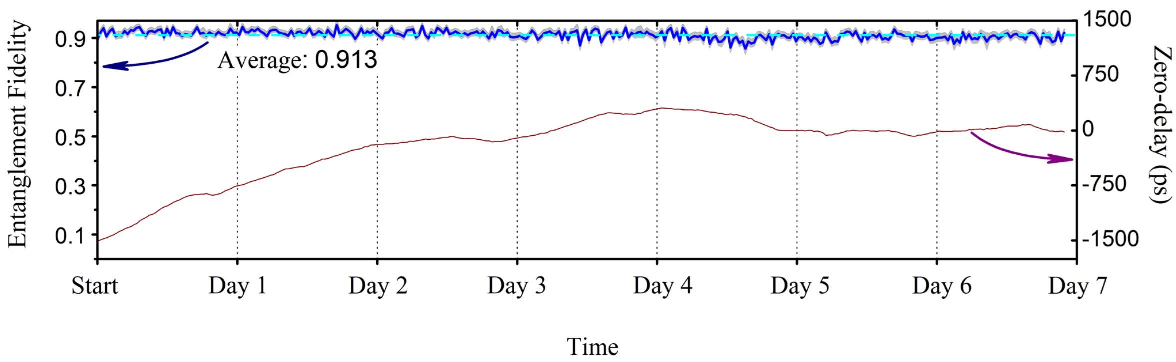

Fig. 4.10 Entanglement fidelity and relative change of qubit transit time over the field fiber for 7 days of continuous operation. The mean fidelity is $(91.3 \pm 1.4)\%$. The gray shaded area indicates one standard deviation. Error bars for the delay values are negligible.

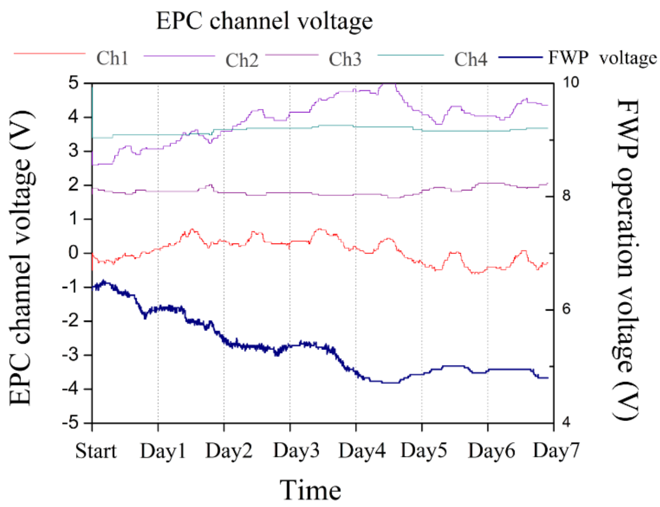

Fig. 4.11 Operation voltage for EPC5 and FWP over the course of the measurement.

$$c_{HH}(t) = bg, (t < t_0); \quad bg + Ae^{(} - \frac{t - t_0}{\tau}), (t > t_0) \tag{4.6}$$

where bg is the background, A is the scaling factor, τ is the photon lifetime and t_0 is the zero-delay value. We convolute the above function with the overall timing jitter of the detection system 70 ps:

$$c_{real}(t) = conv(c_{HH}, 70(ps)) \tag{4.7}$$

We fit the coincidences with c_{real} and obtain t_0. The impact of these changing environmental conditions can be seen in the drift of the time-of-flight of photons of 1.82 ns over the first four days.

The overall results are shown in Figure 4.10. Displayed are the entanglement fidelity and the change in time-of-flight as a function of measurement time. A consistently high entanglement fidelity is achieved over the entire week, with an average value of $(91.3 \pm 1.4)\%$. During the week, the weather has changed drastically with rain and snow, with the temperature variation from -4 to 7 °C.

Figure 4.11 shows the voltages applied to the four channels of the EPC and the FWP as a result of the feedback generated to keep the birefringence stable. Superimposed to the steady drift over the first four days, one can see clear oscillations in EPC and FWP operation voltages corresponding to the day-night cycle of temperatures.

It is important to point out that most of the long-distance fibre networks are equipped with optical amplifiers, which generates significant quantum noise and decoherence [119]. Hence, the entanglement will fail in a fibre network where optical amplifiers are applied.

4.5 Wavelength-division multiplexing scheme

In addition to the TDM scheme introduced in the previous section, we have, in the beginning, adopted a wavelength-division multiplexing (WDM) method to the polarisation stabilisation system, which however failed to stabilise the polarisation. This section introduces the attempts of building such a polarisation stabilisation system and analyses the reason for its failure by introducing polarisation mode dispersion.

Figure 4.12 shows the wavelength-division multiplexing schemes during our initial trial. (a) and (b) show two different approaches to generating polarisation references. In (a), the references are generated using a broadband LED emitting at telecom O-band. It passes a dense wavelength-division multiplexer (DWDM1) with output wavelengths at 1317 nm, 1319 nm, 1321 nm and 1323 nm. And we select the light from 1319 nm and 1323 nm output ports as two polarisation references, which are then combined by DWDM2. The QD is tuned to emit XX photons at 1321 nm, at the centre of the two reference wavelengths.

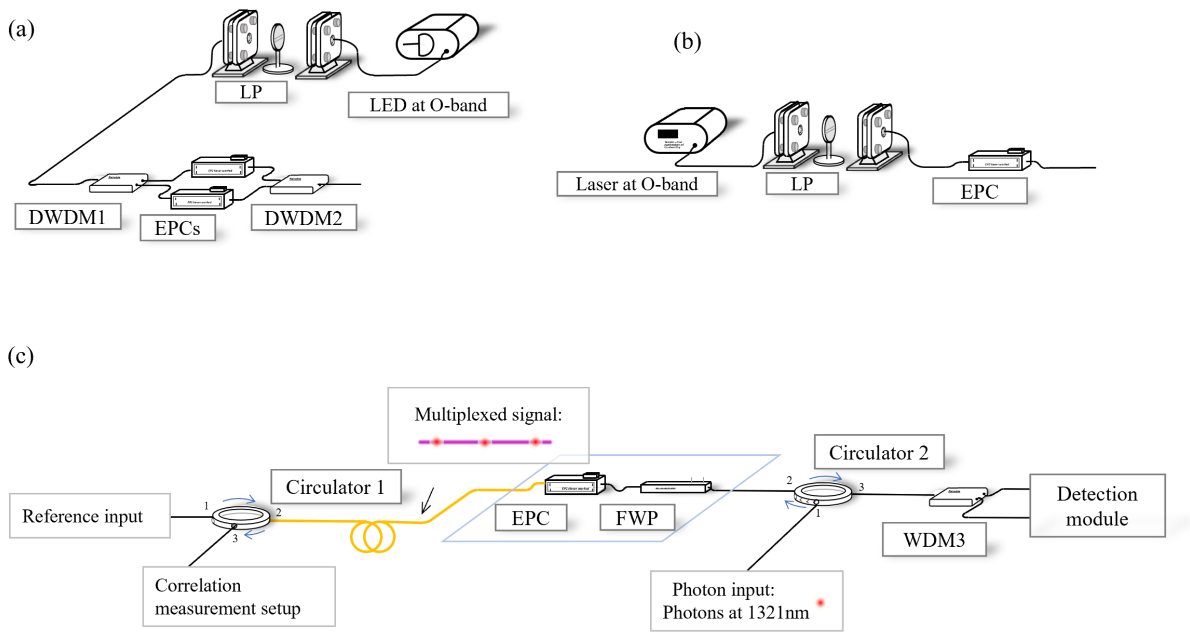

Fig. 4.12 (a) A polarisation reference generation module based on a broadband LED for the wavelength-division multiplexing (WDM) scheme. The light passes the LP, split by the first dense wavelength-division multiplexer (DWDM1) to two references. Each reference is modulated by an EPC. They are combined by DWDM2. (b) An alternative method for generating the polarisation references using a laser. An EPC is in use here with two operational voltage sets that align the polarisation references to required states. (c) The separation between polarisation references and qubits by optical circulators. The two optical circulators have the circulating direction from port 1 to 2, and from port 2 to 3. Polarisation references generated from (a) or (b) and transmitted photons emitted from the QD is separated by these two circulators. The detection module is the same as that in the time-division multiplexed system.

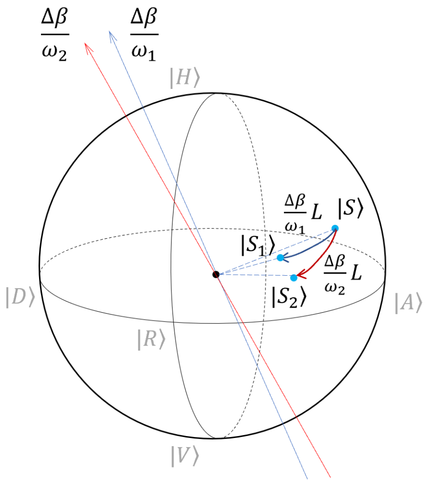

Fig. 4.13 Illustration of fibre birefringence dependence on the light frequency. The two axes $\frac{\Delta\beta}{\omega_1}$ and $\frac{\Delta\beta}{\omega_1}$ represents the fibre birefringence direction on the Poincaré sphere. Hence, the input polarisation state with different input frequencies would evolve along a different direction.

The scheme shown in Figure 4.12 (b) uses a single laser emitting at 1323 nm as polarisation references, 2 nm longer than the transmitted photons. Two sets of EPC operational voltages are stored, each respectively aligns the laser light to polarisation states with orthogonal directions on the Poincaré sphere. Hence, the setups in (a) and (b) are different in that (a) shows references at two different wavelengths, with a broader linewidth around 1nm.

The polarisation references are then connected to the installed fibre. It passes a similar polarisation controlling module consisting of an EPC and a FWP to the detection module, as is shown in Figure 4.12 (c). Optical circulators (Circulator 1 & 2) are installed at both ends of the installed fibre to separate the quantum signal with classical polarisation references. Both of the circulators have the light propagation direction from port 1 to port 2, and from port 2 to port 3. Hence, the module for entangled photon pair generation and the module for polarisation reference generation have to be connected to the opposite ends of the installed fibre, resulting in the polarisation references travelling at an opposite direction of the photons.

Alignment of the system follows the same principle as is introduced in the section 4.2.2, with the polarisation state and detection bases of the first references aligned along the rotational axis of the FWP and those for the second references aligned to an orthogonal direction on the Poincaré sphere. For the reference generation setup in Figure 4.12 (b), the EPC operation voltages for four channels of each base is stored, and activated during the stabilisation.

Several tests on the performance of the stabilisation system are carried out, both with and without the correlation measurement conducted in parallel. When applying polarisation references generated using the setup illustrated in Figure 4.12 (a), we have discovered a degree of polarisation (DOP) drop on both references when using the broadband LED as the source. And the threshold for polarisation project value pol_{th} had to be set to as low as 0.98, corresponding to a polarisation uncertainty over 22°. Cross-talk between the channels is one of the reasons

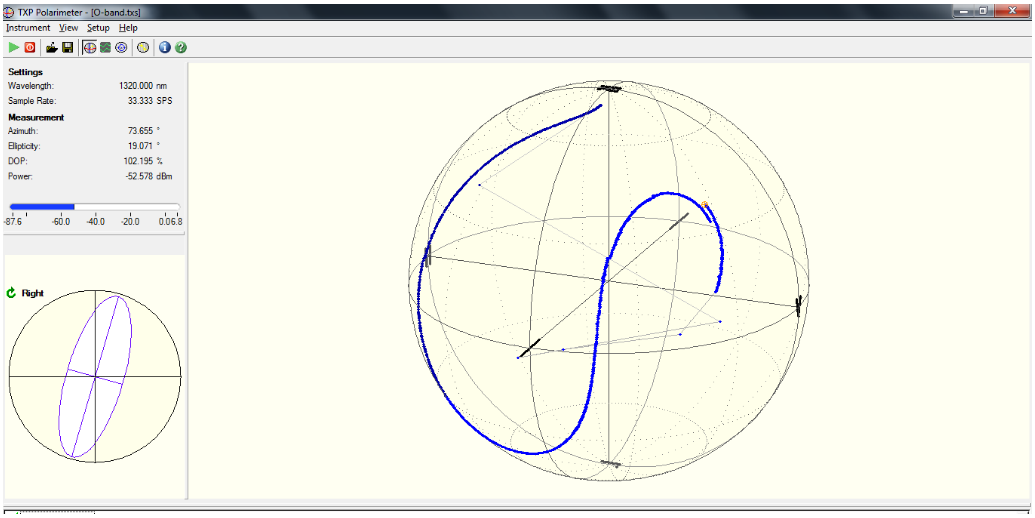

Fig. 4.14 A measurement of the output polarisation state shown on the Poincaré sphere after the input light propagates over the 18 km loop-back fiber, with the wavelength changing from 1315 nm to 1325 nm.

for the drop of DOP. The DWDMs installed in the system have channel isolation of 25-40 dB. Therefore, when detecting one reference, one simultaneously detects the other reference which has a different wavelength with a different polarisation state. We further observed that the original two reference states with orthogonal directions on the Poincaré sphere have become non-orthogonal over a large time-scale, finally resulting in a failure of the stabilisation.

The major reason for the failure of such a scheme is the uncertainty introduced by polarisation mode dispersion (PMD). It is introduced by the residual birefringence of a SMF, breaking the degeneracy of the fundamental spatial mode into two orthogonal polarisation modes, introducing a time delay between them that gives rise to signal distortion. It is associated with the following polarisation dispersion vector:

$$\Omega(\omega) = \Delta\tau_g \overrightarrow{s} \tag{4.8}$$

where $\Delta\tau_g$ is the differential group delay (DGD): $\Delta\tau_g = \frac{\partial\beta}{\partial\omega}L$ following equation 4.2, and $\overrightarrow{s}$ is a unit vector pointing in the direction of the fast axis of the birefringence optical fibre. It is referred to as the first-order PMD. In the transmission where the long installed optical fibre is used, the second-order PMD needs to be considered due to the frequency-dependency of PMD (sometimes referred to as chromatic dispersion):

$$\Omega_\omega = \frac{\partial\Omega(\omega)}{\partial\omega} = \frac{\partial\Delta\tau_g}{\partial\omega}\overrightarrow{s} + \Delta\tau_g\frac{\partial\overrightarrow{s}}{\partial\omega} \tag{4.9}$$

The second term $\Delta\tau_g\frac{\partial\overrightarrow{s}}{\partial\omega}$ indicates the variation of optical fast and slow axes based on frequency, which leads to the frequency-dependent randomised polaristaion change in our case. Considering the Poincaré sphere representation of it in Figure 4.13 where the variation of fibre birefringence direction is indicated, we notice output polarisation states vary when the input

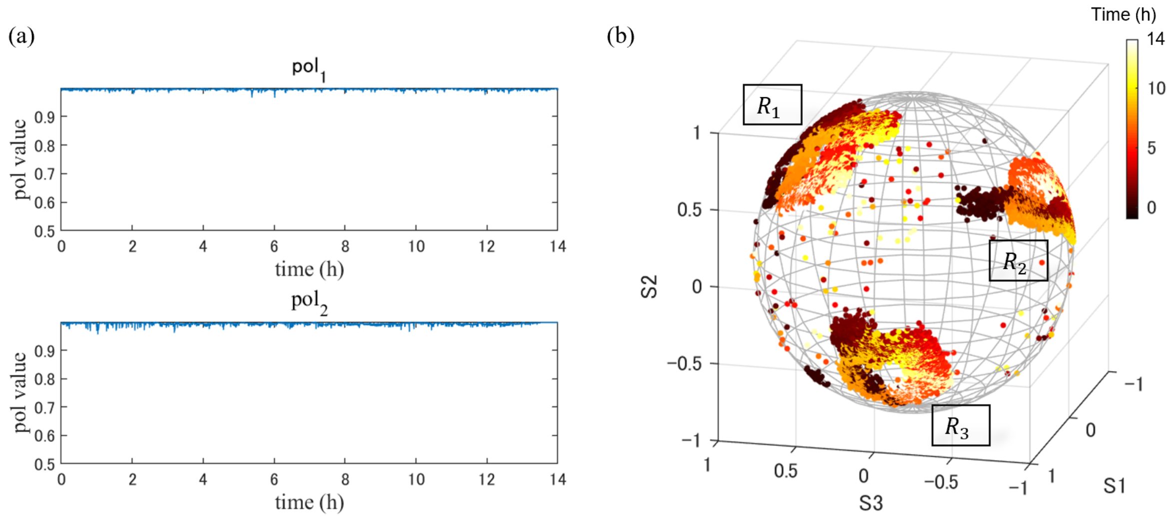

Fig. 4.15 The test result on the WDM-based polarisation stabilisation system. (a) The *pol* value on the two polarisation references, recorded when the stabilisation system is activated. For most of the time, the *pol* values stay above 0.99. (b) The variation of three states $|R_1\rangle$, $|R_2\rangle$ and $|R_3\rangle$ with orthogonal directions on the Poincaré sphere at the quantum channel. They are measured by a polarimeter at the output of the quantum channel on the other end of the installed fibre. We have used a colour map to represent the measured polarisation states over the period to view the time-dependent polarisation variation.

states have different wavelengths. We have performed a test by injecting a tuneable laser to the installed fibre with a linear polarisation state, and measure the output polarisation states while changing its input wavelength. Figure 4.14 shows the output states shown on the Poincaré sphere measured by a polarimeter. Given that the references generated by filtered broadband LED light both to have the bandwidth of around 1nm, a potential output polarisation states spans across a range of around 20°. As a result, the DOP of the light will be reduced. The feedback signal *pol*, therefore, becomes inaccurate as there will not be a perfect polarisation match between the PBS output port and the polarisation states at the measurement port.

The reference generation scheme shown in Figure 4.12 (b) is built to solve this problem, with the input references at the same wavelength. Successfully, we have managed to maintain a high *pol* value for over one day. A stability test on such a system is then performed. We alternate an LED light filtered to the same wavelength as the XX photons using a DWDM with polarisation states having orthogonal directions on the Poincaré sphere to be injected from the quantum channel on one end, and measure their states using a polarimeter on the other end. The polarisation stabilisation system is continuously operated, and the test lasts for 14 hours, with *pol* recorded when the stabilisation system is operated. The result is plotted in Figure 4.15. (a) shows the recorded *pol* values for both references. When performing this measurement, we have used a lower threshold value of $pol_{th'_1} = 0.995$ and $pol_{th'_2} = 0.99$. For most of the time, the threshold condition is fulfilled. However, polarisation drifts with maximum degrees of around 45 °are noticed in the quantum channel on the three states.

Such a phenomenon could be explained by time-dependent PMD [120]. Over a long period, the fibre birefringence of an optical fibre in a field environment experiences certain wavelength-dependent variance. Both the variance and its dependence on the wavelength are randomised over a large time scale. Given that both the EPC and the FWP generate fixed linear operations on polarisation states with less obvious frequency-dependent variation, the applied compensation signal does not stabilise the polarisation over a long period.

Therefore, we decided to adopt the time-division multiplexing scheme to the transmission system to apply the polarisation references at the same wavelength as photons.

Chapter 5

Remote Correlation Measurement Bases Alignment

5.1 Remote alignment based on measuring emission spectra

The polarisation stabilisation system introduced in Chapter 3 successfully maintained the entanglement fidelity when qubits are sent over an installed loop-back fibre. In that experiment, the detection system and QDs were located at the same location in a laboratory. It facilitates the alignment of correlation measurement bases and polarisation references and provides environmental support for a bulky setup with high stability. However, the laboratory equipment is not at all prevalently available, and a more compact setup supporting a non-laboratory environment is required. Qubits in a realistic quantum network would be sent to different locations. Therefore, a deployable source and alignment system for correlation measurement bases need to be installed to enable the transmission in such a case. In terms of the source, the OCP device introduced in the previous chapter works in a full electrical environment that supports both driving and tuning of the QD. In this chapter, we take a further step on establishing an alignment system for calibrating the polarisation correlation measurement bases.

We review the correlation measurement setup in Figure 2.8, where the alignment is performed with a reference installed on top of the cryostat near the fibre coupler. This installation gives it a great advantage of being free-space, facilitating the matching of the polarisation reference state to an eigenstate of the emitted photons. However, the references need to be installed directly above the QD, with a flip mirror controlling its injection to the optical path. Such a setup is difficult to be implemented with a real-world scenario with potential future photonic integration and fibre pig-tailing of the QD device. Therefore, larger spatial separation of the polarisation references system with the source is necessary for practical application. In a fibre-based optical setup, it means that an optical fibre would be installed between the optical collection module for the QD and the point for reference injection and calibration with an unknown unitary transformation in

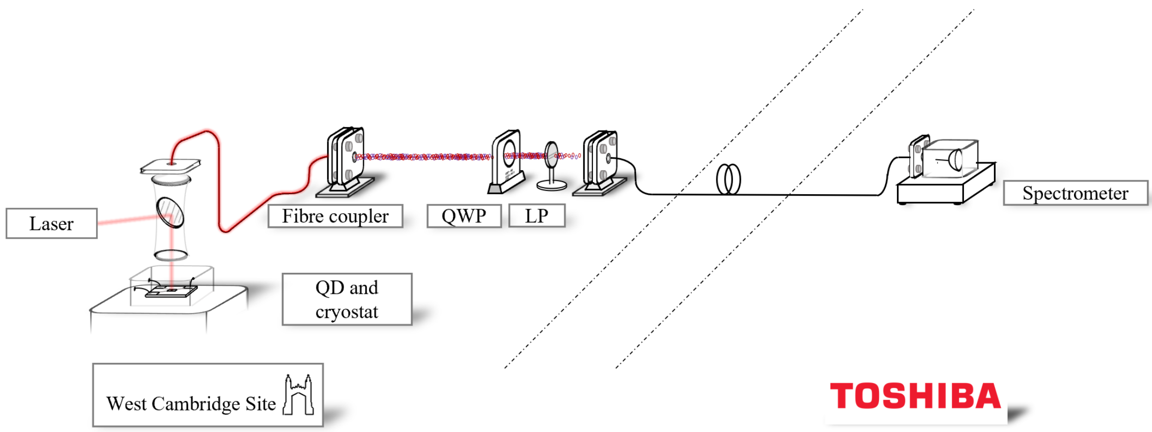

Fig. 5.1 The typical FSS measurement setup in a network environment. The spectrometer might be geographically separated from the QD in certain scenarios. In this case, the QD is located at an office of the Cavendish Laboratory in West Cambridge, whereas the spectrometer is located at the Toshiba Cambridge Research Laboratory (CRL).

between. Hence, the QD references cannot be aligned to the emission eigenbasis without the knowledge of such a unitary transformation.

The new method developed in this work is to obtain the transformed eigenstates at the position where the reference is installed, such that the unitary transformation could be reconstructed. When reviewing equation 2.9, one could notice that by fitting a curve to the measured photon energy by the spectrometer in the setup for measuring FSS using the QWP rotation method, the transformed eigenstates before the QWP could be obtained from θ and ϕ values. Hence, we installed such a setup at the two remote locations, as is shown in Figure 5.1. In this figure, the QD is installed in a closed-cycle cryostat in an office at the Cavendish Laboratory of the University of Cambridge (CAM). An optical fibre is installed to connect it to the QWP and LP polarisation analyser setup. It then passes a deployed fibre to reach the spectrometer, located at CRL with the length of 15 km to connect the two locations. The spectrometer is not deployable due to the requirement of liquid nitrogen for its operation.

The XX and X photon energy is required to obtain the transformed eigenstates at the QWP. And it could be achieved by fitting narrow Gaussian curves to the emitted photon spectra. When the source is deployed, emission from the QD would be transmitted over a long optical fibre before measured. It firstly introduces high optical loss that significantly reduces the signal measured by the spectrometer. Figure 5.2 (a) shows a measurement result with an integration time of 20 seconds. The rate of XX and X photons are much lower compared with in-laboratory measurement, only at about 40 counts per second at the spectrometer. It means a less signal-to-background ratio for the measured spectrum.

On the other hand, the introduced Raman scattering broadens the linewidth of each photon lines, and channel crosstalk further increases the background. The above factors result in a less precise Gaussian fitting for obtaining the photon energy. Figure 5.2 (b) shows a measurement

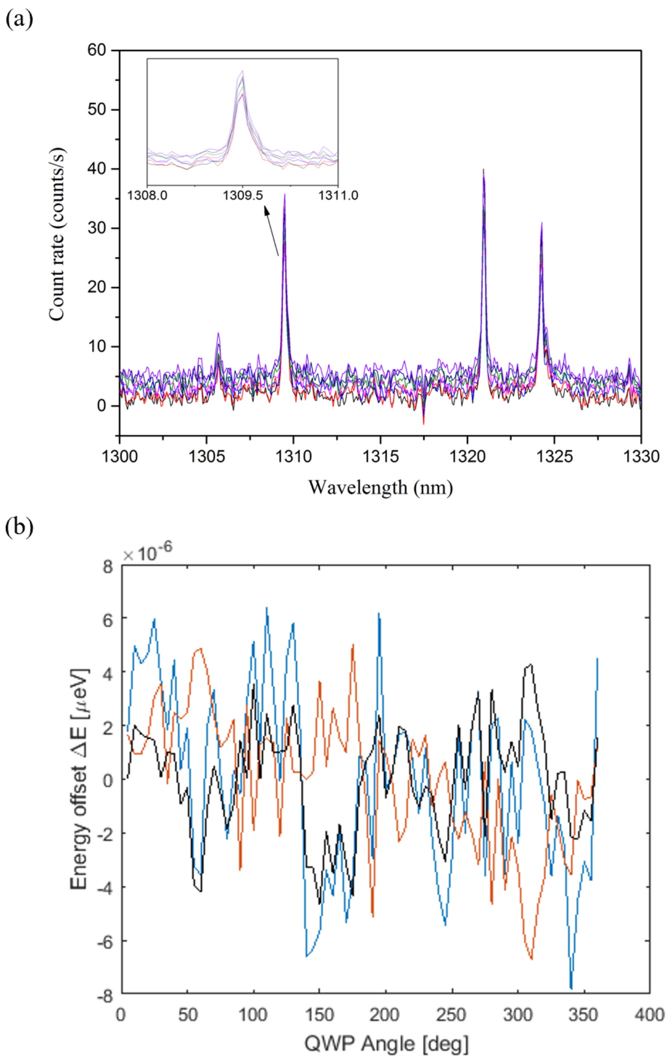

Fig. 5.2 QD emission spectra measured remotely. (a) The spectrum is measured with the QD installed 15 km apart from the spectrometer, connected via an optical fibre. The measurement is performed with a QWP rotation step size of 2°and an integration time of 20 seconds for each spectrum. (b) The change of XX (black), X (red) and the offset (blue) energy with the QWP rotation angle is obtained.

result on the XX/X photon energy and their offsets with the QWP rotation, shown respectively with black, red and blue lines. In this measurement, the deviation is so high that a numerical fitting by equation 2.9 cannot be obtained.

Therefore, it is impossible to obtain an accurate reference state from this method unless there is a deployable spectrometer, which is not available due to the health and safety issues. We have thus introduced a new method for alignment in the time domain.

5.2 Remote alignment based on correlation measurement

5.2.1 Measurement system

The inspiration for the new alignment method comes from the correlation measurement itself. When we analyse the co- or cross-polarised correlation of a superposition state, an oscillation is observed on an overall decay envelope, following equation 2.20. Not only the QD FSS, but also the photon eigenstate (represented with θ and ϕ values) influences the oscillation curve. Therefore, analysis of the correlation could allow one to get an accurate measurement state.

Different from the correlation measurement setup shown in Figure 2.8, the reference for calibrating the QD measurement bases is injected before the spectral filter, shown in Figure 5.3. The mirror is used to switch either the polarisation references or the entangled photons to the spectral filter and following detection setups. The reference is generated by an LED at telecom wavelengths, passing a polarisation modulation setup consisting of a LP, a HWP and a QWP.

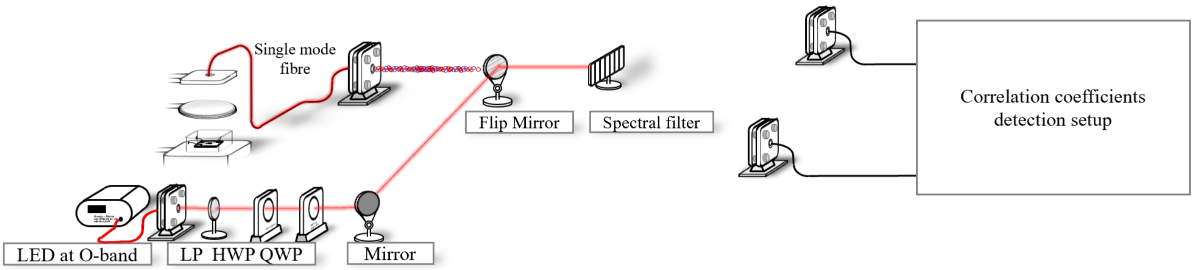

Fig. 5.3 Remote alignment setup of the correlation measurement bases. An LED generates polarisation references for calibrating the detection bases with a polarisation modulator consisting of a LP, a HWP and a QWP. It is switched into the main transmission fibre by a flip mirror before the spectral filter. The following setup is the spectral filter and the detection module, the same as a traditional correlation measurement setup (Figure 2.8)

5.2.2 Alignment method

The method works as follows. We first take X-XX correlation measurements (co- and cross-polarised) in three well-known arbitrary but linearly independent detection bases in the references frame of the polarisation references. The time-dependent evolution of the correlation signal is then analysed to extract the exact orientation of each of the three reference states in the reference frame of the eigenbasis of QD emission. Using the standard procedure for Müller matrix evaluation, we calculate the transformation matrix between the polarisation reference and the QD eigenbasis which enables the generation of perfectly matching reference states for detector calibration in the second step.

The three polarisation reference states are generated by operating the HWP and QWP after the LED. To avoid confusion, we here use labels $|H_R\rangle$, $|D_R\rangle$ and $|R_R\rangle$ to represent the polarisation states in the reference frame of the polarisation reference. Following the same basis alignment procedure in Chapter 2, we align the two detection modules respectively to the generated references by operating the EPC and minimising the count rate on the corresponding SNSPDs for both co- and cross-polarised cases.

We then flip the mirror to connect the entangled photons to the detection system and perform a correlation measurement. By fitting the measured correlation coefficients with equation 2.21, we can extract precise values for for angles θ and ϕ. The relation between these angles and the corresponding Stokes parameters s_1, s_2, s_3 is given by equation 2.41. The polarisation transformation of an optical fibre or other linear optical elements is described by the Müller matrix M.

$$S_m = M \; S_r \tag{5.1}$$

Where S_r is the Stokes vector for the orientation of the polarisation detection system, being calibrated by a corresponding reference state. S_m is the Stokes vector extracted from fitting equation 2.20 to photon pair correlations, which describes the orientation of the QD eigenbasis with respect to the calibration reference state.

As mentioned previously, we have calibrated three detection bases to $|H_R\rangle$, $|D_R\rangle$ and $|R_R\rangle$. Therefore, we will have three sets of Stokes vector for S_m and S_r. It is then convenient to write them in a matrix form:

$$S = \begin{bmatrix} S_1 & S_2 & S_3 \end{bmatrix} = \begin{bmatrix} 1 & 1 & 1 \\ s_{11} & s_{21} & s_{31} \\ s_{12} & s_{22} & s_{32} \\ s_{13} & s_{23} & s_{33} \end{bmatrix} \tag{5.2}$$

The DOP here is considered to be 1. s_{n1-3} are the corresponding Stokes parameters.

It is straight forward to reconstruct M from a set of calibration states (e.g. S_r in $\{H,\ D,\ R\}$) and their corresponding measured vectors S_m [42]:

$$M = S_m S_r^{\dagger} \tag{5.3}$$

where $S_r^{\dagger}$ is the pseudoinverse matrix of S_r, defined by

$$S_r^{\dagger} = (S_r^* S_r)^{-1} S_r^* \tag{5.4}$$

Mathematically, the number of input states is not fixed as the above function could always get a valid result by pseudo-inverse matrix calculation. The main reason for having these three polarisation states at orthogonal directions on a Poincaré sphere is to better define M in its three Euler angles, given that the states S_m are obtained via a numerical fitting on the measured polarisation correlation coefficients. Knowledge of M then enables the deterministic setting of reference calibration states $S_{r'}$ that perfectly match the principal polarisation states S_{eigen} in the reference frame of the QD emitter.

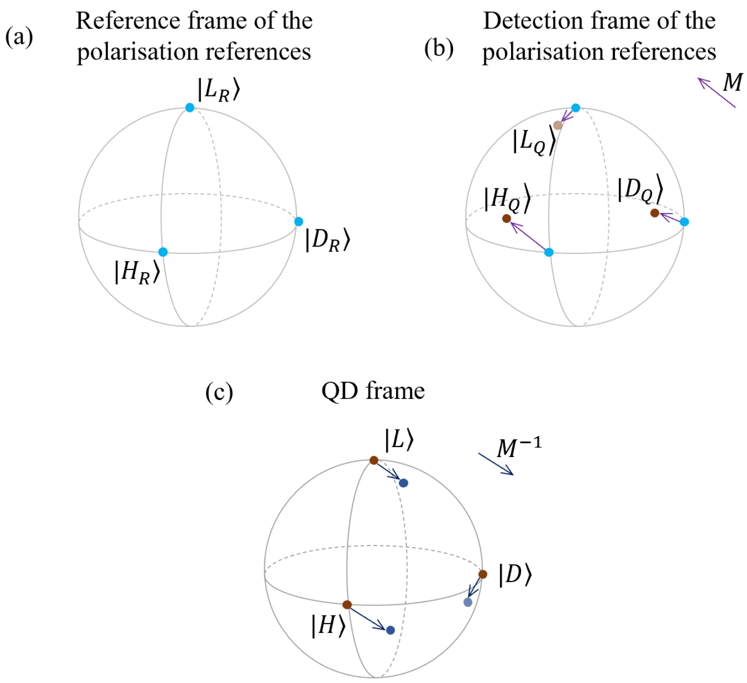

Fig. 5.4 Illustration of the Müller matrix transformation method shown on the Poincaré sphere. Poincaré spheres in (a) and (b) represents the sphere in the frame of the detection basis. (a) shows that the bases are initially aligned to three reference states $|H_R\rangle$, $|D_R\rangle$ and $|R_R\rangle$, based on which the correlation measurement is conducted. Fitting of the correlation measurement results in the states shown in (b). $|H_M\rangle$, $|D_M\rangle$ and $|R_M\rangle$ are the polarisation bases with the same alignment as (a), but when the input source is at the QD propagating via a short optical fibre. We combine the state information of (a) and (b) to acquire the transformation matrix M. The sphere in (c) is in the reference frame of the QD. An inverse calculation then calculates the required reference state on QD eigenbases, shown in (c).

$$S_{r'} \; = \; M^{\dagger} \, S_{eigen} \tag{5.5}$$

One could use more reference input states for further improvement of accuracy.

The above transformation could be understood in the illustration shown in Figure 5.4. The Poincaré spheres in (a) and (b) are in the reference frame of detection bases, while the sphere in (c) is in the reference frame of QD polarisation eigenbases. The detection bases were initially aligned to references with states $|H_R\rangle$, $|D_R\rangle$ and $|R_R\rangle$ at the position where the references are injected, shown in (a). After a set of correlation measurements is performed on the entangled photon pairs emitted from the QD, we obtain the aligned bases indicated as $|H_M\rangle$, $|D_M\rangle$ and $|R_M\rangle$ shown in (b). Therefore, the transformation introduced by the optical fibre, represented by matrix M, could be calculated by the states from (a) and (b) using equation 5.3. Therefore, reference states $S_{r'}$ enabling the detection bases matching $|H\rangle$, $|D\rangle$ and $|R\rangle$ of the QD bases could be calculated by equation 5.5, shown in (c).

Once S_r' is calculated, one needs to rotate HWP and QWP in Figure 5.2 to certain angles to align the polarisation references to the required states. These angles are is calculated by equation 2.35. The photon detection system is then aligned to the calculated angles. This set of angle would then correspond to the states $|HV\rangle$, $|DA\rangle$ and $|RL\rangle$ in the reference frame of the QD.

5.2.3 Alignment precision

Acquisition of precise reference calibration states $S_{r'}$ needs a very accurate expression of the transformation Müller Matrix M. This requires high precision of reference states S_r and the fit states S_m.

The deviation on the actual S_r states from the ideal case comes from two effects. Successful implementation also relies on accurate S_m, which is obtained by fitting the correlation measurement curve using equation 2.21 in subsection 2.3.1. Therefore, we need to have high enough statistics on the measured correlation curves. In a laboratory environment where the XX and X photon rate could be over 200 kHz, it is easy to obtain a proper measurement result in 5 minutes integration time. However, in a field environment with high optical loss in the optical fibre, the rate goes down to below 20 kHz. Hence, we integrate the correlation measurement for 30 minutes on each basis.

Another factor is the error generated by the imperfect rotation of waveplates. One would expect a precise transformation of waveplates that supports accurate fitting. However, such a condition could not always be achieved. The waveplates are wavelength-dependent; hence the degree of polarisation is reduced when a light source such as a broadband LED is used as the reference.

The mechanical alignment of the waveplates is another issue. The plates need to be placed perpendicularly to the light propagation direction for their normal operations. In practice, even taking great care during the installation and alignment, there still exists certain uncertainty.

Hence, the angular deviation would influence the projected light onto the fast and slow axis, simultaneously changing the output polarisation state.

As to be noticed for equation 2.20 that the term that contains θ is in its second order. Therefore, more than one θ value can be found for one curve. For each given θ_0 that meets the function, $\pi - \theta$ also meets the same requirement. Therefore, more than one possible state could be obtained by the fitting. Normally, only one set of measured states would satisfy the condition of having orthogonal directions. Thus, an additional filtering procedure is implemented to identify the correct set of S_m.

5.2.4 Alignment in practice

The alignment method is tested with a deployed QD. The details of the deployment are shown in Chapter 7. Figure 5.5 (a) - (c) shows the measured co- and cross-polarised correlation coincidences of entangled photon pairs emitted from the QD when the bases are aligned to $|H_R\rangle$, $|D_R\rangle$ and $|L_R\rangle$ in the reference frame of the polarisation references. A fitting function here is used based on the correlation coefficient (equation 2.21), defined as:

$$p_{fitting} = A(1 - \sin^2\theta(1 - \cos(\frac{\delta}{\hbar}t - 2\phi))) \tag{5.6}$$

where A is an amplitude modulating factor. We introduce this factor mainly due to the difficulty of normalisation of the measured correlation coefficients that match the function describes by equation 2.21. Therefore, during the fitting, we normalise the measured correlation coefficients by its maximum. One could notice that these curves always have the maximum value one, with A fit to different values. The red curves represent the fitting result of the measurement.

The three states obtained from these fittings are shown on the Poincaré sphere in Figure 5.5 (d), as the points h with the state $|H_M\rangle$, d with the state $|D_M\rangle$ and l with the state $|L_M\rangle$. We have found that the states $|H_M\rangle$ and $|L_M\rangle$ have orthogonal directions on the Poincaré sphere, whereas $|D_M\rangle$ is off by around 14 °with respect to the states on the orthogonal direction with $|H_M\rangle$ and $|L_M\rangle$ caused by misalignment introduced in the previous subsection.

Three sets of required rotation angles of the HWP and the QWP are then calculated using equation 2.35, to align the measurement bases to $|H\rangle$ and $|D\rangle$ and $|L\rangle$ in the QD reference frame. After aligning the detection bases to these three states, We perform another correlation measurement. The three states are roughly aligned to the QD eigenbasis $|H\rangle$ and superposition bases $|D\rangle$ and $|L\rangle$, however with small angular deviation within 10°on each basis. The fidelity calculated from the above result is around 90%. Although being well-above the classical limit, the entanglement fidelity still has a non-negligible drop.

To further improve the alignment, we took this alignment result as another set of S'_M, and the input polarisation states as S'_R. They combine with the previous S_M and S_R to form the matrices containing six polarisation states. This further improves the alignment precision and thus, a high entanglement fidelity is achievable as is introduced in Chapter 7. However, each one alignment

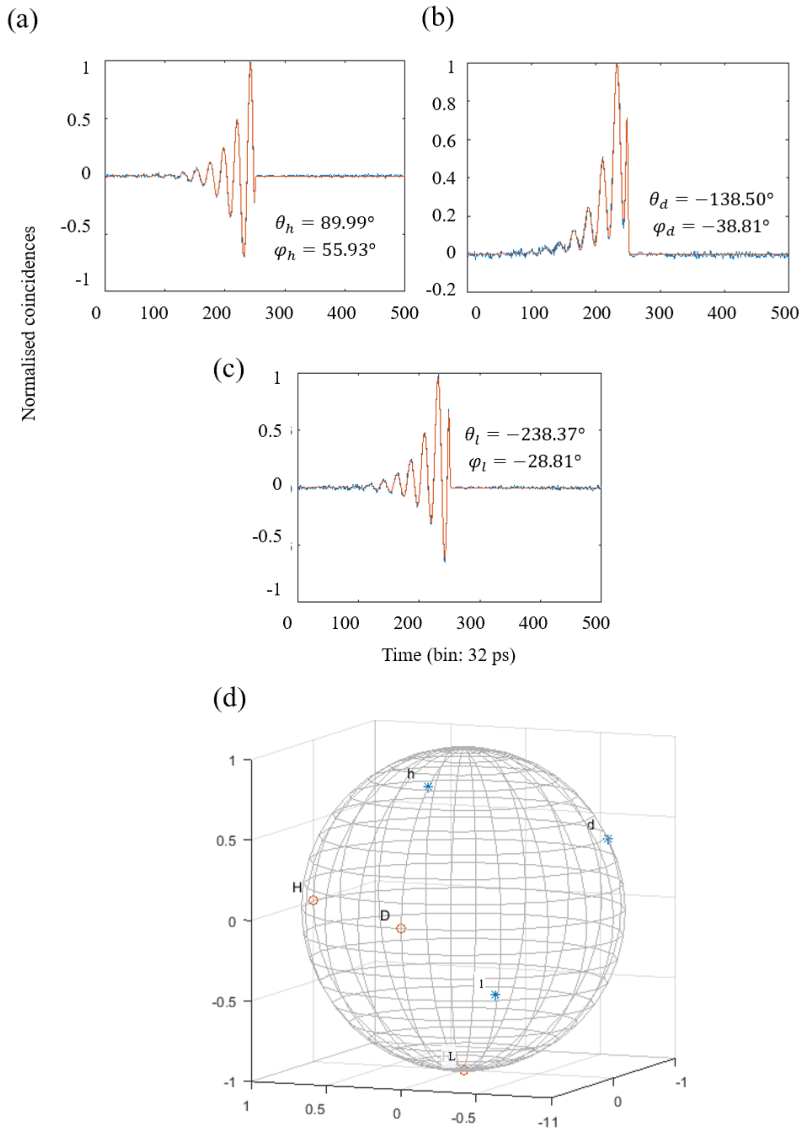

Fig. 5.5 Correlation measurement result with fitting curve for bases alignment. (a), (b) and (c) show the correlation measurement result in blue lines when the bases are aligned to $|H_R\rangle$, $|D_R\rangle$ and $|L_R\rangle$. The red curves are the fitted result that simultaneously emitting the value of θ and ϕ shown in the legends. Their position has been plotted on the Poincaré sphere shown in (d) as the points h, d and l. Simultaneously the reference states $|H_R\rangle$, $|D_R\rangle$ and $|L_R\rangle$ are shown in parallel as the points H, D and L.

processes generally takes hours of operation and measurement time, especially when the photons are sent over a long optical fibre. Luckily, the alignment has only to be done once given the short fibre between the QD and the filtering module remains typically stable.

Chapter 6

Multiplexing with Classical Communication

6.1 Classical channel for entanglement measurement

In the previous chapters, we have introduced core systems for performing the network integration of QDs, including the device and the optical collection module, the correlation measurement setup, the alignment module and the polarisation stabilisation system. These systems will be installed at two different locations where the photons are to be distributed, as is shown in Figure 6.1. The successful remote operation would require classical control signals established between the two locations for information sharing.

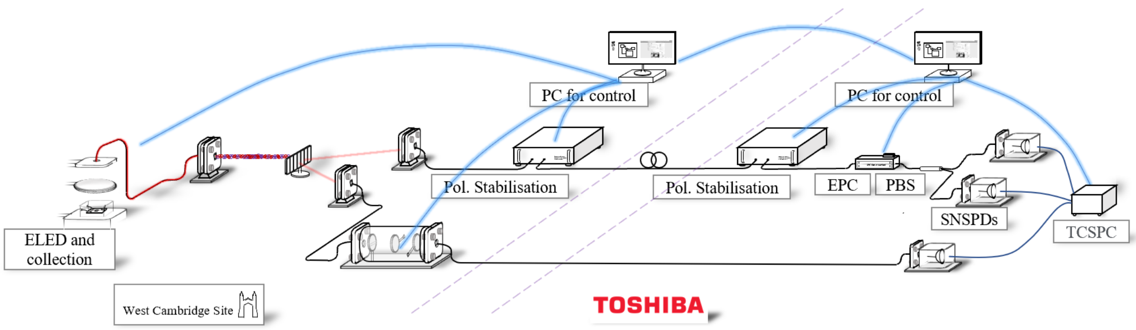

Fig. 6.1 Deployment of entangled photon pairs and flow of system control signal. In this scenario, the QD is deployed at Alice, and the entanglement is distributed between Alice and Bob. As a quantum node operator, Alice needs to control various critical equipment and components including the cryostat, QD current and voltage controllers, EPCs and polarisation stabilisation systems. Blue curves indicate its control signal flow in this case. For components located at Alice's end, it is easily managed. However, access to components at Bob's end would require classical communication between the two locations in addition to the quantum channel.

However, it means that for each link in a quantum network, there must be either at least two optical fibres connecting Alice and Bob, one dedicated for classical communication and the other one for qubit transmission [37, 36, 121], or a multi-core fibre [122–125]. It would require additional fibre installation or replacement, increasing the overall cost for constructing a quantum network.

One elegant way to address this issue is to multiplex the quantum and classical signal over the same optical fibre using coarse wavelength division multiplexing with quantum light at 1310 nm and classical traffic at 1550 nm. Previous field trials have illustrated the feasibility of multiplexing QKD qubits based on attenuated laser pulses with classical data traffic over installed network links [126–128]. In this work, we are adopting this approach for demonstrating for the first time the co-existence of entangled qubits from a sub-Poissonian photon source and classical data traffic over a real-world network.

6.2 Raman scattering and multiplexing scheme

In the multiplexing mentioned above performed on QKD systems, two schemes are considered in this work. In [126, 127, 129–131] the quantum signals are at the telecom O-band and classical signals are at the C-band, and in [132, 133] the scheme of locating both quantum and classical signal at the C-band is analysed. The performance of such multiplexing is influenced mainly by two factors: optical transmission loss and Raman scattering.

Figure 6.2 illustrates the optical loss depending on the wavelength of the light. We notice that the telecom C-band has relatively low loss (around 0.2 dB/km) compared to the telecom O-band (around 0.35 dB/km). Unlike classical signals where the optical transmission loss could be compensated by increasing the launch power, the single-photon emission rate of a QD device cannot be easily increased. Thus, the advantage of locating the quantum channel at the C-band is a higher photon rate at the receiving end.

Raman scattering or the Raman effect [134] is the inelastic scattering of photons by matter, meaning that there is an exchange of momentum. It is introduced by the interaction of photons with the phonons. An effect of it is that a portion of the input light will be scattered to other wavelengths. Raman scattering is normal in signal transmission over the optical fibre, and its effect increases with the fibre length. Thus, for urban-scale transmission over tens of kilometres, it could generate significant influence on signals at other wavelengths. Stokes scattering and anti-stokes scattering are used to describe photons scattered to lower energy (frequency) and higher energy (frequency). Figure 6.3 illustrates the physical of the Stokes and anti-stokes scattering. The intensity ratio between the two scatterings $I_{stokes}/I_{anti-stokes}$ is temperature-dependent and follow a Boltzman distribution, represented by the following equation:

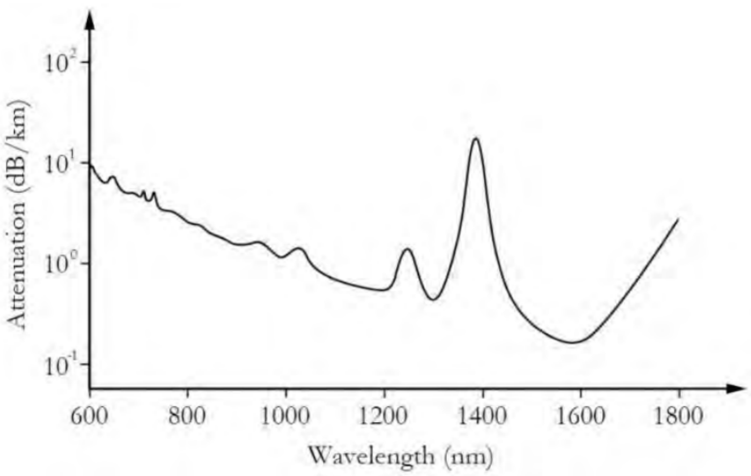

Fig. 6.2 Optical attenuation changed with wavelength [135]. Two transmission windows, the so-called telecom O-band and C-band, centred at 1310 nm and 1550 nm both have low loss compared with the surrounding environment. Therefore they are chosen as telecommunication windows for optical fibre communication.

$$\frac{I_{stokes}}{I_{anti-stokes}} = \frac{(\nu_0 - \nu_m)^4}{(\nu_0 + \nu_m)^4} e^{\frac{hc\nu_m}{K_B T}} \tag{6.1}$$

in which, ν_0 and ν_m are the frequency of the input and the scattered light, K_B is the Boltzman constant and T is the temperature. One could notice that stokes scattering becomes weaker as the transition energy (ν_m) increases. Thus, the advantage of locating the quantum channel at O-band is its reduced influence of Raman scattering from classical light at the C-band, compared with both quantum and classical channels being located the same band.

Thus, there is a performance trade-off in the allocation of wavelength windows of classical and quantum channels. Usually, the quantum channel at the telecom O-band is preferred for transmission at a relatively short distance (< 20 km). The difference of optical loss is not high at this distance for the quantum channel, and the background noise introduced by a scattered photon from the classical channel could be effectively reduced. For longer distance, one normally puts the quantum signal at C-band increase the signal-to-background ratio.

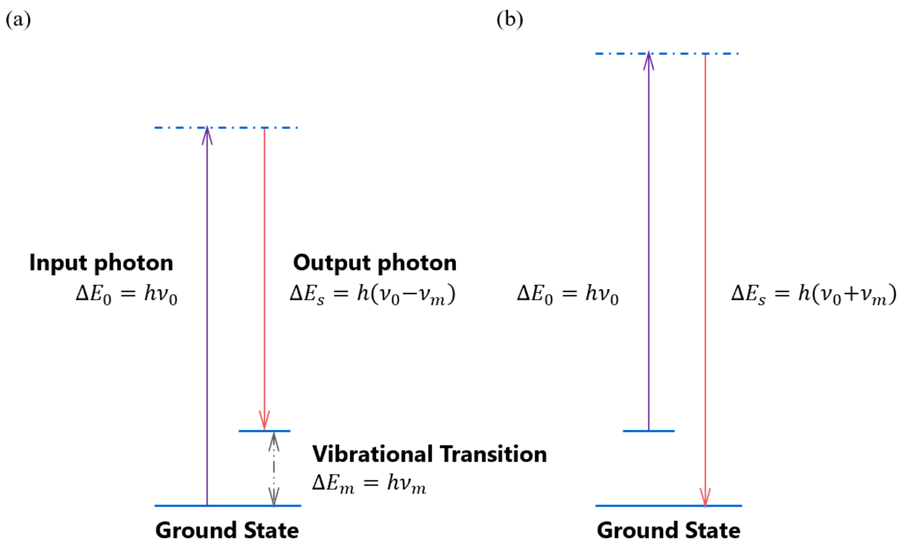

Fig. 6.3 Illustration of Raman scattering by virtual energy states. (a) Stokes scattering and (b) Anti-stokes scattering involves a photon excited to a virtual state (dashed line) and decay to a different energy level. The actual energy transition is caused by the photon energy exchange with phonons.

6.3 Multiplexing system design

6.3.1 Classical communication using transceivers and optical circulators

Standard 1 Gbit/s optical transceiver modules at the telecom C-band are installed to establish the classical communication links in this work. Figure 6.4 (a) shows a schematic for the communication system. The two transceiver modules are at different locations connected via an installed optical fibre, with two optical circulators installed at each end. The light generated from the transmitter port of both modules passes the circulators to the receiver port at the opposite module, enabling bi-directional communication. Each transceiver is connected to a computer (PC) via an Ethernet cable, establishing a local-area-network (LAN).

Figure 6.4 (b) lists a part of the specification sheet of the transceiver module. It is designed to a long-distance optical communication link, with maximally 120 km of fibre length. Thus, the small received power of around -32 dBm is supported. We here minimise the classical signal launch power to maintain a good single-photon purity. The installed fibre in this work has a length of around 15 km and attenuation of 8.5 dB at the telecom C-band, And we introduce an optical attenuator for an additional 20 dB attenuation at the transmitter port of the transceiver module (not shown in the figure). Hence, the launch power is reduced from 1 mW to 10 μW. This adds up to 28.5 dB in the overall transmission.

(a)

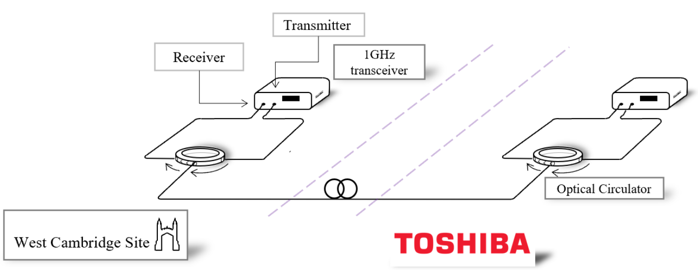

(b)

Form Factor	SFP	**Max Data Rate**	1000Mbps
Wavelength	1550nm	**Max Cable Distance**	120km
Connector	LC duplex	**Optical Components**	DFB 1550nm
Media	SMF	**DOM Support**	Yes
TX Power	0dBm	**Receiver Sensitivity**	< -32dBm
Commercial Temperature Range	0 to 70°C (32 to 158°F)	**Protocols**	SFF-8472 MSA Compliant, IEEE 802.3ah-2004

Fig. 6.4 (a) System schematic for using optical circulators and 1 Gbit/s transceivers to achieve bidirectional classical communication between two locations linked with only one SMF. (b) Specification of the 1 Gbit/s transceiver used in this work.

6.3.2 Wavelength-division multiplexing on quantum and classical channel

Wavelength division multiplexing has become a well-established technology in classical communication. It is employed in nearly every optical communication network. For separating the quantum channel from the classical light, we introduce WDMs, which are typically used for multiplexing of classical signals in urban optical communication. They could be classified into the coarse wavelength-division multiplexer (CWDM), which splits light with large energy gap, for example into telecom O- and C-band; and DWDM, which splits one band into several independent channels with small wavelength separation. In this work, we make use of available commercial CWDMs for multiplexing of quantum and classical channels at O- and C-band.

Figure 6.5 (a) illustrates a schematic of the communication system with CWDMs to multiplex the classical signal with the quantum channel. The common port of the CWDMs is connected to the installed fibre. The telecom O-band and C-band ports are connected to the modules for distribution of entangled qubits and classical communication.

However, multiplexing of quantum and classical signals is not as straightforward. The energy of a photon at the centre of the telecom O-band (1310 nm) is 1.52×10^{-19} Joules. For a single photon source that has a photon emission rate of $1 \times 10^6\, cps$, the received power is maximally 0.15 pW (-98 dBm). The classical communication, as is introduced in the previous subsection, has a launch power of from -20 dBm. Thus, common channel isolation in commercial CWDMs around 30 dB would result in the classical light leaking into the quantum channel with a power that is more than two orders of magnitude higher than the detected photons. The designed multiplexing system would therefore need to minimise the background introduced by the classical light to a level that has a much smaller power than single photons.

(a)

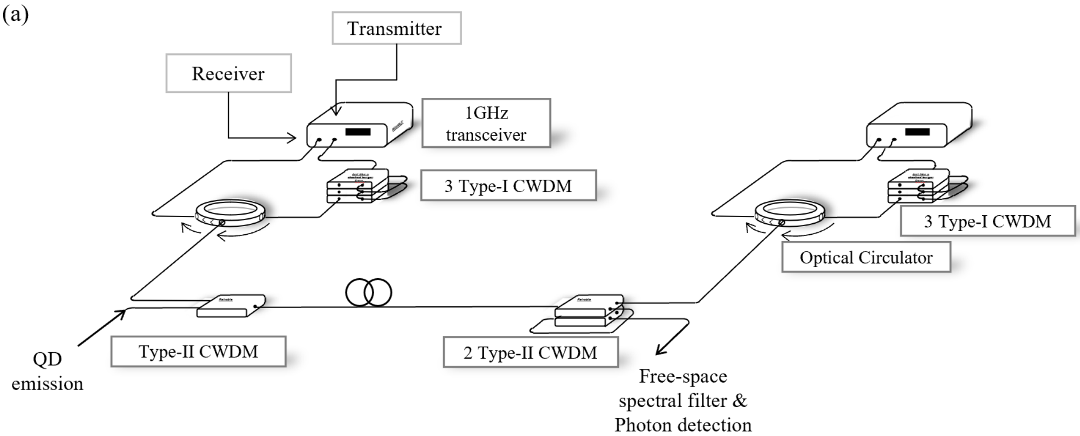

(b)

Type-I CWDM

Parameters	Unit	Performance
1310-1550 Isolation	dB	47
1550-1310 Isolation	dB	55
Insertion loss	dB	0.3dB (measured)

Type-II CWDM

Parameters	Unit	Performance
1310-1550 Isolation	dB	>17
1550-1310 Isolation	dB	>17
Insertion loss	dB	0.1dB (measured)

Fig. 6.5 (a) Design for effective multiplexing of classical communication module with the quantum channel over a single SMF. We are introducing two types of CWDMs. Type-I CWDM has a high extinction ratio and insertion loss, which is used mainly for filtering. Type-II CWDM has low insertion loss and thus used as a multiplexer. (b) Specification of the two types of CWDMs used in this work.

For subtraction of the background in the quantum channel from the classical communication light, we need to consider three factors. The first factor is the generated classical light at the telecom O-band from the transceiver. In the commercial transceiver module, it is common to see some background generated at the band out of the transmitter wavelength range.

Suppression of the O-band classical light is realised by introducing a cascade of CWDMs at the transceiver. Figure 6.5 (b) shows the specification of CWDMs of type-I and type-II. The type-I CWDM has a high noise suppression ratio on output ports, but with a high measured insertion loss. Therefore, it is ideal for filtering the unwanted classical light at telecom O-band. As is shown in Figure 6.5 (a), three type-I CWDMs are connected to the transmitter port of the transceiver module directly. For each of the CWDM, the C-band output port is connected, and the O-band output port is terminated. This is to reduce the classical light generated at the telecom O-band getting injected into the installed fibre. During the experiment, we have discovered that one single type-II CWDM does not support enough background suppression. A cascade consisting of three CWDMs are therefore connected.

The second factor is the channel cross-talk. The type-II CWDMs are used here for multiplexing and demultiplexing the classical and quantum light. Given that the received power at telecom C-band is -28.5 dBm, leakage from the classical light with one CWDM is still significantly higher than the power of photons. Similar to filtering the light at the classical transmitter, two type-II CWDMs are installed in the quantum channel after the CWDM for multiplexing, to suppress the classical light at the telecom C-band in the quantum channel. We, however, have noticed that the background from such a scheme is still higher than the quantum signal, potentially due to the high bandwidth of the CWDM. In this filtering scheme, the SNSPDs detects the signal across the entire telecom O-band. Therefore, a free-space spectral filter is installed just before the SNSPD to suppress the remaining background at the telecom O-band further.

The third factor is the Raman scattering. As is introduced above, a small portion of the classical light at the telecom C-band will be scattered to shorter or longer wavelengths, resulting in additional background generated at the SNSPDs. Thanks to relatively weak anti-stokes scattering, the generated background is much lower than when the quantum and classical signal are located at the telecom C- and O-band. With the additional free-space spectral filter, the background from Raman scattering could be limited.

6.4 Performance analysis of the multiplexing system

Having a system with low optical loss is important for qubits transmission. For the quantum channel, 0.3 dB has been introduced by 3 CDWMs and 1.3 dB by the free-space spectral filter. The loss adds up to 1.6 dB. It results in a photon number loss of less than 35 %.

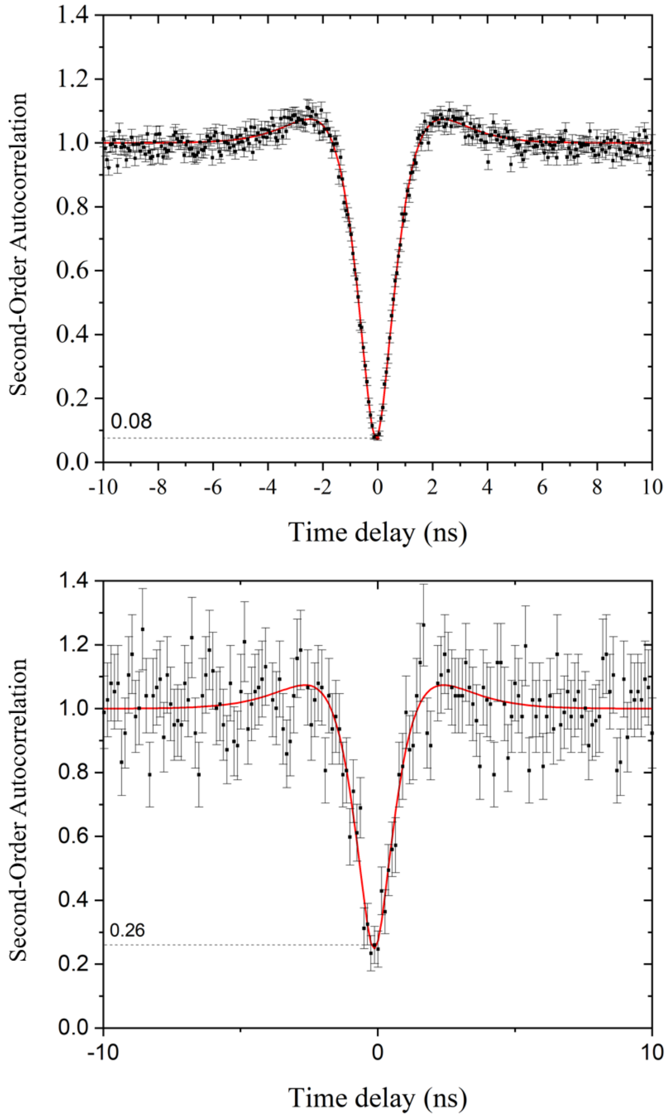

Fig. 6.6 Second-order autocorrelation measurement result for XX photons (a) in the laboratory and (b) after transmission over 15 km of installed fibre, multiplexed with classical data traffic. Data acquisition times were 5 min and 30 min, respectively. The red curves show a theoretical fitting function which is used to extract the displayed $g^{(2)}(0)$ values and corresponding background contribution. Displayed error bars are propagated from Poissonian counting statistics.

The most significant influence of the classical light on qubits is the additional background worsening the single-photon purity. A second-order correlation measurement on XX photons has been performed to see its effect. Here, we show a comparison of the $g^{(2)}$ result between when measured in the laboratory environment (Figure 6.6 (a)) and when measured after deployment with multiplexed classical traffic (Figure 6.6 (b)) with the fitting function equation 2.15. After transmission, the light is still strongly anti-bunched with a $g^{(2)}(0)$ value of 0.26 being significantly below the classical limit of 0.5.

The drop is analysed to be mainly caused by the reduced signal-to-background ratio. Revisiting equation 2.16, we extract a background to a single photon ratio of 15.4% from the measurement over the installed fibre. To notice, the photon rates on two SNSPDs are both under 20 kHz after sent over the installed fibre, compared with around 200 kHz measured in the lab. Therefore, it can be understood as the sum of the background from the source (4.2%) and an additional background (7.1%) due to a reduced signal caused by photon losses. The remaining contribution of 4.1% is most likely caused by stray light coupling into the photon collection at the remote location and small leakage from classical data traffic over the same fibre.

Chapter 7

Deployment

7.1 Detection system and polarisation analysing unit for deployment

Simple electrical operation and compatibility with wavelength division multiplexing standards have provided us with a great foundation for demonstrating the deployment and telecommunication network integration of the device. As already mentioned in previous chapters, we install the source at an office at CAM, whereas keeping the detection modules at CRL in the Science Park. There are two optical fibres of 15 km length each connecting CAM to CRL.

In realistic cases, quantum relays and repeaters in a quantum network naturally require measurement of qubits at the location where the information is supposed to be sent to. In this scenario, the generated entangled photon pair at a particular time would arrive at detectors with a time difference τ, which is not a constant due to the fibre length drift caused by changes in the environment such as temperature and stress. Therefore, synchronisation of XX and X photons is of great importance. People have introduced methods of synchronising the clocks for detection systems in QKD [136, 137] for deterministic qubits generation and detection.

In this work, we are making use of a four-channel SNSPDs in a closed-cycle cryostat with a Helium compressor. Given that the SNSPDs are at the same location, the synchronisation is enabled by connecting the detector output channel for X photons to the synchronisation channel of the TCSPC system, requiring no additional synchronisation link established.

The way to examine the performance of the deployed QD in this work is to check the entanglement fidelity of the emitted XX and X photon-pairs. The correlation measurement setup, as is introduced in Chapter 2, contains the SNSPDs connected with components for detection bases alignment including an EPC and a PBS, as is shown in Figure 7.1 (a). The same setup is connected to the XX photons emitted from the deployed QD in this work, as is shown in Figure 7.1 (b). Here, one of the optical fibre is used for transmitting the XX photons. On the other fibre link along which the X photons are transmitted, we place a polarisation analyser consisting of a HWP, a QWP and a LP. This analyser is installed in CAM, at the same location as the QD

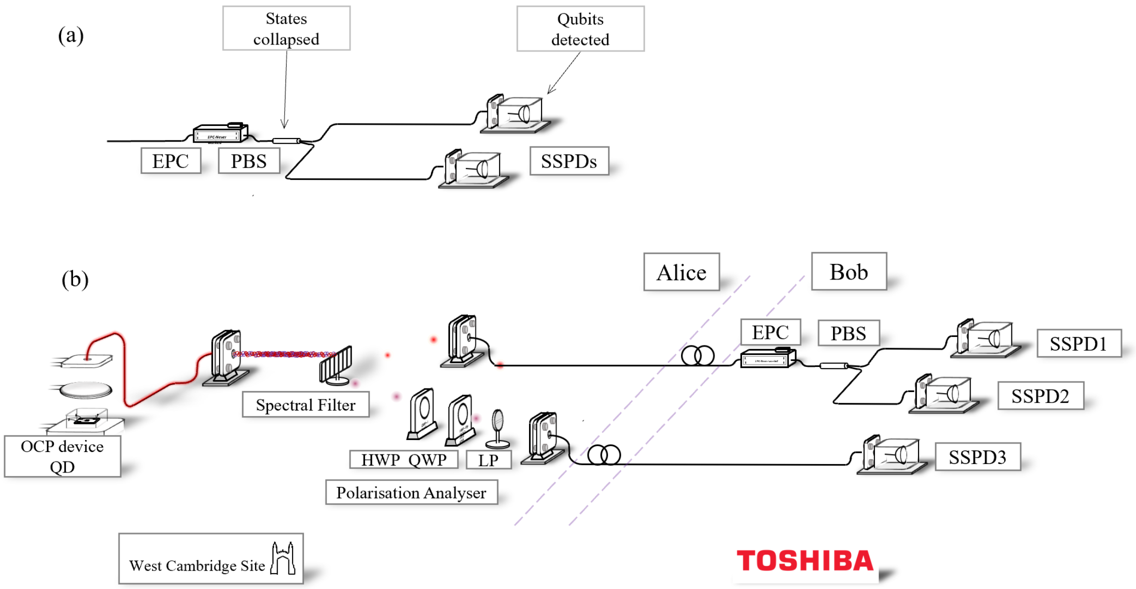

Fig. 7.1 A schematic of (a) a standard detection module for correlation measurement and (b) its implementation in this work. One could divide the detection module into two parts. The PBS is where the entangled state is collapsed after the EPC modulates the state. SNSPDs connected to the output ports of PBS record the count rate of photons. They are where the photon is detected. In this work, we keep such a photon detection module for XX at Bob. The module for X photons is separated with state collapsing components at Alice's and SNSPDs at Bob's location. We are using a polarisation analyser consisting of an HWP, a QWP and an LP to align the detection bases at Alice's location to arbitrary states.

emitter. It collapses polarisation-encoded entangled state at CAM, and send the X photons to the SNSPD at CRL. The X photons are used as a synchronisation signal to calculate the correlation coefficients.

The polarisation analysing module must enable photons to be collapsed to an arbitrary state. The analysis in 2.3.2 suggested that by changing θ_1 and θ_2, the combination of a HWP and a QWP, one could generate an arbitrary state on the Poincaré state. Before passing the linear polariser, similar to the bases alignment module consisting of an EPC and a PBS.

In practice, aligning this polarisation analysis unit to the desired states (referred to $|S\rangle$ here) is similar to the detection EPC alignment procedure introduced in Chapter 2. The generated references from the alignment setup in Chapter 5 passes such a polarisation analyser before sent over to the SNSPDs at CRL. Instead of operating four channels of EPC to minimise the signal, we alternate rotations between the HWP and QWP to minimise the count rate. The rotation angles for HWP and QWP at the minimum count rate is the corresponding operation for the state to be collapsed onto state $|S\rangle'$, which is orthogonal to $|S\rangle$ (with opposite directions on Poincaré sphere). For bringing the states to $|S\rangle$, we then rotates the HWP by 45°. However, it is not critical given that only co- or cross-polarisation matters for correlation measurement instead of actual states.

7.2 Network integration of the quantum dots

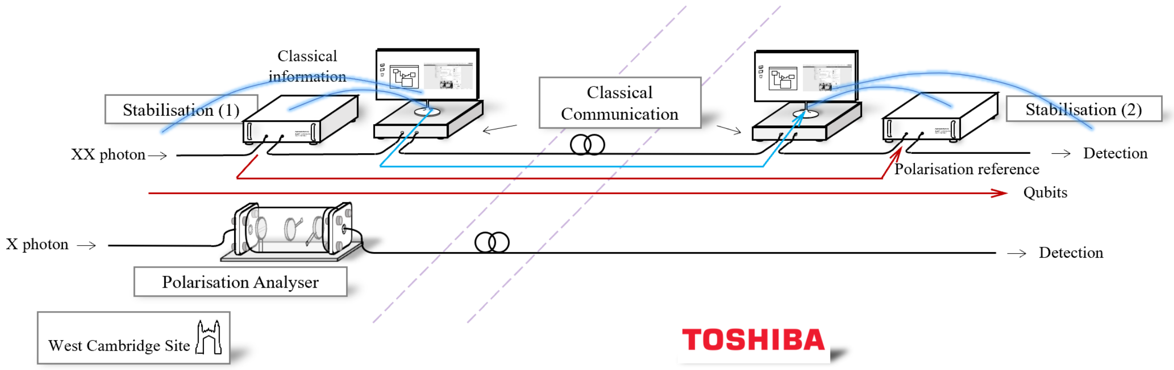

Fig. 7.2 Assembly order and classical information flow of the distribution system. XX photons are first time-division multiplexed with the polarisation references, and then wavelength-division multiplexed with the classical information. They are sent over one deployed fibre to CRL. X photons are collapsed at CAM, and are directly sent to CRL over the other deployed fibre.

The success of the network integration of the QD entangled photon-pair device is built upon various parts discussed in the previous chapters. We here summarised these parts into four systems: the ELED and correlation measurement system, polarisation stabilisation system, classical traffic multiplexing system and the polarisation analyser, following the assembly order shown in Figure 7.2. XX photons and polarisation references for the stabilisation system are time-division multiplexed, sharing the same wavelength. They are then wavelength-division multiplexed with the classical communication signal before being launched into the deployed fibre. The polarisation analyser is connected to X photons. As a result, these systems and modules are distributed in both locations. In CAM, we install the ELED, the polarisation references for correlation measurement bases alignment, the polarisation analyser for X photons, the detection part of the polarisation stabilisation system and one of the communication modules of the classical communication system. The remaining parts are located at CRL.

Following the above architecture, the final system is designed and its schematic is shown in Figure 7.3. We install a close-cycled cryostat by Montana Instruments Ltd. A microscope setup is installed above the cryostat to collect the emitted light from the QD. To enable the required stability for long-term transmission of entangled photons from the QD, we here introduce an additional mechanical stabilisation unit for the microscope setup, consisting of three Picomotor piezo linear actuators at x, y and z axis of the mechanical mount of the optical fibre coupler. These three actuators are driven by three voltage sources with feedback generated by the measured photon count rate. This stabilisation module is applied continuously to always maximise the recorded coincidences.

There are two optical fibres connecting CAM to CRL, for the transmission of XX and X photons respectively. For the installed fibre for transmission of XX photons, the polarisation stabilisation system and the classical multiplexing system are connected. As is mentioned in the

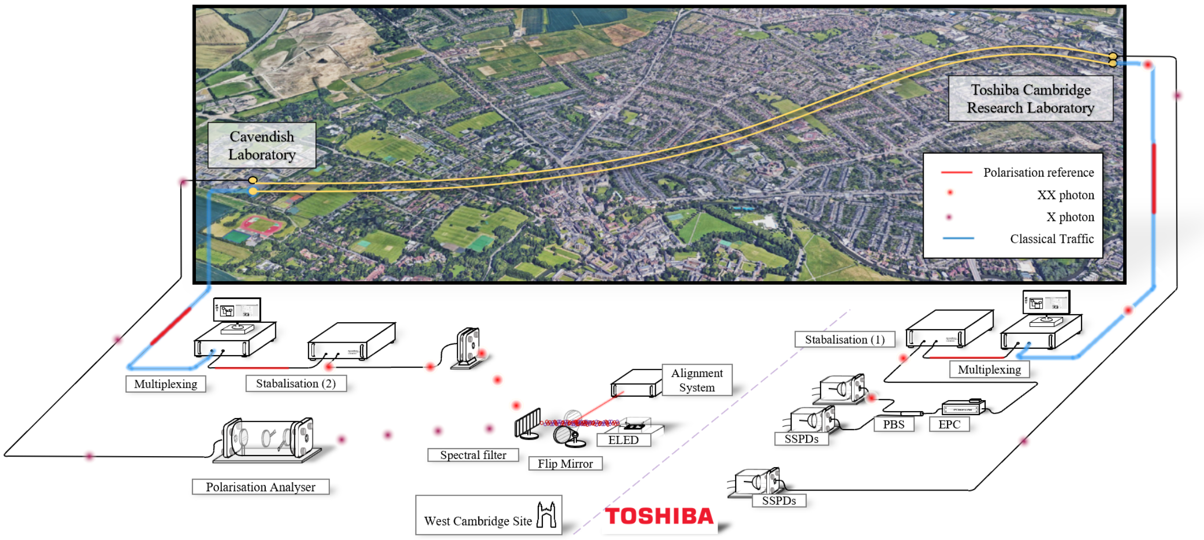

Fig. 7.3 Map: Imagery ©2019 Google, Getmapping plc, Infoterra Ltd & Bluesky, The GeoInformation Group, Maxar Technologies, Data SIO, NOAA, U.S. Navy, NGA, GEBCO, Maxar Technologies, Landsat / Copernicus, Map data ©2019.

A schematic of the overall experimental setup for entangled photon transmission from network-deployed ELED. Single photons are shown as ‘red’ (XX) and ‘violet’ (X) dots, laser pulses for polarisation stabilisation are shown as short ‘red’ lines and classical data traffic is shown as continuous ‘blue’ line. Entangled photon pairs are generated from the tuneable ELED device at West Cambridge (CAM). X and XX photons are spatially separated with a spectral filter module. X photons pass through a polarisation analyser consisting of a HWP, a QWP and a LP before being sent over one of the two installed fibres. Entangled XX photons are sent over the other field fibre which is stabilised for polarisation drifts using a polarisation stabilisation sub-system (Stabilisation 1 and 2). At CRL, their quantum state is measured using an EPC, a PBS and two SNSPDs. For remote control of the deployed source and system components, a classical data connection in the telecom C-band is established over the same fibre using a classical-quantum multiplexing system (labelled as Multiplexing). Arrival time of the X photons in the first fibre is measured with a third SNSPD at CRL. The alignment system is installed before the spectral filter, and a flip mirror is used to control whether the polarisation reference from the alignment system or the entangled photons are injected to the spectral filter.

previous section, X photons directly pass a polarisation analyser before being sent to CRL as a time reference. Therefore no polarisation stabilisation system is installed at the end of this fibre.

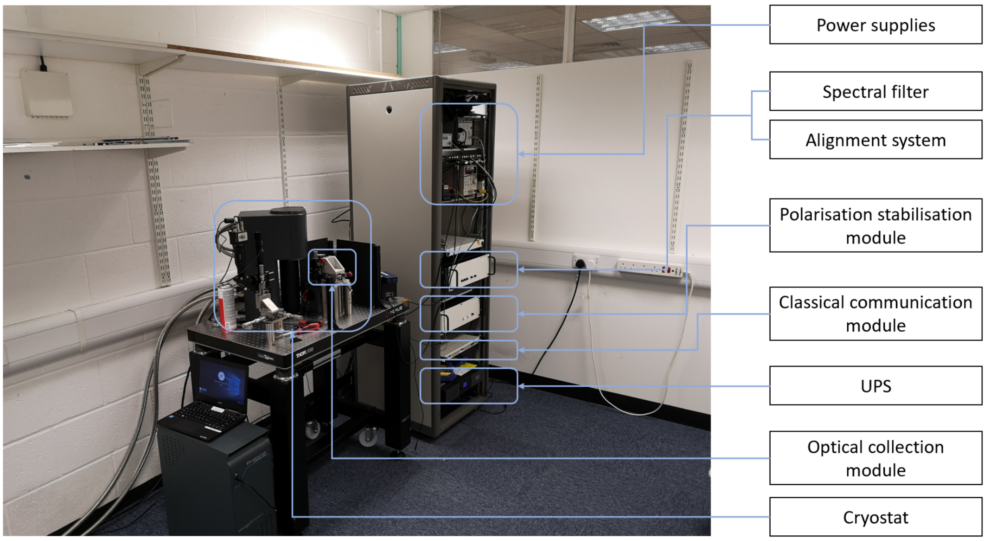

Fig. 7.4 The deployed systems for QD network integration at CAM. An optical bench and a standard optical rack are used for installing the systems, in a normal office of the Cavendish Laboratory. The cryostat is installed on a small optical bench with the collection module. All other system components are installed on the optical rack. An optical fibre is used to connect the source to the systems.

In addition to the modules mentioned above, power sources and controlling interface hardware needs to be deployed as well. All the modules and individual hardware pieces were carefully sealed and packed in cardboard boxes to prevent unwanted damage during the deployment. Figure 7.4 shows a photo of the deployed system at CAM. A rack is used for mounting deployed modules. From its bottom to top, there are respectively Uninterruptible Power Supply (UPS), the classical communication module, polarisation stabilisation module, spectral filter and alignment module, and power supplies The cryostat with optical collection module is placed to the left of it, which is connected to the spectral filter by an SMF.

Apart from the introduced systems and components, an additional fibre coupled tuneable filter has been installed at CRL before measuring X photons. It is to filter out additional noise at telecom O-band. During deployment and preparation, we found additional photon counts over the deployed fibre for X photon transmission. When measuring its end at CRL on the spectrometer, we observed sharp lines at around 1310 nm and 1313 nm respectively, as is shown in Figure 7.5 (a). It is, unfortunately, not possible to get access to every single node on this fibre in the CFN for testing the connection and finding the cause of it. However, it is very likely that the additional noise is introduced by a leak from a nearby standard optical fibre in the same optical cable. Figure 7.5 (b) shows a fibre-loss measurement result on the second fibre, from which we see a sharp increase at 11 km. It is potentially due to a sharp bend of SMF or loose connection that would both introduce unwanted leakage of signal in the fibre. The introduced

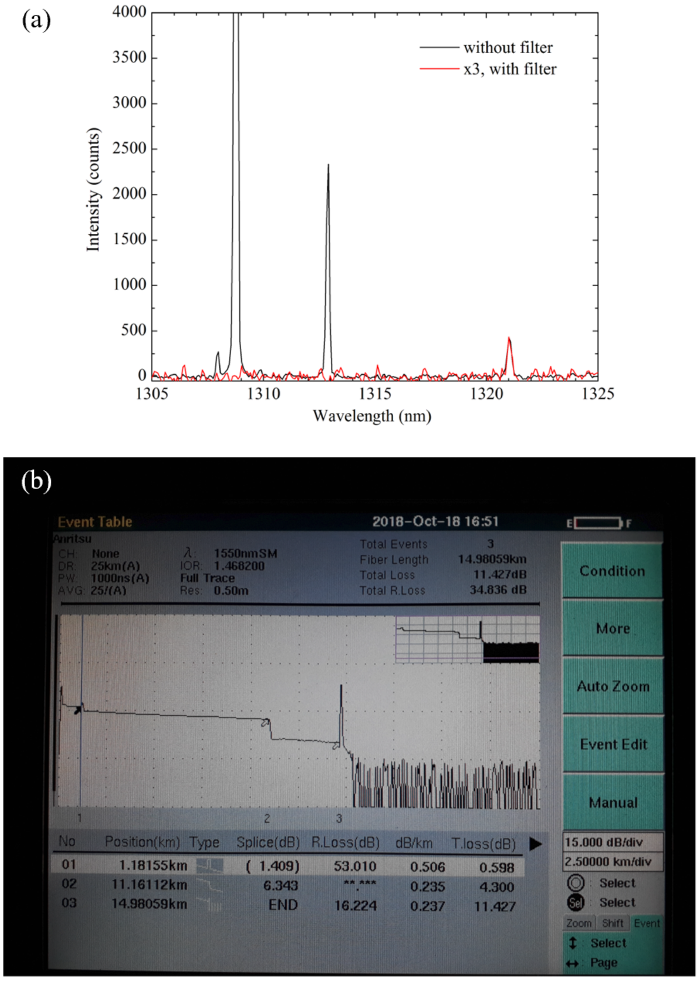

Fig. 7.5 Introduced noise at the telecom O-band and the optical loss for the deployed fibre for X photons. (a) We have observed noise on the deployed fibre used for X photon transmission at telecom O-band during the measurement with higher intensity than X photons, as is shown by the black curve. Such noise could be eliminated by applying a fibre tuneable filter before detection. The red curve indicates its spectrum after the filter. (b) Measured optical transmission attenuation corresponding to the transmission distance. We could observe a clear drop at 11 km from CRL.

filter is effective in noise reduction. The measured spectrum after the filter is shown in the red line in Figure (a), from which we noticed the elimination of noise on the output and only the quantum signal at 1321 nm is observed.

7.3 Overall system performance and remote entanglement measurement

For network integration of the QD device with time-multiplexed polarisation stabilisation system and wavelength-multiplexed classical communication system, it is important to achieve high single photon purity and entanglement fidelity for the entangled photon pairs, and high duty cycle and low loss for the system. In Chapter 6, we have performed the second-order correlation measurement confirming the high single-photon purity. Therefore in this section, we will evaluate the system from the other aspects.

7.3.1 System loss and duty cycle

Additional filters have been introduced to the system for minimising the background generated by the classical communication module, therefore, it is important to keep the optical loss from the fibre connection and system components at a minimum. Therefore, we have re-selected the EPC and the FWP used in the polarisation stabilisation system to ones with lowest optical loss among all available components, being respectively 0.68 dB and 0.98 dB. In addition, we have spliced most of the connections within the propagation of XX photons. The overall loss introduced by the multiplexing module and polarisation stabilisation system to XX photons are measured as 3.3 dB. The connection for transmitting entangled XX photons and establishing classical communication has a total loss of 8.5 dB at 1310 nm and the fibre used for sending the projected X photons has a loss of 12.5 dB.

While the previous entanglement measurement with the polarisation stabilisation system has already achieved a high duty-cycle of 98%, we have improved the algorithm for polarisation stabilisation to enable faster compensation operation and more frequency polarisation checks, reducing the operational time for polarisation recovery by 2 seconds. In this experiment, two polarisation references that are aligned along orthogonal axes on the Poincaré sphere are injected for 100 ms and measured over the field fibre every 15 s. Feedback to a polarisation controller is then applied to compensate for detected polarisation rotations. In addition, the stabilisation is forced every 225 s and typically takes around 3 s to reach maximum alignment. More frequent polarisation checks (with intervals being 10 s) are enabled, enabling the capability of detecting the polarisation change in a smaller time scale. The resulting overall duty-cycle for transmission of quantum bits is around 98%.

7.3.2 Remote entanglement measurement

Following Chapter 5, we have calibrated the polarisation bases using the M "uller matrix transformation method. And a final entanglement measurement result is shown in Figure 7.6 [138]. In this figure, (a)-(c) shows the results for co- and cross-polarised coincidences in the

$|HV\rangle$, $|DA\rangle$ and $|RL\rangle$ basis when projecting the quantum states of X photons at CAM and XX photons at CRL with a measurement time of 40 minutes on each basis. The detection basis was changed every ten minutes. In the HV basis, we observe a strong correlation of photon polarisations with a maximum contrast of 96.8%. The fidelity to the maximally entangled Bell ϕ^+ state peaks at 95.19 ± 0.5 % (see Figure 7.6(c)) for a post-selection window size of 32 ps. Compared with the entanglement measurement in Chapter 3, higher fidelity is obtained thanks to the accurate alignment supported by the method developed in Chapter 5. The zero-delay value is extracted using the same method as is introduced in Chapter 3.

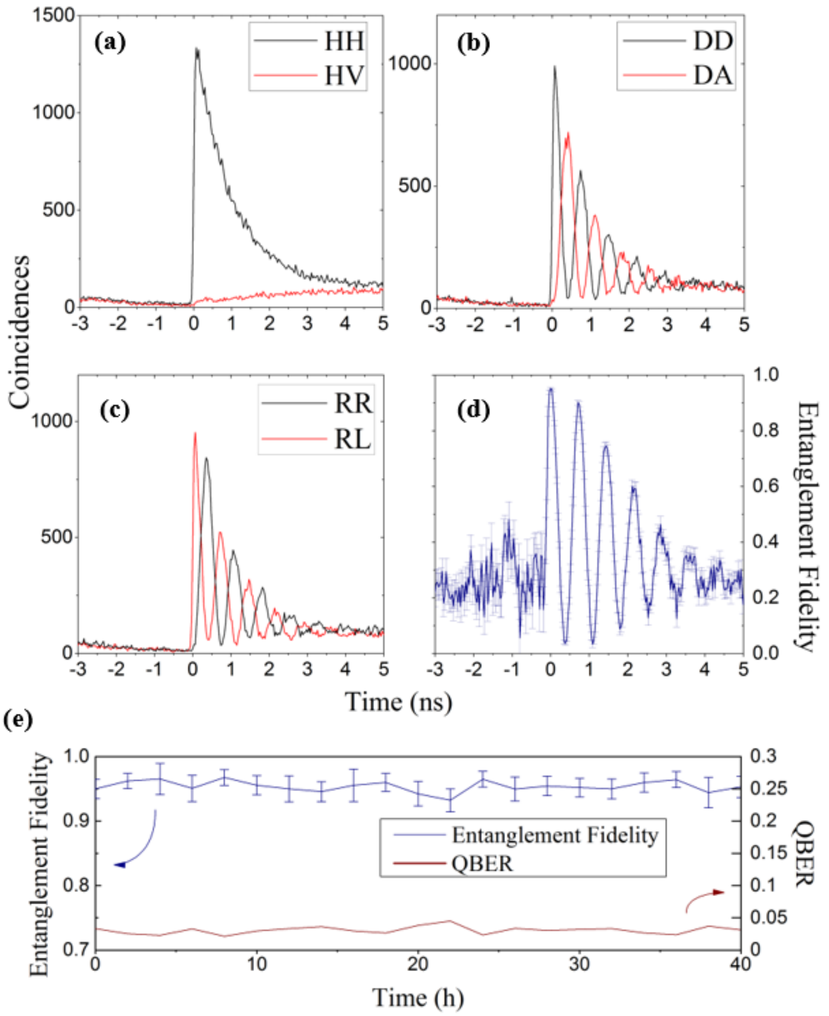

Fig. 7.6 3 Correlation measurements of entangled photons across installed network link. (a) HV basis; (b) DA basis; (c) RL basis. (d) Fidelity to Bell ϕ^+ state. Data is displayed on 32 ps resolution timing grid. (e) Evolution of maximum fidelity and corresponding quantum bit error rate (QBER) over 40 h of continuous operation. Each data point corresponds to 2h of data.

The experiment was continuously running over 40 hours to demonstrate the good stability of the deployed ELED device. Figure 7.6 (e) shows the evolution of the entanglement fidelity based on 2 hours of data per displayed point. The bottom of the graph shows the corresponding quantum-bit error rate, which is stable at around 3.4%. Compared with the measured maximum fidelity of 97.32% in a laboratory environment, a small drop is observed, which is mainly due to the reduced signal-to-background ratio. These results are directly obtained from raw data, and no background subtraction of any kind has been done during processing. The classical communication link was running at all times.

Chapter 8

Conclusion and Future work

8.1 Conclusion

In this work, we have successfully achieved the network integration of a QD device at a remote location outside of the laboratory. Entangled qubits with high fidelity were successfully acquired from the deployed device when operated remotely.

To achieve the network integrability of the entangled single-photon emitter, in Chapter 4 we have introduced an OCP QD device and verified its capability of generating high-fidelity entangled photon-pairs with network integration requirements such as full electrical operation. The device is operated under the driving current of 1.6mA. One can achieve a wavelength tuning range of 30nm by changing the tuning voltage from -0.5 V to -3.5 V while keeping the FSS below $10\mu eV$. Either when considering the tuning range of wavelength only or when considering the tuning range with respect to the maximally applied electric field, the QD device in this work has achieved larger tuneability compared with most other existing works. It also has a good single-photon purity for XX and X photons (both $g^{(2)}(0)$ being 0.08). We have obtained a laboratory-based entanglement fidelity from this device of $97.3 \pm 0.2\%$.

To help maintain the qubits entanglement during long-distance and long-term transmission, we have designed a polarisation stabilisation system to compensate for the variation of fibre birefringence as is introduced in Chapter 3. Different schemes for multiplexing polarisation references to the qubits have been studied and time-division multiplexing scheme has been chosen. The compensation on polarisation states variation is based on feedback from two polarisation references that have perpendicular directions on the Poincaré sphere. We have achieved full polarisation stabilisation capability with a duty cycle of 98% and a low loss of 2dB. This enables for the first time a stable transmission of entangled qubits with entanglement fidelity over 90% over an 18 km optical for one week.

We have further developed a new method for aligning the correlation measurement bases in Chapter 5, given that the standard spectral method turned out to be not working over long installed fibre. We here extract the unitary-transformed QD eigenbasis from the measured correlation coefficients, and calculate the Mueller matrix to represent the required unitary transformation of the optical fibre from the cryostat to a required location. This removes the requirement of a spectrometer to be installed with the QD at the same location. It will in the future support any on-chip or fibre-pigtailed devices.

In order to establish a classical communication channel among locations during the network integration without drastically increasing the cost of infrastructure, we have designed a classical-quantum multiplexing scheme as is introduced in Chapter 6. The signal from a C-band 1 Gbit telecommunication transceiver module is wavelength-multiplexed with the entangled photon-pairs at the O-band. A second-order correlation measurement of the XX photons over a 15 km deployed fibre with the multiplexed classical traffic has been carried out, illustrating a good single-photon purity maintained in this scheme.

And finally, the network integration of the developed OCP QD device has been achieved with all of the systems and modules described above. The device, the optical collection module, the polarisation detection module of the stabilisation system, the correlation bases alignment module, one classical communication module are deployed to an office location in the Cavendish. We have achieved an entanglement measurement with the deployed QD emitter with the fidelity of 95.3%, and for the first time with classical traffic multiplexed with the entangled photons over the same fibre. The measurement has further been carried out for over 40 hours to verify its operation stability and robustness. This work has, for the first time, demonstrated a true network integration of a telecom QD device in a deployed fibre network in an urban environment. The fully electrically operated and tuned OCP QD device and the system designed for multiplexing with classical traffic has made it possible for qubits to be generated transmitted in a pre-deployed optical fibre network.

8.2 Future work

8.2.1 Device improvement

This work has proven the capability of OCP devices generating high-fidelity entangled photon-pairs. Potential improvement could be made to enhance network integrability.

A discovered issue of the OCP devices is that a change on the voltage (or current) applied to either the pumping or the tuning diode would simultaneously change the n-type potential of the other diode. This happens even though the Ohmic contact deposited on the n-type layer is grounded. A potential reason is that the pumping and tuning diode share the same n-type layer. And the Ohmic contact (grounded) for n-type layer is more than 200 μm apart from the device. Given that the conductivity of GaAs/AlGaAs is lower than a conductor, the current flows over the n-type layer would cause a potential difference that makes the n-type voltage of both diodes different from the ground.

Even though such a feature does not drastically influence the operation of the OCP devices, it does provide a coupling of pumping and tuning parameters that influences the QD characterisation. Separating the n-type layer of the pumping diode from that of the tuning diode could be a potential solution for this issue. That would require an additional etching to be performed, generating gaps between two diodes where all the doped layers are removed, as is shown in Figure 8.1. In such a design, a two-level etching needs to be performed with enough depth for reaching the n-type layer and undoped layer beneath.

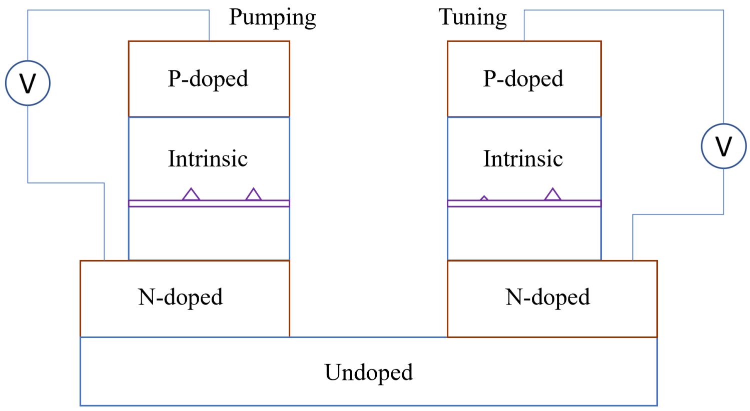

Fig. 8.1 OCP device with separated n-type contact for pumping and tuning diodes. In this design, part of the region that separates the pumping and tuning diode needs to be deeply etched such that the n-type material is completely removed.

Furthermore, the ultimate network integration of a quantum emitter requires the deterministic source of coherent single photons to enable quantum information processing with other devices and applications in the network. However, it still remains a challenge to implement deterministic resonant optical excitation of the quantum dot that is required for generating single coherent photon. In one of the relevant publication of this work [61], we have realised 1 GHz pulsed operation of an electrically excited QD device and successfully distributed the generated entangled qubits across the Cambridge Fibre Network with the entanglement fidelity of 79%. While being purely electrically operated that is favoured by a practical network environment, this device does not support the wavelength and FSS tuneability, which could become a limiting factor for the network application.

The developed OCP devices in this work could become a suitable design for a deterministic QD entangled photon-pair source. However, the device developed in this work has a large p-type area that results in a large device capacitance and therefore, a small resonant frequency. The QD device in [61] has an oval shape with the length of the long axis less than 100 μm. Its area is much smaller compared with the pumping diode of the OCP device in this work.

The minimal device size based on the current design is limited by the size of the bonding pad. During fabrication, gold wires are used for connecting the device bonding pad to the packaging, which is melted at the moment when it is attached to the pad. This generates a small metal ball with a width of around tens of micrometres, as is shown in Figure 3.3 (a). To prevent the metal ball from spreading to the p-type region for QD measurements or n-type region, we design the pad to have a minimum diameter of around 80 μm currently.

We here propose a new design that allows the bonding pad to be separated from the device itself, by depositing an insulation layer Si_3N_4 before the metal contact, as is shown in Figure 8.2. The deposited metal contact could span across the p- or n-type layer and the insulation layer, making a bigger bonding pad possible on a small device. Therefore, the area of the pumping and tuning diodes could be reduced to a size where GHz operation could be achieved. Calibration will be necessary for getting the optimal area since smaller pumping diode also leads to less excitation light reaching the QDs. During the processing of these devices, evaporator with rotation axis might be needed due to the requirement of vertically deposited metal connections.

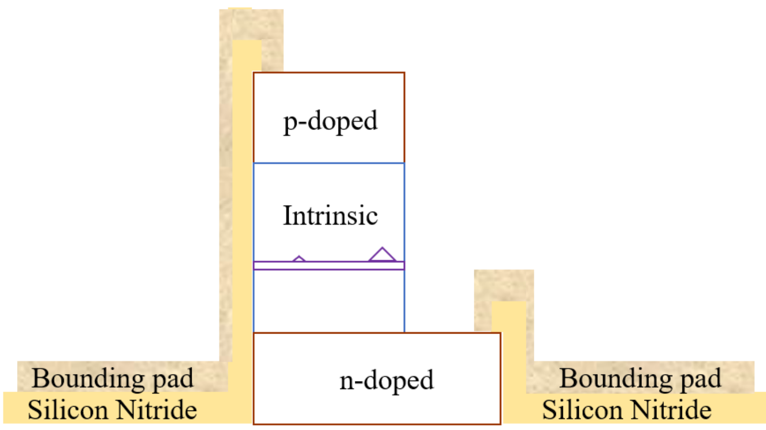

Fig. 8.2 An improved device fabrication method. A layer of Si_3N_4 is deposited before the metal contact. It leaves a window where the emitted photons from the QD are collected. Metal contact is then deposited covering certain areas on both of the Si_3N_4 and the p- or n-type layer. Since Si_3N_4 is an insulator, the current or voltage will only be applied to the connected mesas. Hence, the QD devices could be small while the large bonding pad is sitting on the insulation layer.

Although we have discussed the impact of the InGaAs strain-relaxation layer on the on-chip pumping efficiency in Chapter 4 by making a comparison of an OCP device made on wafer W1310 with a similar device made on wafer W950, a detailed and quantitative study on the influence of the wafer structure to the on-chip pumping efficiency would further support a comprehensive understanding of the on-chip pumping technique. Furthermore, characteristics of the pumping light could be studied by measurement of photon reflectance.

One important result to investigate from this work is that described in subsection 4.2.2, where we have witnessed an efficiency difference on devices made from the central region of W1310 with the devices made from the edge of W1310. The emission spectra in Figure 3.5 (b) and (c) show different profiles of light emitted from the InGaAs layer collected from the pumping diode compared with that collected from the tuning diode. It could be potentially due to the higher QD density, which requires more excitation power.

Long-distance quantum communication requires the photon rate to be significantly increased to overcome high optical loss. Given that photons are collected in the vertical direction, device design with micropillar, CBG and solid immersion lens [139, 140] technology could effectively enhance the photon emission toward the collecting optical fibre. Such designs could be further improved by the fibre pig-tailing technique [141]. With the improved photon rate, quantum teleportation and entanglement swapping could be made possible.

8.2.2 Precise polarisation references for the alignment system

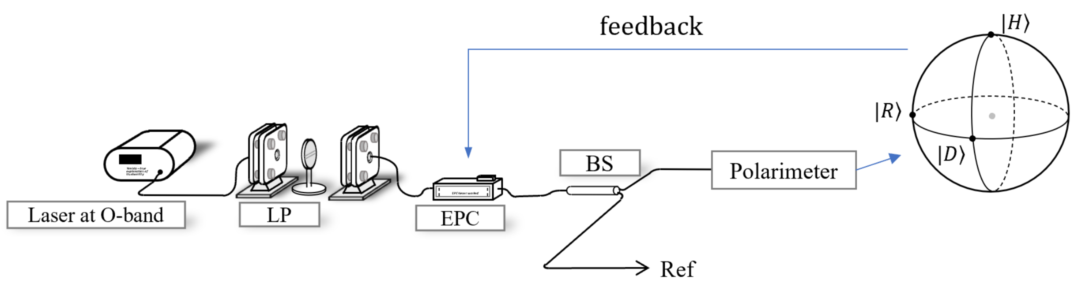

Fig. 8.3 A setup for generating polarisation references for the alignment system. The reference is generated from a laser and passes a LP. It is then connected to an EPC for states modulation. For monitoring purposes, a BS is connected, which splits the light into two paths. A polarimeter is connected to one of the output ports of the BS to generate the feedback. The other output would be connected to the main optical path as the polarisation references.

In Chapter 5, we discussed the limited precision of free-space waveplates for generating required polarisation states. To solve this problem, we have proposed a solution that is shown in Figure 8.3.

In this setup, the states are aligned by operating the EPC based on feedback generated from the polarimeter, which is connected to one of the output ports of the BS. And the light at another output ports of the BS would be used as the polarisation reference to the main system. Given that one can obtain highly accurate states by the polarimeter, the alignment could then be realised with much higher accuracy in this scheme.

8.2.3 Multiplexing with classical traffic and device network operation capability

In Chapter 6, we introduced the system for multiplexing the emitted photons from the QD with classical traffic. With various CWDMs and the free-space filter, the background at telecom O-band becomes negligible at the end of the detector, making the high-fidelity entanglement measurement possible over the deployed fibre. However, it is necessary to do further characterisation on components of the multiplexing systems for a deeper understanding of signal filtering and background suppression.

Two types of CWDM introduced for filtering the background generated from the standard classical module into the quantum channel have been introduced in Figure 6.5. In this work, we have only measured the insertion loss of these CWDMs without characterising the actual isolation. It is, however, important to measure the optical power emitted from the module and the CWDM isolation to quantify its influence on the quantum channel. Such an aspect is critical for design improvement to support its integration with a larger-scale communication network.

An important aspect of network integration is to reduce the system dependency on free-space optics. The current multiplexing design involves a free-space spectral filter that suppresses the background from the classical communication module. A potential improvement for the system would be to look at whether the free-space filter could be replaced by fibre-based spectral filters such as the tuneable bandpass fibre optical filter or the fibre Bragg-grating.

We would then need to consider cases where the realistic optical fibre network environment is applied. In this work, the 1 Gbit/s communication module is applied, which in practice could be suitable for a single point-to-point communication link. However, in a metropolitan area network (MAN) or a larger wide area network (WAN), the potential existence of various communication link multiplexed using the DWDMs on a single fibre results in a much higher classical power. The evaluation will need to be carried out, preparing for the device integration in such a network. Therefore, it is critical to measure the change of QBER with respect to the classical power given the current isolation. Such a measurement would make it possible to determine the required isolation given the optical power in the network when QBER is to be kept under a certain threshold.

References

[1] Charles H Bennett and Gilles Brassard. Quantum cryptography: Public key distribution and coin toss. In *Proceedings of the International Conference on Computers, Systems and Signal Processing*, 1984.

[2] Charles H Bennett, Gilles Brassard, and Artur K Ekert. Quantum cryptography. *Scientific American*, 267(4):50–57, 1992.

[3] Artur K Ekert. Quantum cryptography based on Bell's theorem. *Physical review letters*, 67(6):661, 1991.

[4] Charles H Bennett. Quantum cryptography using any two nonorthogonal states. *Physical review letters*, 68(21):3121, 1992.

[5] Hoi-Kwong Lo, Marcos Curty, and Bing Qi. Measurement-device-independent quantum key distribution. *Physical review letters*, 108(13):130503, 2012.

[6] Marco Lucamarini, Zhiliang L Yuan, James F Dynes, and Andrew J Shields. Overcoming the rate-distance limit of quantum key distribution without quantum repeaters. *Nature*, 557(7705):400–403, 2018.

[7] Hoi-Kwong Lo, Xiongfeng Ma, and Kai Chen. Decoy state quantum key distribution. *Physical review letters*, 94(23):230504, 2005.

[8] Valerio Scarani, Helle Bechmann-Pasquinucci, Nicolas J Cerf, Miloslav Dušek, Norbert Lütkenhaus, and Momtchil Peev. The security of practical quantum key distribution. *Reviews of modern physics*, 81(3):1301, 2009.

[9] Boris Korzh, Charles Ci Wen Lim, Raphael Houlmann, Nicolas Gisin, Ming Jun Li, Daniel Nolan, Bruno Sanguinetti, Rob Thew, and Hugo Zbinden. Provably secure and practical quantum key distribution over 307 km of optical fibre. *Nature Photonics*, 9(3):163, 2015.

[10] Toshiba QKD system. https://www.toshiba.eu/eu/Cambridge-Research-Laboratory/Quantum-Information/Quantum-Key-Distribution/Toshiba-QKD-system/.

[11] Zhiliang Yuan, Alan Plews, Ririka Takahashi, Kazuaki Doi, Winci Tam, Andrew Sharpe, Alexander Dixon, Evan Lavelle, James Dynes, Akira Murakami, et al. 10-Mb/s quantum key distribution. *Journal of Lightwave Technology*, 36(16):3427–3433, 2018.

[12] Juan Yin, Yuan Cao, Yu-Huai Li, Ji-Gang Ren, Sheng-Kai Liao, Liang Zhang, Wen-Qi Cai, Wei-Yue Liu, Bo Li, Hui Dai, et al. Satellite-to-ground entanglement-based quantum key distribution. *Physical review letters*, 119(20):200501, 2017.

[13] Shuang Wang, Wei Chen, Zhen-Qiang Yin, Hong-Wei Li, De-Yong He, Yu-Hu Li, Zheng Zhou, Xiao-Tian Song, Fang-Yi Li, Dong Wang, et al. Field and long-term demonstration of a wide area quantum key distribution network. *Optics express*, 22(18):21739–21756, 2014.

[14] Paul Benioff. The computer as a physical system: A microscopic quantum mechanical hamiltonian model of computers as represented by turing machines. *Journal of statistical physics*, 22(5):563–591, 1980.

[15] SJ Lomonaco. Shor's quantum factoring algorithm. In *Proceedings of Symposia in Applied Mathematics*, volume 58, pages 161–180, 2002.

[16] Jonathan A Jones, Michele Mosca, and Rasmus H Hansen. Implementation of a quantum search algorithm on a quantum computer. *Nature*, 393(6683):344–346, 1998.

[17] Frank Arute, Kunal Arya, Ryan Babbush, Dave Bacon, Joseph C Bardin, Rami Barends, Rupak Biswas, Sergio Boixo, Fernando GSL Brandao, David A Buell, et al. Quantum supremacy using a programmable superconducting processor. *Nature*, 574(7779):505–510, 2019.

[18] Vittorio Giovannetti, Seth Lloyd, and Lorenzo Maccone. Quantum metrology. *Physical review letters*, 96(1):010401, 2006.

[19] H Jeff Kimble. The quantum internet. *Nature*, 453(7198):1023–1030, 2008.

[20] Chip Elliott. Building the quantum network. *New Journal of Physics*, 4(1):46, 2002.

[21] Hoi-Kwong Lo and Hoi Fung Chau. Unconditional security of quantum key distribution over arbitrarily long distances. *science*, 283(5410):2050–2056, 1999.

[22] Xiongfeng Ma, Bing Qi, Yi Zhao, and Hoi-Kwong Lo. Practical decoy state for quantum key distribution. *Physical Review A*, 72(1):012326, 2005.

[23] Marcos Curty, Maciej Lewenstein, and Norbert Lütkenhaus. Entanglement as a precondition for secure quantum key distribution. *Physical review letters*, 92(21):217903, 2004.

[24] Stefano Pironio, Antonio Acin, Nicolas Brunner, Nicolas Gisin, Serge Massar, and Valerio Scarani. Device-independent quantum key distribution secure against collective attacks. *New Journal of Physics*, 11(4):045021, 2009.

[25] Nelson J Muga, Mário FS Ferreira, and Armando N Pinto. QBER estimation in QKD systems with polarization encoding. *Journal of Lightwave Technology*, 29(3):355–361, 2010.

[26] Stefano Pirandola. Capacities of repeater-assisted quantum communications. *arXiv preprint arXiv:1601.00966*, 2016.

[27] H-J Briegel, Wolfgang Dür, Juan I Cirac, and Peter Zoller. Quantum repeaters: the role of imperfect local operations in quantum communication. *Physical Review Letters*, 81(26):5932, 1998.

[28] Sreraman Muralidharan, Linshu Li, Jungsang Kim, Norbert Lütkenhaus, Mikhail D Lukin, and Liang Jiang. Optimal architectures for long distance quantum communication. *Scientific reports*, 6:20463, 2016.

[29] Marek Zukowski, Anton Zeilinger, Michael A Horne, and Aarthur K Ekert. "Event-ready-detectors" Bell experiment via entanglement swapping. *Physical Review Letters*, 71:4287–4290, 1993.

[30] Alexander I Lvovsky, Barry C Sanders, and Wolfgang Tittel. Optical quantum memory. *Nature photonics*, 3(12):706, 2009.

[31] Pierre Jobez, Nuala Timoney, Cyril Laplane, Jean Etesse, Alban Ferrier, Philippe Goldner, Nicolas Gisin, and Mikael Afzelius. Towards highly multimode optical quantum memory for quantum repeaters. *Physical Review A*, 93(3):032327, 2016.

[32] Hugues De Riedmatten, Ivan Marcikic, Wolfgang Tittel, Hugo Zbinden, Daniel Collins, and Nicolas Gisin. Long distance quantum teleportation in a quantum relay configuration. *Physical Review Letters*, 92(4):047904, 2004.

[33] Daniel Collins, Nicolas Gisin, and Hugues De Riedmatten. Quantum relays for long distance quantum cryptography. *Journal of Modern Optics*, 52(5):735–753, 2005.

[34] Christiana Varnava, R Mark Stevenson, Jonas Nilsson, Joanna Skiba-Szymanska, Branislav Dzurňák, Marco Lucamarini, Richard V Penty, Ian Farrer, David A Ritchie, and Andrew J Shields. An entangled-LED-driven quantum relay over 1 km. *Npj Quantum Information*, 2:16006, 2016.

[35] J Huwer, RM Stevenson, J Skiba-Szymanska, MB Ward, AJ Shields, M Felle, I Farrer, David Alastair Ritchie, and Richard Vincent Penty. Quantum-dot-based telecommunication-wavelength quantum relay. *Physical Review Applied*, 8(2):024007, 2017.

[36] Raju Valivarthi, Qiang Zhou, Gabriel H Aguilar, Varun B Verma, Francesco Marsili, Matthew D Shaw, Sae Woo Nam, Daniel Oblak, Wolfgang Tittel, et al. Quantum teleportation across a metropolitan fibre network. *Nature Photonics*, 10(10):676, 2016.

[37] Qi-Chao Sun, Ya-Li Mao, Si-Jing Chen, Wei Zhang, Yang-Fan Jiang, Yan-Bao Zhang, Wei-Jun Zhang, Shigehito Miki, Taro Yamashita, Hirotaka Terai, et al. Quantum teleportation with independent sources and prior entanglement distribution over a network. *Nature Photonics*, 10(10):671–675, 2016.

[38] Albert Einstein, Boris Podolsky, and Nathan Rosen. Can quantum-mechanical description of physical reality be considered complete? *Physical review*, 47(10):777, 1935.

[39] Reinhard F Werner. Quantum states with Einstein-Podolsky-Rosen correlations admitting a hidden-variable model. *Physical Review A*, 40(8):4277, 1989.

[40] John S Bell. On the einstein podolsky rosen paradox. *Physics Physique Fizika*, 1(3):195, 1964.

[41] Charles H Bennett, Gilles Brassard, Claude Crépeau, Richard Jozsa, Asher Peres, and William K Wootters. Teleporting an unknown quantum state via dual classical and einstein-podolsky-rosen channels. *Physical review letters*, 70(13):1895, 1993.

[42] Dik Bouwmeester, Jian-Wei Pan, Klaus Mattle, Manfred Eibl, Harald Weinfurter, and Anton Zeilinger. Experimental quantum teleportation. *Nature*, 390(6660):575–579, 1997.

[43] Jian-Wei Pan, Dik Bouwmeester, Harald Weinfurter, and Anton Zeilinger. Experimental entanglement swapping: entangling photons that never interacted. *Physical review letters*, 80(18):3891, 1998.

[44] Paul G Kwiat, Klaus Mattle, Harald Weinfurter, Anton Zeilinger, Alexander V Sergienko, and Yanhua Shih. New high-intensity source of polarization-entangled photon pairs. *Physical Review Letters*, 75(24):4337, 1995.

[45] John C Howell, Ryan S Bennink, Sean J Bentley, and Robert W Boyd. Realization of the einstein-podolsky-rosen paradox using momentum-and position-entangled photons from spontaneous parametric down conversion. *Physical Review Letters*, 92(21):210403, 2004.

[46] Haibo Wang, Tomoyuki Horikiri, and Takayoshi Kobayashi. Polarization-entangled mode-locked photons from cavity-enhanced spontaneous parametric down-conversion. *Physical Review A*, 70(4):043804, 2004.

[47] Ying Wu, Marvin G Payne, EW Hagley, and L Deng. Preparation of multiparty entangled states using pairwise perfectly efficient single-probe photon four-wave mixing. *Physical Review A*, 69(6):063803, 2004.

[48] Hiroki Takesue and Kyo Inoue. Generation of polarization-entangled photon pairs and violation of Bell's inequality using spontaneous four-wave mixing in a fiber loop. *Physical Review A*, 70(3):031802, 2004.

[49] Hiroki Takesue and Kyo Inoue. Generation of 1.5 μm band time-bin entanglement using spontaneous fiber four-wave mixing and planar light-wave circuit interferometers. *Physical Review A*, 72(4):041804, 2005.

[50] Oliver Benson, Charles Santori, Matthew Pelton, and Yoshihisa Yamamoto. Regulated and entangled photons from a single quantum dot. *Physical review letters*, 84(11):2513, 2000.

[51] N Akopian, NH Lindner, E Poem, Y Berlatzky, J Avron, D Gershoni, BD Gerardot, and PM Petroff. Entangled photon pairs from semiconductor quantum dots. *Physical review letters*, 96(13):130501, 2006.

[52] R Hafenbrak, SM Ulrich, P Michler, L Wang, A Rastelli, and OG Schmidt. Triggered polarization-entangled photon pairs from a single quantum dot up to 30 K. *New Journal of Physics*, 9(9):315, 2007.

[53] Arvind Baskaran and Peter Smereka. Mechanisms of Stranski-Krastanov growth. *Journal of Applied Physics*, 111(4):044321, 2012.

[54] MB Ward, MC Dean, RM Stevenson, AJ Bennett, DJP Ellis, K Cooper, I Farrer, CA Nicoll, DA Ritchie, and AJ Shields. Coherent dynamics of a telecom-wavelength entangled photon source. *Nature communications*, 5:3316, 2014.

[55] Quantum dots : a true "particle in a box" system. http://physicsopenlab.org/2015/11/20/quantum-dots-a-true-particle-in-a-box-system/.

[56] CL Salter, RM Stevenson, I Farrer, CA Nicoll, DA Ritchie, and AJ Shields. An entangled-light-emitting diode. *Nature*, 465(7298):594, 2010.

[57] M Scholz, S Büttner, O Benson, AI Toropov, AK Bakarov, AK Kalagin, A Lochmann, E Stock, O Schulz, F Hopfer, et al. Non-classical light emission from a single electrically driven quantum dot. *Optics express*, 15(15):9107–9112, 2007.

[58] Takashi Kuroda, Takaaki Mano, Neul Ha, Hideaki Nakajima, Hidekazu Kumano, Bernhard Urbaszek, Masafumi Jo, Marco Abbarchi, Yoshiki Sakuma, Kazuaki Sakoda, et al. Symmetric quantum dots as efficient sources of highly entangled photons: Violation of Bell's inequality without spectral and temporal filtering. *Physical Review B*, 88(4):041306, 2013.

[59] Gediminas Juska, Valeria Dimastrodonato, Lorenzo O Mereni, Agnieszka Gocalinska, and Emanuele Pelucchi. Towards quantum-dot arrays of entangled photon emitters. *Nature Photonics*, 7(7):527, 2013.

[60] Jiaxiang Zhang, Johannes S Wildmann, Fei Ding, Rinaldo Trotta, Yongheng Huo, Eugenio Zallo, Daniel Huber, Armando Rastelli, and Oliver G Schmidt. High yield and ultrafast sources of electrically triggered entangled-photon pairs based on strain-tuneable quantum dots. *Nature communications*, 6:10067, 2015.

[61] Ginny Shooter, Ziheng Xiang, Jonathan RA Müller, Joanna Skiba-Szymanska, Jan Huwer, Jonathan Griffiths, Thomas Mitchell, Matthew Anderson, Tina Müller, Andrey B Krysa, et al. 1GHz clocked distribution of electrically generated entangled photon pairs. *arXiv preprint arXiv:2004.14880*, 2020.

[62] M Anderson, T Müller, J Skiba-Szymanska, AB Krysa, J Huwer, RM Stevenson, J Heffernan, DA Ritchie, and AJ Shields. Gigahertz-clocked teleportation of time-bin qubits with a quantum dot in the telecommunication C band. *Physical Review Applied*, 13(5):054052, 2020.

[63] Jonathan RA Müller, R Mark Stevenson, Joanna Skiba-Szymanska, Ginny Shooter, Jan Huwer, Ian Farrer, David A Ritchie, and Andrew J Shields. Active reset of a radiative cascade for superequilibrium entangled photon generation. *arXiv preprint arXiv:2001.06251*, 2020.

[64] Adrien Dousse, Jan Suffczyński, Alexios Beveratos, Olivier Krebs, Aristide Lemaître, Isabelle Sagnes, Jacqueline Bloch, Paul Voisin, and Pascale Senellart. Ultrabright source of entangled photon pairs. *Nature*, 466(7303):217–220, 2010.

[65] Serkan Ates, Luca Sapienza, Marcelo Davanco, Antonio Badolato, and Kartik Srinivasan. Bright single-photon emission from a quantum dot in a circular bragg grating microcavity. *IEEE Journal of Selected Topics in Quantum Electronics*, 18(6):1711–1721, 2012.

[66] Hui Wang, Yu-Ming He, T-H Chung, Hai Hu, Ying Yu, Si Chen, Xing Ding, M-C Chen, Jian Qin, Xiaoxia Yang, et al. Towards optimal single-photon sources from polarized microcavities. *Nature Photonics*, 13(11):770–775, 2019.

[67] R Mark Stevenson, Robert J Young, Paola Atkinson, Ken Cooper, David A Ritchie, and Andrew J Shields. A semiconductor source of triggered entangled photon pairs. *Nature*, 439(7073):179, 2006.

[68] JM Taylor, CM Marcus, and MD Lukin. Long-lived memory for mesoscopic quantum bits. *Physical review letters*, 90(20):206803, 2003.

[69] Hui Wang, Yu He, Yu-Huai Li, Zu-En Su, Bo Li, He-Liang Huang, Xing Ding, Ming-Cheng Chen, Chang Liu, Jian Qin, et al. High-efficiency multiphoton boson sampling. *Nature Photonics*, 11(6):361, 2017.

[70] Yan Chen, Jiaxiang Zhang, Michael Zopf, Kyubong Jung, Yang Zhang, Robert Keil, Fei Ding, and Oliver G Schmidt. Wavelength-tunable entangled photons from silicon-integrated III–V quantum dots. *Nature communications*, 7(1):1–7, 2016.

[71] Bianca Höfer, Fabian Olbrich, Jan Kettler, Matthias Paul, Jonathan Höschele, Michael Jetter, Simone L Portalupi, Fei Ding, Peter Michler, and Oliver G Schmidt. Tuning emission energy and fine structure splitting in quantum dots emitting in the telecom O-band. *AIP Advances*, 9(8):085112, 2019.

[72] T Müller, J Skiba-Szymanska, AB Krysa, J Huwer, M Felle, M Anderson, RM Stevenson, J Heffernan, David Alastair Ritchie, and AJ Shields. A quantum light-emitting diode for the standard telecom window around 1,550 nm. *Nature communications*, 9(1):862, 2018.

[73] Fabian Olbrich, Jonatan Höschele, Markus Müller, Jan Kettler, Simone Luca Portalupi, Matthias Paul, Michael Jetter, and Peter Michler. Polarization-entangled photons from an InGaAs-based quantum dot emitting in the telecom C-band. *Applied Physics Letters*, 111(13):133106, 2017.

[74] Juan Yin, Yuan Cao, Yu-Huai Li, Sheng-Kai Liao, Liang Zhang, Ji-Gang Ren, Wen-Qi Cai, Wei-Yue Liu, Bo Li, Hui Dai, et al. Satellite-based entanglement distribution over 1200 kilometers. *Science*, 356(6343):1140–1144, 2017.

[75] Sheng-Kai Liao, Wen-Qi Cai, Wei-Yue Liu, Liang Zhang, Yang Li, Ji-Gang Ren, Juan Yin, Qi Shen, Yuan Cao, Zheng-Ping Li, et al. Satellite-to-ground quantum key distribution. *Nature*, 549(7670):43–47, 2017.

[76] A Tajima, T Kondoh, T Ochi, M Fujiwara, K Yoshino, H Iizuka, T Sakamoto, A Tomita, E Shimamura, S Asami, et al. Quantum key distribution network for multiple applications. *Quantum Science and Technology*, 2(3):034003, 2017.

[77] GL Roberts, M Lucamarini, ZL Yuan, JF Dynes, LC Comandar, AW Sharpe, AJ Shields, M Curty, IV Puthoor, and E Andersson. Experimental measurement-device-independent quantum digital signatures. *Nature communications*, 8(1):1–7, 2017.

[78] G Vilela De Faria, J Ferreira, GB Xavier, GP Temporão, and Jp Von Der Weid. Polarisation control schemes for fibre-optics quantum communications using polarisation encoding. *Electronics Letters*, 44(3):228–229, 2008.

[79] Alberto Boaron, Gianluca Boso, Davide Rusca, Cédric Vulliez, Claire Autebert, Misael Caloz, Matthieu Perrenoud, Gaëtan Gras, Félix Bussières, Ming-Jun Li, et al. Secure quantum key distribution over 421 km of optical fiber. *Physical review letters*, 121(19):190502, 2018.

[80] JF Dynes, Adrian Wonfor, WW-S Tam, AW Sharpe, R Takahashi, M Lucamarini, A Plews, ZL Yuan, AR Dixon, J Cho, et al. Cambridge quantum network. *npj Quantum Information*, 5(1):1–8, 2019.

[81] The tokyo QKD network. http://www.uqcc.org/QKDnetwork/.

[82] Adrian Wonfor, JF Dynes, R Kumar, H Qin, WWS Tam, A Plews, AW Sharpe, M Lucamarini, ZL Yuan, RV Penty, et al. High performance field trials of QKD over a metropolitan network. *Quantum Cryptography (Qcrypt)*, page Th467, 2017.

[83] Masahide Sasaki, M Fujiwara, H Ishizuka, W Klaus, K Wakui, M Takeoka, S Miki, T Yamashita, Z Wang, A Tanaka, et al. Field test of quantum key distribution in the Tokyo QKD network. *Optics express*, 19(11):10387–10409, 2011.

[84] Kaoru Shimizu, Toshimori Honjo, Mikio Fujiwara, Toshiyuki Ito, Kiyoshi Tamaki, Shigehito Miki, Taro Yamashita, Hirotaka Terai, Zhen Wang, and Masahide Sasaki. Performance of long-distance quantum key distribution over 90-km optical links installed in a field environment of tokyo metropolitan area. *Journal of Lightwave Technology*, 32(1):141–151, 2013.

[85] Yan Chen, Iman Esmaeil Zadeh, Klaus D Jöns, Andreas Fognini, Michael E Reimer, Jiaxiang Zhang, Dan Dalacu, Philip J Poole, Fei Ding, Val Zwiller, et al. Controlling the exciton energy of a nanowire quantum dot by strain fields. *Applied Physics Letters*, 108(18):182103, 2016.

[86] Jingzhong Yang, Michael Zopf, and Fei Ding. Strain tunable quantum dot based nonclassical photon sources. *Journal of Semiconductors*, 40:000000–000000, 2019.

[87] Jing Tang and Xiu-Lai Xu. Magneto optical properties of self-assembled InAs quantum dots for quantum information processing. *Chinese Physics B*, 27(2):027804, 2018.

[88] S Sanguinetti, M Gurioli, E Grilli, M Guzzi, and M Henini. Piezoelectric-induced quantum-confined stark effect in self-assembled InAs quantum dots grown on (N11) GaAs substrates. *Applied Physics Letters*, 77(13):1982–1984, 2000.

[89] AJ Bennett, MA Pooley, RM Stevenson, MB Ward, RB Patel, A Boyer de La Giroday, N Sköld, I Farrer, CA Nicoll, DA Ritchie, et al. Electric-field-induced coherent coupling of the exciton states in a single quantum dot. *Nature Physics*, 6(12):947, 2010.

[90] Pierce Munnelly, Tobias Heindel, Alexander Thoma, Martin Kamp, Sven H ofling, Christian Schneider, and Stephan Reitzenstein. Electrically tunable single-photon source triggered by a monolithically integrated quantum dot microlaser. *Acs Photonics*, 4(4):790–794, 2017.

[91] Jun-Wei Luo, Ranber Singh, Alex Zunger, and Gabriel Bester. Influence of the atomic-scale structure on the exciton fine-structure splitting in InGaAs and GaAs quantum dots in a vertical electric field. *Physical Review B*, 86(16):161302, 2012.

[92] Pierce Munnelly, Tobias Heindel, Matthias M Karow, Sven Höfling, Martin Kamp, Christian Schneider, and Stephan Reitzenstein. A pulsed nonclassical light source driven by an integrated electrically triggered quantum dot microlaser. *IEEE Journal of Selected Topics in Quantum Electronics*, 21(6):681–689, 2015.

[93] JP Lee, E Murray, AJ Bennett, DJP Ellis, C Dangel, Ian Farrer, P Spencer, David Alastair Ritchie, and AJ Shields. Electrically driven and electrically tunable quantum light sources. *Applied Physics Letters*, 110(7):071102, 2017.

[94] Markus Müller, Samir Bounouar, Klaus D Jöns, M Glässl, and P Michler. On-demand generation of indistinguishable polarization-entangled photon pairs. *Nature Photonics*, 8(3):224–228, 2014.

[95] Daniel Huber, Marcus Reindl, Yongheng Huo, Huiying Huang, Johannes S Wildmann, Oliver G Schmidt, Armando Rastelli, and Rinaldo Trotta. Highly indistinguishable and strongly entangled photons from symmetric GaAs quantum dots. *Nature communications*, 8(1):1–7, 2017.

[96] C Nawrath, F Olbrich, M Paul, SL Portalupi, M Jetter, and P Michler. Coherence and indistinguishability of highly pure single photons from non-resonantly and resonantly excited telecom C-band quantum dots. *Applied Physics Letters*, 115(2):023103, 2019.

[97] L Besombes, K Kheng, L Marsal, and H Mariette. Acoustic phonon broadening mechanism in single quantum dot emission. *Physical Review B*, 63(15):155307, 2001.

[98] R Seguin, A Schliwa, S Rodt, K Pötschke, UW Pohl, and D Bimberg. Size-dependent fine-structure splitting in self-organized InAs/GaAs quantum dots. *Physical review letters*, 95(25):257402, 2005.

[99] RM Stevenson, RM Thompson, AJ Shields, I Farrer, BE Kardynal, DA Ritchie, and M Pepper. Quantum dots as a photon source for passive quantum key encoding. *Physical Review B*, 66(8):081302, 2002.

[100] Martin Connor Patrick Felle. *Telecom Wavelength Quantum Devices*. PhD thesis, University of Cambridge, 2017.

[101] M Anderson, T Müller, J Huwer, J Skiba-Szymanska, AB Krysa, RM Stevenson, J Heffernan, DA Ritchie, and AJ Shields. Quantum teleportation using highly coherent emission from telecom C-band quantum dots. *npj Quantum Information*, 6(1):1–7, 2020.

[102] M Felle, J Huwer, RM Stevenson, J Skiba-Szymanska, MB Ward, Ian Farrer, RV Penty, DA Ritchie, and AJ Shields. Interference with a quantum dot single-photon source and a laser at telecom wavelength. *Applied Physics Letters*, 107(13):131106, 2015.

[103] Peter Grünwald. Effective second-order correlation function and single-photon detection. *New Journal of Physics*, 21(9):093003, 2019.

[104] Markus Aspelmeyer, Hannes R Böhm, Tsewang Gyatso, Thomas Jennewein, Rainer Kaltenbaek, Michael Lindenthal, Gabriel Molina-Terriza, Andreas Poppe, Kevin Resch, Michael Taraba, et al. Long-distance free-space distribution of quantum entanglement. *science*, 301(5633):621–623, 2003.

[105] Robert J Young, R Mark Stevenson, Paola Atkinson, Ken Cooper, David A Ritchie, and Andrew J Shields. Improved fidelity of triggered entangled photons from single quantum dots. *New Journal of Physics*, 8(2):29, 2006.

[106] Grant R Fowles. *Introduction to modern optics*. Courier Corporation, 1989.

[107] Nicolas Fressengeas. Polarization Optics. *Université Paul Verlaine Metz*, cel-00521501v3, 2010.

[108] AG Baca, F Ren, JC Zolper, RD Briggs, and SJ Pearton. A survey of ohmic contacts to III-V compound semiconductors. *Thin Solid Films*, 308:599–606, 1997.

[109] A Piotrowska, A Guivarc'h, and G Pelous. Ohmic contacts to III–V compound semiconductors: A review of fabrication techniques. *Solid-State Electronics*, 26(3):179–197, 1983.

[110] Jiaxiang Zhang, Eugenio Zallo, Bianca Höferr, Yan Chen, Robert Keil, Michael Zopf, Stefan Böttner, Fei Ding, and Oliver G Schmidt. Electric-field-induced energy tuning of on-demand entangled-photon emission from self-assembled quantum dots. *Nano letters*, 17(1):501–507, 2017.

[111] Shahriar Aghaeimeibodi, Chang-Min Lee, Mustafa Atabey Buyukkaya, Christopher JK Richardson, and Edo Waks. Large stark tuning of InAs/InP quantum dots. *Applied Physics Letters*, 114(7):071105, 2019.

[112] Yu-Bo Sheng and Lan Zhou. Deterministic polarization entanglement purification using time-bin entanglement. *Laser Physics Letters*, 11(8):085203, 2014.

[113] Harishankar Jayakumar, Ana Predojević, Thomas Kauten, Tobias Huber, Glenn S Solomon, and Gregor Weihs. Time-bin entangled photons from a quantum dot. *Nature communications*, 5(1):1–5, 2014.

[114] E Moreau, I Robert, JM Gérard, I Abram, L Manin, and V Thierry-Mieg. Single-mode solid-state single photon source based on isolated quantum dots in pillar microcavities. *Applied Physics Letters*, 79(18):2865–2867, 2001.

[115] Tatjana Wilk, Simon C Webster, Axel Kuhn, and Gerhard Rempe. Single-atom single-photon quantum interface. *Science*, 317(5837):488–490, 2007.

[116] Gordon W Day. Birefringence measurements in single mode optical fiber. In *Single Mode Optical Fibers*, volume 425, pages 72–81. International Society for Optics and Photonics, 1983.

[117] GB Xavier, G Vilela de Faria, GP Temporão, and JP Von der Weid. Full polarization control for fiber optical quantum communication systems using polarization encoding. *Optics express*, 16(3):1867–1873, 2008.

[118] Zi-Heng Xiang, Jan Huwer, R Mark Stevenson, Joanna Skiba-Szymanska, Martin B Ward, Ian Farrer, David A Ritchie, and Andrew J Shields. Long-term transmission of entangled photons from a single quantum dot over deployed fiber. *Scientific reports*, 9(1):1–6, 2019.

[119] JD Franson. Entanglement and decoherence in optical amplifiers. In *2017 IEEE Photonics Society Summer Topical Meeting Series (SUM)*, pages 93–94. IEEE, 2017.

[120] Misha Brodsky, Nicholas J Frigo, Misha Boroditsky, and Moshe Tur. Polarization mode dispersion of installed fibers. *Journal of Lightwave Technology*, 24(12):4584–4599, 2006.

[121] AR Dixon, JF Dynes, M Lucamarini, B Fröhlich, AW Sharpe, A Plews, S Tam, ZL Yuan, Y Tanizawa, H Sato, et al. High speed prototype quantum key distribution system and long term field trial. *Optics express*, 23(6):7583–7592, 2015.

[122] Liang Cui, Jie Su, Xiaoying Li, and ZY Ou. Distribution of entangled photon pairs over few-mode fibers. *Scientific reports*, 7(1):1–9, 2017.

[123] Emilio Hugues-Salas, Rui Wang, George T Kanellos, Reza Nejabati, and Dimitra Simeonidou. Co-existence of 9.6 Tb/s classical channels and a quantum key distribution (QKD) channel over a 7-core multicore optical fibre. In *2018 IEEE British and Irish Conference on Optics and Photonics (BICOP)*, pages 1–4. IEEE, 2018.

[124] Davide Bacco, Beatrice Da Lio, Daniele Cozzolino, Francesco Da Ros, Xueshi Guo, Yunhong Ding, Yusuke Sasaki, Kazuhiko Aikawa, Shigehito Miki, Hirotaka Terai, et al. Boosting the secret key rate in a shared quantum and classical fibre communication system. *Communications Physics*, 2(1):1–8, 2019.

[125] Chun Cai, Yongmei Sun, Yongrui Zhang, Peng Zhang, Jianing Niu, and Yuefeng Ji. Experimental wavelength-space division multiplexing of quantum key distribution with classical optical communication over multicore fiber. *arXiv preprint arXiv:1811.04198*, 2018.

[126] Paul D Townsend. Simultaneous quantum cryptographic key distribution and conventional data transmission over installed fibre using wavelength-division multiplexing. *Electronics Letters*, 33(3):188–190, 1997.

[127] Yingqiu Mao, Bi-Xiao Wang, Chunxu Zhao, Guangquan Wang, Ruichun Wang, Honghai Wang, Fei Zhou, Jimin Nie, Qing Chen, Yong Zhao, et al. Integrating quantum key distribution with classical communications in backbone fiber network. *Optics express*, 26(5):6010–6020, 2018.

[128] Iris Choi, Yu Rong Zhou, James F Dynes, Zhiliang Yuan, Andreas Klar, Andrew Sharpe, Alan Plews, Marco Lucamarini, Christian Radig, Jörg Neubert, et al. Field trial of a quantum secured 10 Gb/s DWDM transmission system over a single installed fiber. *Optics express*, 22(19):23121–23128, 2014.

[129] NI Nweke, P Toliver, RJ Runser, SR McNown, JB Khurgin, TE Chapuran, MS Goodman, RJ Hughes, CG Peterson, K McCabe, et al. Experimental characterization of the separation between wavelength-multiplexed quantum and classical communication channels. *Applied Physics Letters*, 87(17):174103, 2005.

[130] TE Chapuran, P Toliver, NA Peters, J Jackel, MS Goodman, RJ Runser, SR McNown, N Dallmann, RJ Hughes, KP McCabe, et al. Optical networking for quantum key distribution and quantum communications. *New Journal of Physics*, 11(10):105001, 2009.

[131] Iris Choi, Robert J Young, and Paul D Townsend. Quantum information to the home. *New Journal of Physics*, 13(6):063039, 2011.

[132] GB Xavier, G Vilela de Faria, GP Temporão, and JP Von Der Weid. Scattering effects on QKD employing simultaneous classical and quantum channels in telecom optical fibers in the C-band. In *AIP Conference Proceedings*, volume 1110, pages 327–330. American Institute of Physics, 2009.

[133] NA Peters, P Toliver, TE Chapuran, RJ Runser, SR McNown, CG Peterson, D Rosenberg, N Dallmann, RJ Hughes, KP McCabe, et al. Dense wavelength multiplexing of 1550 nm QKD with strong classical channels in reconfigurable networking environments. *New Journal of physics*, 11(4):045012, 2009.

[134] Herman A Szymanski. *Raman spectroscopy: theory and practice*. Springer Science & Business Media, 2012.

[135] Pedro Martín-Mateos. *New spectroscopic techniques and architectures for environmental and biomedical applications*. PhD thesis, 09 2015.

[136] C Gobby, ZL Yuan, and AJ Shields. Quantum key distribution over 122 km of standard telecom fiber. *Applied Physics Letters*, 84(19):3762–3764, 2004.

[137] Hiroki Takesue, Toshihiko Sasaki, Kiyoshi Tamaki, and Masato Koashi. Experimental quantum key distribution without monitoring signal disturbance. *Nature Photonics*, 9(12):827, 2015.

[138] Zi-Heng Xiang, Jan Huwer, Joanna Skiba-Szymanska, R Mark Stevenson, David JP Ellis, Ian Farrer, Martin B Ward, David A Ritchie, and Andrew J Shields. A tuneable telecom wavelength entangled light emitting diode deployed in an installed fibre network. *Communications Physics*, 3(1):1–8, 2020.

[139] Aleksander Bogucki, Łukasz Zinkiewicz, Magdalena Grzeszczyk, Wojciech Pacuski, Karol Nogajewski, Tomasz Kazimierczuk, Aleksander Rodek, Jan Suffczyński, Kenji Watanabe, Takashi Taniguchi, et al. Ultra-long-working-distance spectroscopy of single nanostructures with aspherical solid immersion microlenses. *Light: Science & Applications*, 9(1):1–11, 2020.

[140] Sarah Fischbach, Alexander Schlehahn, Alexander Thoma, Nicole Srocka, Timo Gissibl, Simon Ristok, Simon Thiele, Arsenty Kaganskiy, André Strittmatter, Tobias Heindel, et al. Single quantum dot with microlens and 3D-printed micro-objective as integrated bright single-photon source. *ACS photonics*, 4(6):1327–1332, 2017.

[141] Davide Cadeddu, Jean Teissier, Floris R Braakman, Niels Gregersen, Petr Stepanov, Jean-Michel Gérard, Julien Claudon, Richard J Warburton, Martino Poggio, and Mathieu Munsch. A fiber-coupled quantum-dot on a photonic tip. *Applied Physics Letters*, 108(1):011112, 2016.